Doctoral Dissertation

Academic Year 2025

Controlling Physical Properties of Artificial Spider Silk through Sequence-Property Relationships

Graduate School of Media and Governance

Keio University

Hiroyuki Nakamura

Doctoral Dissertation

Academic Year 2025

Controlling Physical Properties of Artificial Spider Silk through Sequence-Property Relationships

Abstract

Spiders utilize up to eight types of silk throughout their lifecycles, tailoring each physical properties of silks to specific functions. Among these, major ampullate silk (MA-silk) has attracted extensive research interest due to its extraordinary tensile strength and toughness, prompting continuous efforts to artificially reconstruct MA-silk. With the growing demand for environmentally sustainable alternatives to man made and natural fibers, recombinant based artificial spider silk has drawn considerable attention in the textile industry. To facilitate broader applications, controlling physical properties of the fiber is essential. This thesis aims to establish the design methodology by engineering protein sequences. A comparative analysis was conducted on the physical properties and protein composition of MA-silk and minor ampullate silk (MI-silk). The results indicate that differences in protein composition and sequences explain the distinct physical properties of these two silk types. To demonstrate the feasibility of manipulating these properties, fibers were produced and evaluated from recombinant mini-spidroins. MaSp1- and MiSp-based fibers exhibited higher tensile strength than those made from MaSp2, whereas MaSp2 fibers showed greater shrinkage in water (supercontraction) than both MaSp1 and MiSp. These findings suggest that the properties of artificial spider silk can be controlled through amino acid sequence designs reflective of those found in natural spidroins (Chapter 2). Building on these observations, motifs correlated with specific physical and structural properties were extracted from 1,000 spiders spidroins and applied to motif-based sequence modifications of artificial spider silk. Incorporating a positively correlated motif increased the tensile strength of the recombinant mini-spidroin fibers by 9.3%, while substituting a negatively correlated motif decreased it by 5.1% (Chapter 3). These outcomes demonstrate that motif-based sequence modifications can be employed to tailor the mechanical properties of artificial spider silk, thereby broadening its potential industrial applications.

Keywords: biomaterial, structural protein, protein design, artificial spider silk, mechanical property

論文題目

配列―物性相関を用いた人工クモ糸の物性制御

論文要旨

クモはその生態の中で最大 8 種類のクモ糸を使い分けており、各クモ糸は用途に合わせた物性を示す。中でも大瓶状腺糸（major ampullate silk: MA-silk）は、その高い強度とタフネスから盛んに研究され、人工的な再現が継続的に試みられてきた。近年、合成繊維や天然繊維による環境負荷が課題となる中で、人工クモ糸はこれらに代わる低環境負荷の繊維として注目を集めている。しかしながら、将来的により広範な分野への応用をめざすには、繊維の物性を制御することが必要不可欠である。本論文では、タンパク質のアミノ酸配列を設計することによって繊維の物性を制御する方法論を確立することを目的とし、まず MA-silk と小瓶状腺糸(minor ampullate silk: MI-silk）の物性およびタンパク質組成を比較分析した。その結果、両者のクモ糸タンパク質（spidroin）の組成が異なることが、物性の差異を説明する要因であることが示唆された。さらに、組換えタンパク質による人工クモ糸でこれを検証したところ、MaSp1 と MiSp を用いた繊維は MaSp2 を用いた繊維より高い強度を示す一方で、MaSp2 由来の繊維は、水に触れた際に MaSp1 や MiSp 由来の繊維より強く収縮を示す(超収縮現象)ことが確認された。これにより、タンパク質の配列設計によって人工クモ糸の物性を制御できる可能性が示された（第 2 章)。次に、1,000 種以上のクモ由来の spidroin 配列と物性の相関を解析し、物性と相関するモチーフを抽出して人工クモ糸に導入した。その結果、強度と正の相関をもつモチーフの導入により強度が 9.3% 向上し、負の相関をもつモチーフを導入により 5.1% 低下した(第 3 章)。これにより、物性と相関をもつモチーフを組み込んだタンパク質配列デザインが、人工クモ糸の物性制御を可能にし、より幅広い産業応用の可能性を切り開くことが示唆された。

キーワード：バイオマテリアル、構造タンパク質、タンパク質デザイン、クモ糸、人工クモ糸、力学物性

Table of Contents

List of Figures

List of Tables

Acknowledgements

First, I would like to express my sincere gratitude to my supervisor, Professor Kazuharu Arakawa, for giving me the opportunity to pursue a Ph.D. in his laboratory. Discussing various topics beyond research was one of my greatest pleasures during my doctoral studies. Without his constant guidance and outstanding mentorship, I could not have accomplished this work.

I would also like to thank my committee members, Professor Akio Kanai and Professor Yasuhiro Naito, for agreeing to serve as my assistant examiners. Their critical comments and suggestions during my thesis proposal were invaluable, and I sincerely hope this thesis reflects their insights.

I would like to thank all members of the Arakawa Lab for welcoming me and for providing generous support and feedback. Dr. Yasuha Watanabe, Dr. Sae Tanaka, and Dr. Saori M. Harada, and former member Dr. Nobuaki Kono offered insightful questions and suggestions that greatly helped my research. I am also grateful to Dr. Ana Lyons for encouraging me and for taking the time to review this thesis. Yuki Takai showed tremendous patience in helping accident-prone me. Lastly, I thank Naoko Ishii, Ayako Shirahata, and Makiko Anzai for their kindness and support.

I would like to thank Professor Keiji Numata for giving me the opportunity to work with him over 10 years. I am truly grateful that I could join the ImPACT Program PJ1-1 alongside both him and my supervisor. During the ImPACT Program (2014–2019) and afterward, I learned countless lessons from these two mentors. I would like to express my utmost respect and appreciation to them both.

I am grateful for the opportunity to collaborate with Dr. Ali Defrance Malay and Dr. Nur Alia Oktaviani. Their research on spider silk always inspires me, and I have learned a great deal from working with them. I also had the chance to work with Associate Professor Kenji Yazawa, Associate Professor Kosuke Tsuchiya, Dr. Hiroyasu Masunaga, Dr. Masaru Mori, Ayaka Tateishi, Nao Ifuku, and members of the RIKEN Biomacromolecules Research Team during the ImPACT Program. I sincerely appreciate their generous help throughout the project.

I would like to thank my arachnology mentor, Dr. Akio Tanikawa, for teaching me about spiders. Before I met him and conducted fieldwork together, I had virtually no knowledge of spider ecology or phylogeny. I greatly appreciate his guidance, comments, and discussions on all aspects of arachnology. I would also like to acknowledge members of the Arachnological Society of Japan for their valuable discussions in the arachnological research field and for supporting the Spider Silkome Project.

I would like to thank my manager at Spiber Inc., Chikako Sato, for giving me the opportunity to study and conduct basic research for many years. Her continuous support always encouraged and motivated me, and our discussions about research and industrial development were consistently

insightful. Her guidance also helped me balance research work and development tasks. I sincerely feel fortunate to have her as my boss.

I am grateful to have worked with Dr. Yusuke Ito, whose insights always gave me fresh perspectives. I would also like to thank my colleagues on the molecular design team—Hiroaki Sugawara, Toshiaki Osawa, Masahiro Murakami, and Yuka Kobayashi—for working closely with me and making me feel like a true team member. Our discussions in the headquarters laboratory remain some of my favorite memories.

I would additionally like to thank Dr. Daniel Pedrazzoli, Rintaro Ohtoshi, and Asaka Shinohara for their collaboration in the ImPACT PJ1-1 project. To the molecular properties evaluation team—Ryota Sato, Kaori Yaosaka, Yoshinori Ohta, Kazuko Wajima and HongFang Chi—thank you for your invaluable support; without it, I would have accomplished nothing. I am also deeply grateful to the founders, Kazuhide Sekiyama and Dr. Junichi Sugahara, as well as everyone at Spiber Inc., for working with me to develop the first artificial spider silk industry over these past 15 years. Nevertheless, I would like to note that Spiber Inc. had no role in the research design for studies conducted in this dissertation.

The studies presented in this thesis was generously supported by a grant from the MEXT Program: Data Creation and Utilization-Type Material Research and Development Project (grant number JPMXP1122714694), by research funds from the Yamagata Prefectural Government and Tsuruoka City, Japan, and by a grant from the ImPACT Program of the Council for Science, Technology and Innovation (Cabinet Office, Government of Japan).

Lastly, I would like to thank my family. I am deeply grateful to Tomonori Nakamura and Eiko Nakamura for their love and support throughout my life. As the years go by, I have come to appreciate their wisdom and patience more and more, and I am fortunate to have them as parents. I hope to pay it forward to my own children.

To Koki Nakamura and Taka Nakamura, your smiles and mere presence constantly motivate and encourage me. Finally, I would like to thank Mihoko Nakamura for her unfailing support and tremendous patience. Your understanding and forgiveness have helped me complete this thesis. In many aspects of my life, you have always reassured and encouraged me. Thank you for all your support.

Throughout my doctoral studies, I have been supported by many people. This thesis would not exist without their help, and I feel a responsibility to repay their kindness by using the expertise I have gained during my doctoral research.

Chapter 1
Introduction

1.1 Silk

"Silk" refers to fibrous protein-based materials secreted by specialized organs in certain animals. These materials are stored as a liquid solution and then solidify for use in the extracellular environment (Craig 1997; Herold and Scheibel 2017; Holland *et al.* 2019). Many arthropod species are known to produce silk (Figure 1-1) (Craig 1997; Sutherland *et al.* 2010; McKim and Turner 2024), and they use silk for constructing shelters, foraging, providing structural support for reproduction (e.g., egg sacs), and dispersing juveniles. Because the purposes for which silk is used vary widely, the form and physical properties of different silks also differ significantly (Craig 1997; Sutherland *et al.* 2010). The secondary structures of silk proteins are diverse and include alpha-helices (Hepburn, Chandler and Davidoff 1979; Yoshioka *et al.* 2017), parallel and cross β-sheets (Warwicker 1954, 1960; Rudall and Kenchington 1971), 3_1-helices (Polyglycine-II helices) (Perea *et al.* 2013; Riekel, Burghammer and Rosenthal 2020),and 3_2-helices (Collagen triple-helices) (Sutherland *et al.* 2010). Furthermore, silk proteins display additional diversity at the primary sequence level. This sequence variation, together with the structural and physicochemical properties of silk, drives divergence in physical characteristics. Spider mites (Tetranychidae) produce silk for building nests, creating draglines, and foraging (Kovoor 1987). Notably, spider mite silk has an extremely high Young's modulus (approximately 20–25 GPa), as measured by atomic force microscopy (Hudson *et al.* 2013; Lozano-Pérez *et al.* 2020). Proteomic evidence indicates that its primary amino acid sequence closely resembles that of aciniform and cylindrical spidroins—both associated with a high Young's modulus—suggesting a link between sequence similarity and the mechanical performance of spider mite silk (Arakawa *et al.* 2021). In addition, small benthic crustaceans called tanaids (Tanaidacea) use silk to form tube-like nests. One of their silk genes contains the GAGAGS motif, also found in the fibroin of *Bombyx mori*, while another has a high abundance of serine, similar to caddisfly fibroin—caddisflies also produce silk underwater (Kakui *et al.* 2021). These examples illustrate the interconnected relationships among amino acid sequence properties, physical characteristics, silk utilization, and the environmental contexts.

1.2 Human uses of silk

Due to its remarkable mechanical performance and aesthetic appeal, silk has been employed by humans for a wide range of purposes for thousands of years. Sericulture—the deliberate rearing

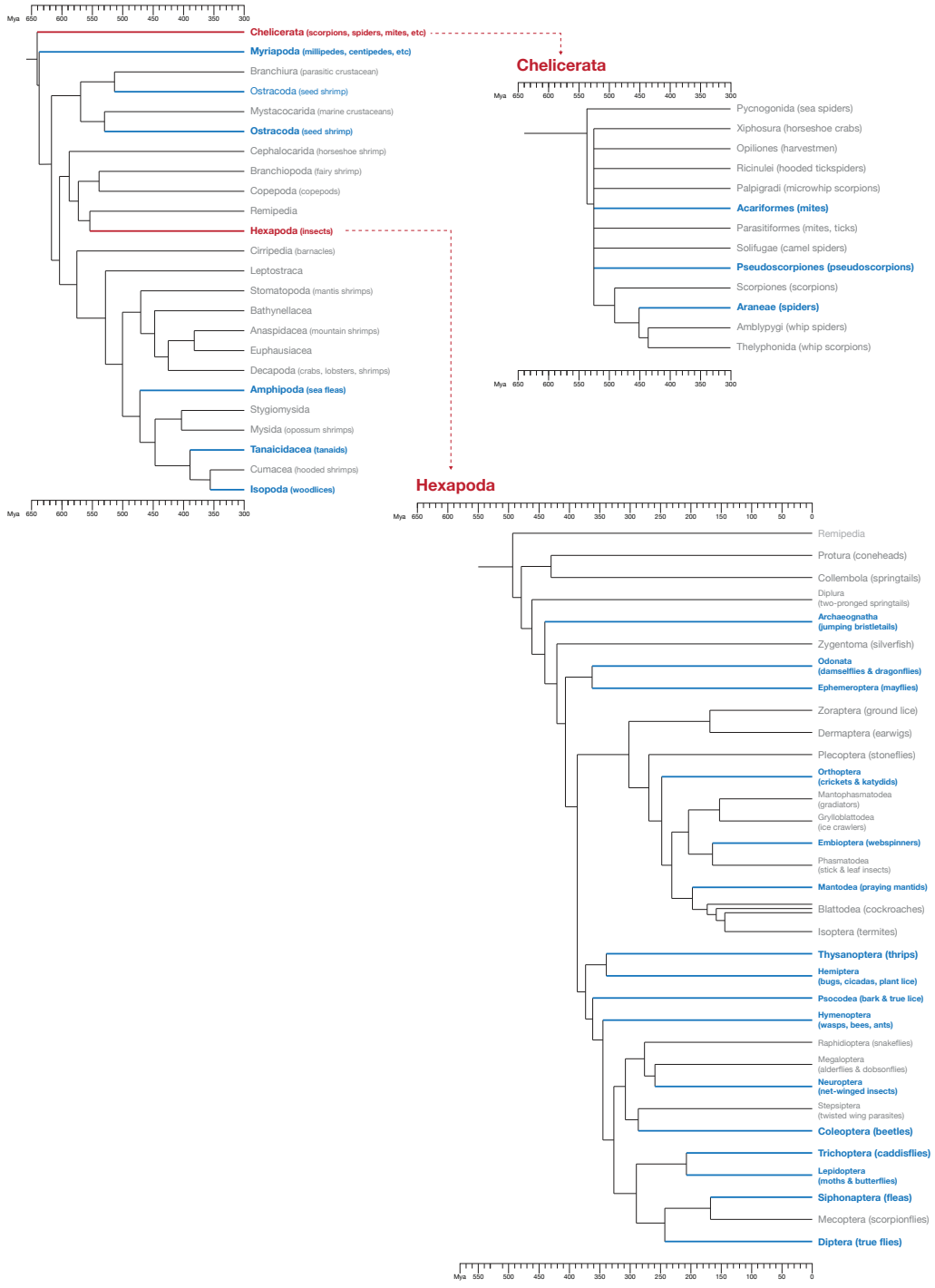

Figure 2-1. Time-calibrated phylogeny of arthropods that produce silk.

Taxa at the subphylum and order levels with silk-spinning members are shown in bold blue lines. The horizontal axis denotes approximate divergence times (in millions of years). The overall arthropod phylogeny is taken from Giribet and Edgecombe (2019), the Chelicerata phylogeny from Bernot *et al.* (2023), and the Hexapoda phylogeny from Misof *et al.* (2014).

of silkworms for fiber production—likely began between 5000 and 2000 BC (Holland *et al.* 2019). Since then, people have used *Bombyx mori* silk, along with wild silks such as that of *Antheraea yamamai*, for textiles and medical applications (e.g., wound dressings and sutures). In recent decades, research and development of silk have expanded even further: films, nanoparticles, scaffolds and hydrogels have been proposed for tissue engineering, optics and food coatings, among other uses (Guidetti *et al.* 2022).

Unlike the plant-feeding *B. mori*, spiders are carnivorous and cannibalistic, making large-scale cultivation impractical. Consequently, spider-silk applications have remained limited. Historical records indicate that ancient Romans and Greeks bundled spider silk to dress wounds (Holland *et al.* 2019), and artisans recently created a cape woven from golden-orb-weaver silk (Guessous *et al.* 2024). Nevertheless, industrial use has not materialized because spider silk cannot be produced at scale. Despite this hurdle, the extraordinary mechanical properties of spider silk, and the growing demand for environmentally sustainable alternatives to petrochemically derived synthetic fibers have long attracted scientific and commercial interest. For decades, researchers have pursued recombinant strategies to manufacture "artificial" spider silk, and recent technological advances are finally making large-scale production a realistic prospect (Guessous *et al.* 2024).

1.3 Physical properties of the silk

Physical properties of fibers are used to evaluate their performance. These include mechanical properties, which describe how a fiber responds to physical displacement, and supercontraction, which measures the reaction to water and humidity of the fibers. Figure 1-2A shows the method used to test mechanical properties of fiber, and the resulting stress–strain (SS) curve, which represents the measured data.

First, the fiber is clamped at both ends and pulled until it breaks. During this test, a load cell records the force applied. This force is then normalized by the cross-sectional area of fiber; the resulting value is called stress. The displacement of the fiber is also recorded, and strain is calculated by dividing the change in length (displacement) by initial length of the fiber. Plotting stress against strain produces the SS curve, which is essential for characterizing the mechanical properties of fibers. From this curve, one can determine Young's modulus and toughness. The Young's modulus reflects stiffness and is obtained from the slope of the initial region of the curve up to the yield point. Toughness represents the amount of energy the fiber can absorb before breaking, calculated as the area under the SS curve.

Another important physical property of spider silk is supercontraction—the phenomenon in which the fiber shrinks upon immersion in water. This property reflects the response to moisture of the fiber. As illustrated in Figure 1-2B, supercontraction is measured by comparing the length of fiber before and after immersion, yielding a percentage of contraction. Typically, further

shrinkage occurs as the fiber dries, so the total contraction percentage is measured after drying the fiber overnight. This final value is recorded separately from the initial percentage of contraction.

1.4 Spider silk

Araneae are a notable group of arthropods that utilize silk in a variety of ways, producing different types of silk for various functions. An individual spider can spin up to eight distinct types of silk (Kovoor and Peters 1988) for tasks such as prey capture, draglines, egg protection, and web construction (Eberhard 2020). These silk types include major ampullate silk (MA-silk), minor ampullate silk (MI-silk), flagelliform silk, cylindrical silk, aciniform silk, pyriform silk, cribellate silk, paracribellate silk, and pseudoflagelliform silk. In addition to these nine types of silk, viscid orb-weavers (Araneoidea) use aggregate glue in the sticky spiral rather than the cribellate silk. Figure 1-3 illustrates the silks used by both a typical ecribellate (araneoid) and cribellate (uloborid) spider. *Polenecia producta*, a species known to produce the greatest variety of silk types and silk glands, has eight distinct silk types and nine distinct silk glands, including two types of aciniform silk glands (Kovoor and Peters 1988). Because each silk type serves specialized purposes, the physical properties of spider silk are highly divergent (Denny 1976; Work 1977; Stauffer, Coguill and Lewis 1994; Blackledge and Hayashi 2006). MA-silk is employed for constructing the orb web frame and the dragline, while MI-silk is used for the temporary spiral of the orb web, bridging lines, and components of prey capture threads. Flagelliform silk, together with sticky glue from the aggregate glands, forms the sticky spirals of the orb web. Aciniform silk is found in prey capture threads and the inner egg-sac layers, whereas cylindrical silk forms the outer layer of the egg sac. In cribellate spiders, the sticky spiral consists of pseudoflagelliform silk, paracribellate silk, and cribellate silk (Joel *et al.* 2015), whereas ecribellate spiders use the flagelliform silk and aggregate glue for the sticky spiral. Although the functions and physical properties of these silks differ greatly, all spider silk types represent a synapomorphic trait, as they share a family of homologous proteins known as spidroins. This synapomorphy distinguishes spider silks from other silks, which evolved convergently. In the following section, I describe the two types of ampullate silk—MA-silk and MI-silk—that are the primary focus of this thesis. I subsequently describe the fiber's hierarchical structure, followed by its major constituent protein, spidroin.

1.4.1 Major ampullate silk (MA-silk)

Major ampullate silk (MA-silk), also known as dragline silk, is the most extensively studied type of spider silk. Spiders use MA-silk as draglines and for supporting lines in orb webs (Figure 1-3) (Denny 1976; Work 1977). Along with the superior mechanical properties, MA-silk is known for the phenomenon called "supercontraction" in which the silk can shrink in length by up to 60.4% when immersed in water (Arakawa *et al.* 2022). Since initial finding of Work (1977), this

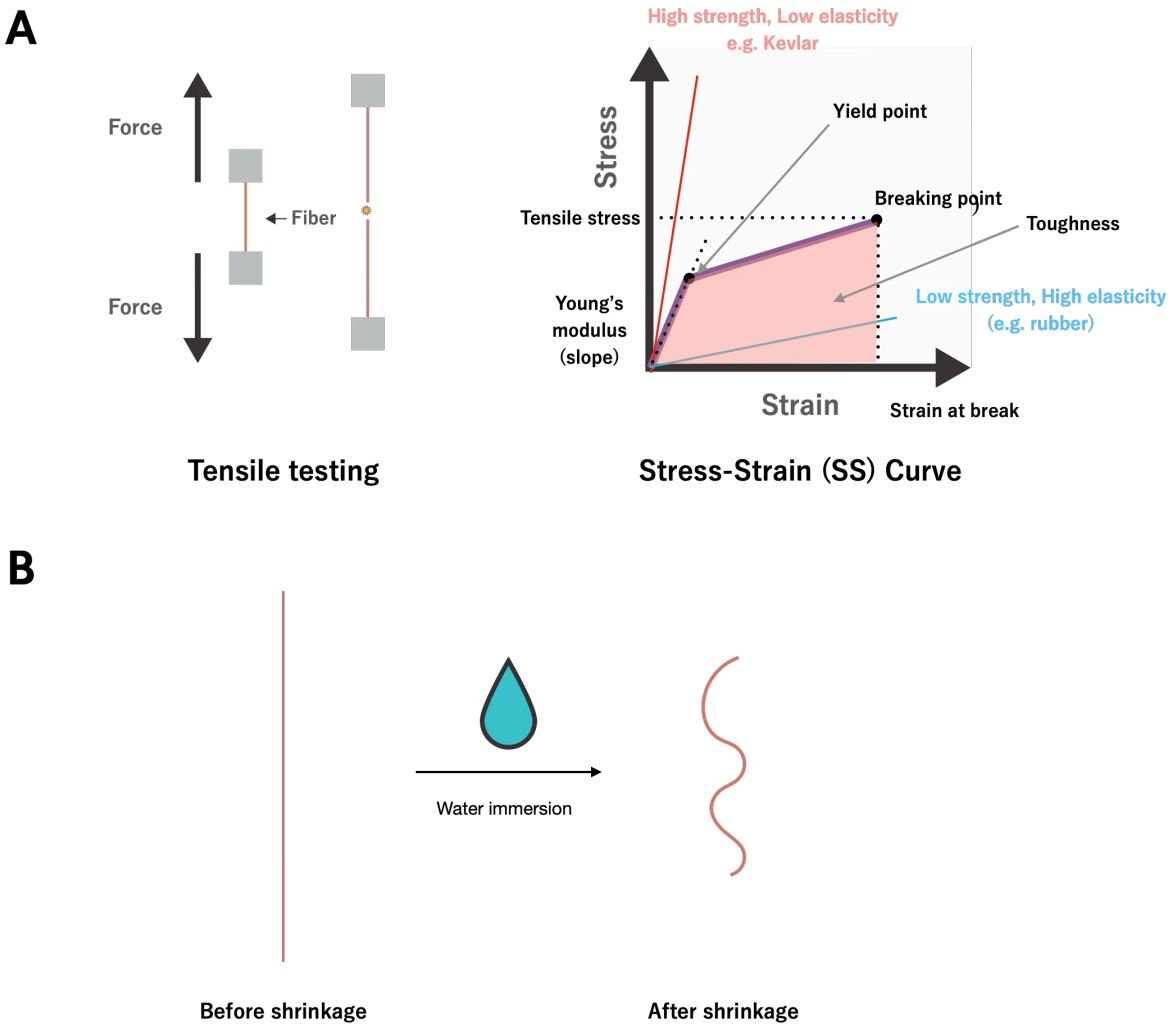

Figure 2-2. Physical properties of the silk.

A) Schematic diagram of tensile testing and the resulting stress-strain (SS) curve. The fiber is fixed and pulled along its axis, while load cells record the force until the fiber breaks. The resulting plot of stress versus strain (the SS curve) represents the mechanical properties of the fiber. B) Schematic diagram illustrating supercontraction. When the fiber is immersed in water, it shortens and becomes thicker. The ratio of the fiber length before and after shrinkage is used to represent the degree of supercontraction.

phenomenon has been extensively studied for many years (Work 1977, 1981; Guinea *et al.* 2005; Boutry and Blackledge 2010; Guan, Vollrath and Porter 2011; Cohen, Levin and Eisenbach 2021; Fazio *et al.* 2022). Supercontraction reduces the tensile strength of MA-silk, while simultaneously increasing the strain at break (Liu, Shao and Vollrath 2005). The reason for this behavior has been widely debated: some researchers contend that supercontraction is an essential constraint for achieving the high tensile strength observed in dried silk (Liu, Shao and Vollrath 2005), whereas others propose it serves a functional role by helping wet orb webs retain their shape and improve prey capture performance (Work 1981; Boutry and Blackledge 2013). The main components of MA-silk are a family of spidroins called major ampullate spidroins (MaSp). MaSp contain poly-alanine antiparallel β-sheet regions (crystalline regions) and glycine-rich amorphous regions (Simmons, Ray and Jelinski 1994; Grubb and Jelinski 1997; Riekel *et al.* 1999; Sampath *et al.* 2012). The hierarchically structured, highly ordered semi-crystalline architecture of MaSp is believed to be responsible for the mechanical properties of the silk (Van Beek *et al.* 2002; Lin *et al.* 2017). Previously, MA-silk was thought to be composed of two MaSp subfamilies, MaSp1 and MaSp2, each with distinct motifs in the amorphous regions. MaSp1 contains GGX motifs, whereas MaSp2 has GPGXX and QQ motifs (Gatesy *et al.* 2001; Malay, Arakawa and Numata 2017). The GPGXX motifs of MaSp2 form β-turn structures associated with the elasticity of MA-silk (Savage and Gosline 2008a; Jenkins *et al.* 2010), while MaSp1 is considered responsible for tensile strength due to the tight packing of the β-sheet crystallites (Van Beek *et al.* 2002). Proline in the GPGXX motif of MaSp2 is thought to play an important role in the supercontraction phenomenon (Liu *et al.* 2008), along with GXG motifs in MaSp1 (Guan, Vollrath and Porter 2011). Recently, multi-omics studies have revealed that MaSp3 is another main component of MA-silk, along with a non-spidroin proteins called SpiCE (Spidroin Constituent Element) (Kono *et al.* 2019, 2021a). The precise function of MaSp3 remains uncertain, although studies suggest a possible correlation between MaSp3 and the tensile strength of MA-silk (Kono *et al.* 2019; Arakawa *et al.* 2022). Furthermore, previous research indicates that SpiCE significantly influences the mechanical properties of MA-silk (Kono *et al.* 2021a)

1.4.2 Minor ampullate silk (MI-silk)

Minor ampullate silk (MI-silk) is another type of ampullate silk. Although the minor ampullate gland is similar in morphology to the major ampullate gland, it is smaller in size (Kovoor 1987). MI-silk serves multiple functions, including use as the temporary spiral of the orb web (Figure 1-3), as bridging lines, and as prey-wrapping silk. During orb-weaver web construction, spiders build a non-sticky (auxiliary) spiral to reinforce the radii and strengthen the web (Zschokke and Vollrath 1995). In most orb-weaver species, this non-sticky spiral is removed when the sticky spiral is added(Andersen 1970), hence the term “temporary spiral.” Spiders also use MI-silk to form bridging lines when traveling between distant locations. Observations of spider spigots under a

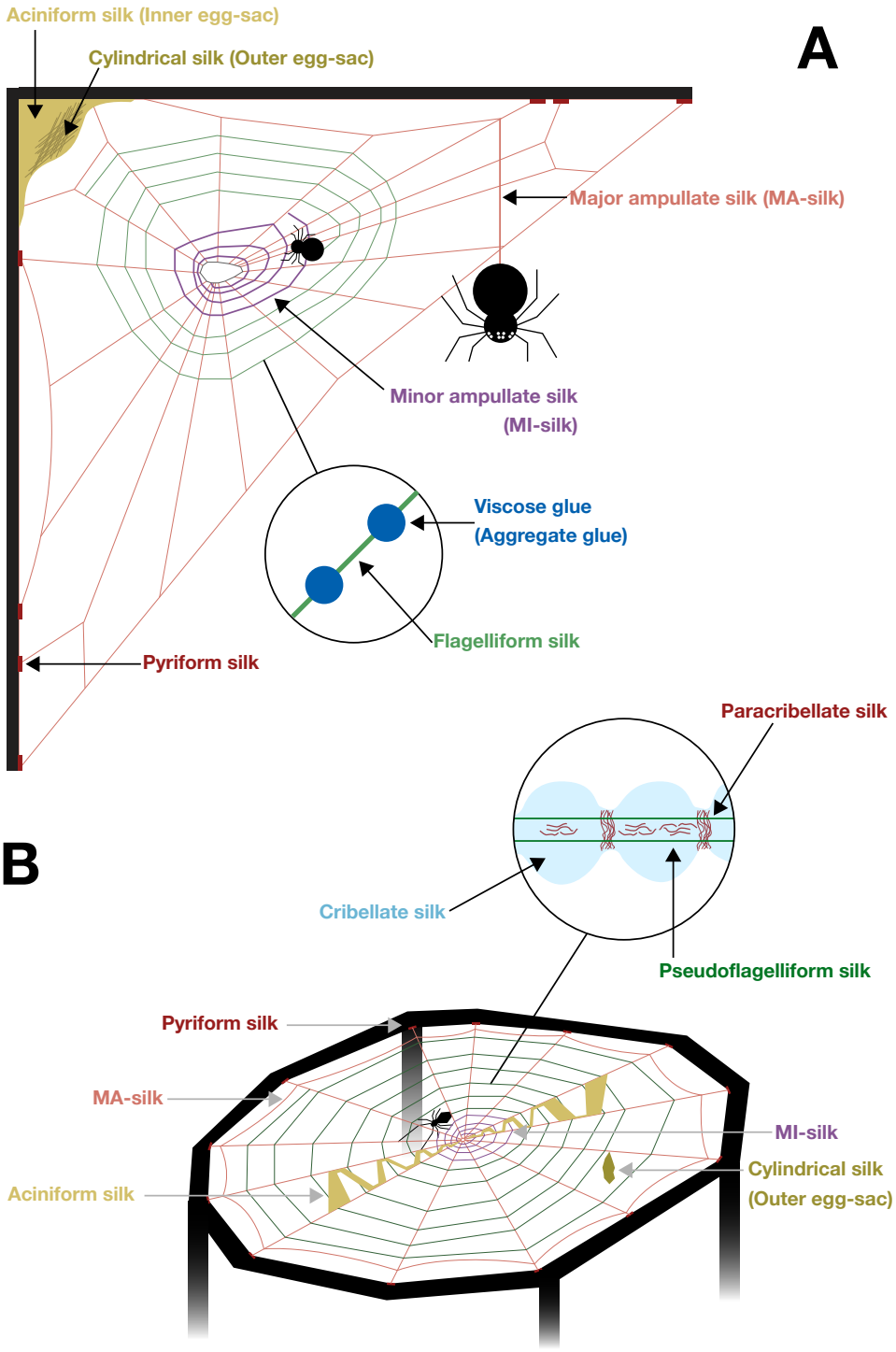

Figure 2-3. Schematic diagram of the types of silk and their usage in the orb webs of araneoid and uloborid spiders

A) Orb web of araneoid spiders. MA-silk forms the main framework of web and dragline, while MI-silk is used for the temporary spiral. Flagelliform silk coated with viscous (aggregate) glue makes up the sticky spiral for prey capturing. Aciniform silk lines the inner layer of the egg sac, and cylindrical silk creates the outer layer of the egg sac. Pyriform silk anchors these threads to the substrate. B) Orb web of uloborid spiders. Unlike araneoid spiders, the sticky spiral consists of paracribellate silk, cribellate silk, and pseudoflagelliform silk.

scanning electron microscope revealed that the main component of these bridging lines is MI-silk (Peters 1990). In addition, La Mattina and colleagues discovered that prey-wrapping silk contains both MI-silk and aciniform silk, suggesting that MI-silk reinforces aciniform silk to better immobilize large prey (La Mattina *et al*. 2008). The stress-strain curve of MI-silk differs from that of MA-silk: MI-silk has lower tensile strength but greater extensibility (Blackledge and Hayashi 2006). It also has a smaller diameter; for example, in *Araneus diadematus*, the diameter of MA-silk is 2.71 μm, whereas MI-silk measures 1.22 μm (Work 1977). Another critical difference is their reaction to water. While MA-silk exhibits a high degree of supercontraction, supercontraction of MI-silk is significantly lower (Work 1977; Guinea *et al*. 2012). In *Trichonephila inaurata*, for instance, MA-silk shows 41 ± 1% total contraction after drying, whereas MI-silk shows only 13.4 ± 0.5% (Guinea *et al*. 2012). The main component of MI-silk is minor ampullate spidroin (MiSp). Although both MaSp and MiSp contain polyalanine crystalline regions—and wide-angle X-ray scattering (WAXS) reveals a similar semi-crystalline structure (Sampath *et al*. 2012) —MiSp features poly-GQ motifs in its primary sequence. Solid-state NMR data suggest these poly-GA motifs adopt β-sheet structures. Based on these findings, Holland *et al*. concluded that the higher poly-GA content in MI-silk explains its distinct reaction to water compared to MA-silk (Holland *et al*. 2008).

1.4.3 Hierarchical structure of spider silk

Like many biomaterials, spider silk exhibits a hierarchical structure. Using atomic force microscopy (AFM), Li *et al*. (1994) observed a fibrillar structure in longitudinal sections and distinct force interactions between the core and outer regions in 90° cross-sections of major ampullate (MA) silk from *Trichonephila clavipes*, attributing these differences to variations in protein composition. Sponner *et al.* (2007) reported both a fibrillar structure and a layered architecture using several imaging methods: after removing the outermost layer with ether, they found that it did not take up the lipophilic dye oil red, concluding that this layer consists of lipids. Treating the second layer with Concanavalin A yielded a positive reaction, indicating a glycoprotein composition. Antibodies against MaSp1 and MaSp2 applied to MA-silk cross-sections revealed different distributions of these spidroins under TEM. On the basis of these findings, the authors argued that the fiber surface bears a lipid–glycoprotein coat and that the inner and outer protein layers contain distinct spidroin components. Lin *et al.* (2017) used AFM to show that microfibrils are assembled from homogeneous granules about 100 nm in diameter and that similar granules are present in the storage sac and tapering duct of the MA gland. Sonavane *et al.* (2024), employed spatial transcriptomics to reveal location-dependent gene-expression patterns within the major ampullate gland of *Larinioides sclopetarius*. They also showed that MA silk dissolved in different concentrations of urea exhibits distinct protein compositions, which they attributed to layer-specific spidroin distribution. Although the presence of a fibrillar structure in

spider silk is widely accepted and has been repeatedly confirmed by various methods, whether proteins are differentially distributed within the fiber remains a topic of active discussion and is not yet resolved.

The hierarchical organization is widely believed to underlie the exceptional mechanical properties of MA-silk. Li *et al.* suggested that the highly ordered fibrils contribute to the high tensile strength and elasticity of MA-silk, whereas Lin *et al.* argued that fibrils composed of nanometer-scale granules help to explain the remarkable toughness of MA-silk. In materials science, hierarchical structuring is a well-established strategy for enhancing toughness and is considered a hallmark of many biomaterials (Ritchie 2011; Sen and Buehler 2011). With respect to the skin layer, Yazawa *et al.* (2019) showed that removing it has no measurable effect on the mechanical properties of MA-silk, indicating that the skin contributes little to the mechanical property.

1.4.4 Spidroin

In the spider silk gland, silk is stored as a highly concentrated (30–50%) aqueous solution (Vollrath and Porter 2006). Spidroin is the primary component of this solution and solidifies when spiders spin silk from the spigots on their spinnerets. Spidroins are high molecular weight proteins (several hundred kDa) composed of an N-terminal domain (NTD), a repetitive region, and a C-terminal domain (CTD) (Figure 1-4). The NTD and CTD—both non-repetitive domains—are critical for transforming soluble protein solutions into solid fibers during silk spinning, and each domain contains multiple alpha-helices (Askarieh *et al.* 2010; Hagn *et al.* 2011). Within the silk gland sac at pH 7, the NTD is monomeric. When the pH drops to 5.5 in the spinning duct, the NTD dimerizes (Kronqvist *et al.* 2014; Oktaviani *et al.* 2023). As for the CTD, structural unfolding is observed under low pH, shear force, and higher salt concentrations—conditions believed to initiate fiber formation (Hagn *et al.* 2010; Andersson *et al.* 2014). Malay et al. (2020) found that the NTD drives nanofibrillar network formation, while the CTD and the repetitive region are responsible for liquid–liquid phase separation (LLPS) (Malay *et al.* 2020). The repetitive regions comprise approximately 90% of the spidroin sequence and underlie much of the variation in the mechanical properties of the silk (Guerette *et al.* 1996; Gatesy *et al.* 2001; Tian and Lewis 2005). Although the NTD and CTD are conserved across spidroin families, the repetitive regions exhibit high diversity among spidroin types and spider species. These repetitive regions include both crystalline and amorphous parts. In MaSp (the spidroin of MA-silk) and MiSp (the spidroin of MI-silk), the crystalline regions are composed of polyalanine (poly-Ala), whereas the amorphous regions are glycine-rich (Figure 1-4) (Simmons, Michal and Jelinski 1996; Sampath *et al.* 2012). Specific sequence motifs in the amorphous regions differ among spidroin families and species, influencing the physical properties of spider silk (Gatesy *et al.* 2001; Malay, Arakawa and Numata 2017; Craig *et al.* 2020; Arakawa *et al.* 2022)

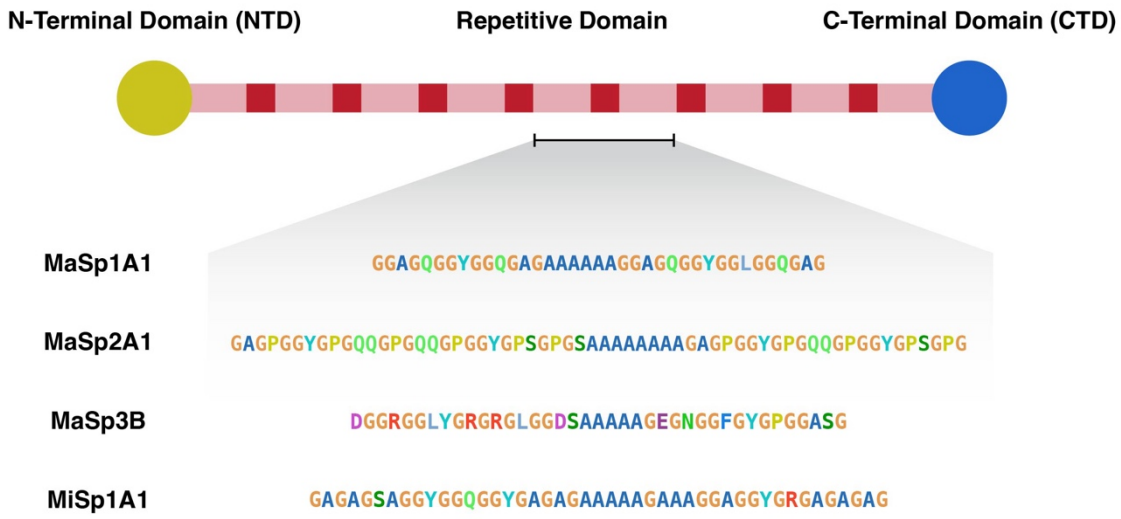

Figure 2-4. Schematic of spidroin domain organization and representative repetitive-region sequences from *Trichonephila clavata*.

Each spidroin monomer comprises an N-terminal domain (NTD) (yellow circle), a repetitive domain (pink/red bars), and a C-terminal domain (CTD) (blue circle). The crystalline region of the repetitive domain is shown in red, and the amorphous region is shown in pink. Below are partial amino acid sequences from the repetitive regions of four *T. clavata* spidroins: MaSp1A1, MaSp2A1, MaSp3B1, and MiSp1

1.5 Artificial spider silk

1.5.1 Techniques and advances in artificial spider silk spinning

Artificial spider silk refers to fibers produced from recombinant spidroins through artificial silk-spinning processes. In these processes, organic solvents are used to prepare a "spinning dope" from recombinant spidroins, which is then extruded into coagulation baths where it precipitates into fiber form (Koeppel and Holland 2017). Common solvents include hexafluoroisopropanol (HFIP) (Xia *et al.* 2010; Lin *et al.* 2013), DMSO with inorganic salts (Kono *et al.* 2021a; Nakamura *et al.* 2023), trifluoroacetic acid (TFA)/2,2,2-trifluoroethanol (TFE)/H_2O (Simmons, Xu and Rainey 2019), formic acids (Asakura *et al.* 2022a), or aqueous solutions such as phosphate-buffered saline (Lazaris *et al.* 2002). The spinning dope is extruded into coagulation baths containing solvents like methanol, ethanol, or isopropanol. Because this approach differs from natural silk spinning, the NTD and CTD of the spidroins become denatured, preventing the fibrillation and hierarchical structure formation observed in natural spider silk. As discussed in a review by Koeppel, early efforts to improve artificial spider silk focused on increasing the molecular weight of the recombinant protein (Koeppel and Holland 2017). For example, Xia et al. employed a 284.9 kDa recombinant spidroin to create fibers with a tensile strength of up to 508 MPa (Xia *et al.* 2010), whereas Bowen *et al*. produced a 556 kDa recombinant spidroin using split intein–mediated ligation, achieving a tensile strength of 1030 MPa (Bowen *et al.* 2018). More recently, researchers have modified the amino acid sequence of recombinant spidroins to alter mechanical properties: Hu *et al*. adjusted the number of alanine residues in the polyalanine motifs to customize fiber performance (Hu *et al.* 2024), and Li *et al*. replaced polyalanine motifs with peptides derived from human islet amyloid peptide (hIAPP) and amyloid beta (Aβ) to increase tensile strength (Li *et al.* 2021). Johansson and Rising propose optimizing crystal region with hydrophobic residues to increase strength of β-sheet (Johansson and Rising 2021).

To overcome the limitations of artificial spinning—particularly the lack of hierarchical structures observed in natural spider silk—biomimetic spinning processes are under development. Unlike artificial methods, biomimetic spinning leverages the natural roles of the NTD and CTD in fiber solidification. Andersson *et al*. spun fibers in an aqueous buffer with reduced pH using a chimeric mini-spidroin solution (Andersson *et al.* 2017), and Saric *et al*. used co-expressed eADF3 and eADF4 to achieve a tensile strength of 834 MPa (Saric *et al.* 2021). This biomimetic approach can recreate hierarchical structures and may resolve some shortcomings of purely artificial methods, making it a current focus of active research.

1.5.2 Sustainability and industrialization

Alongside advances in artificial spider silk, concern has grown over marine pollution caused by discarded synthetic fibers (Andrady 2011; Belzagui *et al.* 2019; Lim 2021). Additionally, man-made fibers often lack biodegradability (Chamas *et al.* 2020), and their production relies on petrochemicals, leading to greenhouse gas emissions associated with petroleum consumption. In response, the textile industry is increasingly seeking eco-friendly alternatives (European Commission *et al.* 2024). Spider silk represents a promising candidate because it can be produced as fibers with varying mechanical properties through a single process, is biodegradable, and does not rely on petrochemical resources.

Recent industrial-scale efforts to produce artificial spider silk have shown promise, as several startup companies are now developing products for the textile sector (Figure 1-5) (Guessous *et al.* 2024). Industrialization requires upscaling recombinant protein production while simultaneously controlling mechanical properties for broader applications, including automotive uses. These goals can conflict; for instance, increasing the molecular weight of recombinant proteins generally boosts tensile strength but often reduces expression levels (Hauptmann *et al.* 2013; Bowen *et al.* 2018). Hence, novel strategies for tuning mechanical properties are needed to balance these competing demands.

1.6 The physical properties, structural properties, and sequence relationships of natural spider silk

The physical properties and primary sequence relationships of MA-silk have been extensively studied. Even within the same silk type, interspecific variations can result in significant differences in mechanical properties (Madsen, Shao and Vollrath 1999). Blackledge *et al*. proposed that the mechanical enhancement of MA-silk corresponds to the sequential evolution of major ampullate spidroins (Blackledge *et al.* 2012). Comparative studies of mechanical properties and spidroin sequence relationships in various spider species indicate that physical properties of the silk are largely governed by differences in spidroin sequences and the resulting fiber structures (Gatesy *et al.* 2001; Craig *et al.* 2020; Arakawa *et al.* 2022). Focusing on over 1,000 spiders, Arakawa *et al*. correlated spidroin sequences with the mechanical properties of MA-silk, performing statistical analyses to determine how motif content relates to these physical properties. Araneoidea spiders, for instance, exhibit higher silk toughness than other spider families, primarily due to the presence of MaSp3—one of the main spidroins, alongside MaSp1 and MaSp2. The researchers also found correlations between motif content and mechanical properties such as tensile strength, Young's modulus, strain at break, and toughness. For example, the GYGQGG motif in MaSp1 showed a strong correlation with both tensile strength and strain at break, ultimately influencing toughness (Arakawa *et al.* 2022).

Figure 2-5. The industrial application of the artificial spider silk.

The jacket, released by GOLDWIN in collaboration with the Japanese biotechnology startup Spiber Inc., represents an early example of the industrial application of artificial spider silk.

Supercontraction also exhibited a strong link to amino acid sequence, with the length of the polyalanine region showing a negative correlation with supercontraction. Overall, these findings underscore that both MaSp composition and motif content in spidroin sequences are closely tied to the mechanical properties of MA-silk.

1.7 Aims and scope of the thesis

This thesis aims to establish a method for controlling the mechanical properties of artificial spider silk by leveraging sequence–property relationships found in natural spider silk. Currently, efforts to enhance the physical properties of recombinant proteins typically involve increasing their molecular weight or modifying their crystalline regions with various sequence motifs. Although these approaches have successfully improved properties such as tensile strength, they are not without potential drawbacks. For instance, elevating the molecular weight generally reduces the expression level of recombinant proteins, posing challenges for large-scale production. Radically modifying the crystalline regions can also lead to unexpected issues in protein production, even in prokaryotic systems. Consequently, any sequence modifications must remain compatible with established production processes. Furthermore, while these attempts have chiefly targeted tensile strength, no methods exist for the precise and independent fine-tuning of other physical properties. To meet the demands of diverse industries—from textiles to automotive—strategies that enable the discrete optimization of specific mechanical properties are essential. To achieve this, validating the sequence–property relationship in both natural and artificial spider silk is crucial. Accordingly, this study examines two spider silk types—MA-silk and MI-silk—which differ in their physical properties. These differences, observed in natural silks, were then replicated using recombinant mini-spidroins to produce artificial spider silk. Subsequently, the sequence–property relationships gleaned from analyzing the physical properties and spidroin sequences of 1,000 spider species were used to design artificial mini-spidroins. This approach facilitated the control of physical properties in artificial spider silk, guided by insights from natural spider silk.

Minor ampullate silk is one of several silk types produced by spiders, yet it exhibits mechanical properties distinct from those of MA-silk. Unlike MA-silk, MI-silk does not undergo supercontraction. Although prior research has highlighted the physical differences between MA- and MI-silks, direct evidence linking these differences to protein composition has been limited. This thesis addresses that gap using a multi-omics approach to elucidate the origins of their divergent properties. Furthermore, it demonstrates how sequence–property relationships can be employed to regulate the physical properties of artificial spider silk (Chapter 2)

Controlling mechanical properties such as tensile strength and strain at break is paramount for expanding the utility of artificial spider silk in industries requiring exceptional performance, including the automotive sector. To develop methods for precise control, we utilized data from

1,000 spider species worldwide, correlating the mechanical properties of MA-silk with their spidroin sequences. Building on earlier studies linking specific sequence motifs to mechanical properties, we devised a motif-substitution-based design strategy for artificial spider silk. By applying these insights to MaSp2-derived artificial mini-spidroins, we confirmed that the sequence–property relationships found in natural spider silk are critical in influencing the mechanical properties of artificial spider silk (Chapter 3). The findings are expected to advance the industrial application of artificial spider silk, as motif-substitution-based sequence design enables the tailoring of mechanical properties to meet diverse requirements.

Chapter 2
Composition of minor ampullate silk makes its properties different from those of major ampullate silk

2.1 Introduction

Major ampullate silk (MA-silk) and minor ampullate silk (MI-silk) are two types of silks produced by major and minor ampullate glands. MA-silk is used as the dragline or in the construction of the radii, frame and anchor lines of orb webs (Denny 1976; Eberhard 2020). MA-silk is known for its substantial toughness, combining high tensile strength and high elasticity (Denny 1976; Gosline, DeMont and Denny 1986). The molecular structure of MA-silk is modeled as a semicrystalline material composed of recurrent β-sheet crystallites and amorphous domains (Termonia 1994). Nuclear magnetic resonance (NMR) and wide-angle X-ray scattering (WAXS) confirmed the model and assigned the β-sheet crystallite for polyalanine (Simmons, Michal and Jelinski 1996; Grubb and Jelinski 1997; Riekel *et al.* 1999). Components of MA-silk are thought to be major ampullate spidroin 1 (MaSp1) (Xu and Lewis 1990) and major ampullate spidroin 2 (MaSp2) (Hinman and Lewis 1992), which have Gly-Pro and Glu-Glu motifs in their amino acid sequence (Malay, Arakawa and Numata 2017). Recently, another type of spidroin named MaSp3 was identified in several species using target capture sequencing (Chaw *et al.* 2015; Collin *et al.* 2018). Studies utilizing a multi-omics approach revealed that MaSp3 is one of the main components of MA-silk (Kono *et al.* 2019, 2021a).

MI-silk, a comparably thinner fiber than MA-silk, is often used to construct the temporally (auxiliary) spiral, which is used during orb web building as a walking scaffold (Work 1981) and as a bridging line when reaching distant places (Peters 1990). Mattina *et al*. found using proteomic analysis that *Latrodectus hesperus* uses MI-silk as a constituent of prey-wrapping silk (La Mattina *et al.* 2008). Several lineage-specific uses are also observed, such as *Araneus diadematus* using a MA-silk and MI-silk pair to construct most radii in their orb web (Peters and Kovoor 1991). In many species of Araneoidea, temporary spirals are reported to be cut out and removed during the construction of capture spirals (Zschokke 1993); however, Nephilinae spiders do not remove this temporary spiral and retain it in their finished orb webs. Hesselberg and Vollrath reported that the mechanical properties of temporary spirals in orb webs of Nephilinae spiders are identical to those of MA-silk, suggesting that the temporary spiral might not consist of MI-silk (Hesselberg and Vollrath 2012). The ecological implications of the use of MI-silk therefore remain largely elusive,

but an economical preference in applications not requiring high tensile strength is suggested due to the reduced amount of protein by smaller diameter of the MI-silk (Eberhard 2020).

The mechanical properties of MI-silk are clearly different from that of MA-silk. It has higher elasticity and lower Young's modulus and tensile strength than MA-silk (Blackledge and Hayashi 2006), while the molecular structure of MI-silk is also a semicrystalline structure, and the crystallite is a β-sheet of polyalanine (Sampath *et al.* 2012). A known component of MI-silk is minor ampullate spidroin (MiSp), for which Colgin and Lewis reported two paralogs, namely, MiSp1 and MiSp2 from the *Trichonephila clavipes* minor ampullate gland (Colgin and Lewis 1998). Both MiSp1 and MiSp2 have GGX motifs as well as GA repeats in the amorphous domains and polyalanine in crystalline regions. MiSps often also contain nonrepetitive Ser-rich spacer regions of approximately 140 residues in length, which was suggested in a study utilizing partial recombinant proteins to be involved in fiber assembly under the existence of shear force (Gao *et al.* 2013).

The most significant difference between MA-silk and MI-silk is their reaction to water molecules. When MA-silk is exposed to water, it undergoes supercontraction up to approximately 50% of its original length. In 1977, Work reported that MA-silk undergoes supercontraction when wetted, but MI-silk shows a smaller degree of contraction than MA-silk.(Work 1977). In their comprehensive study of MA-silk and MI-silk, Guinea *et al*. confirmed that MI-silk does not have the ground state of MA-silk, and permanent deformation occurs after contraction (Guinea *et al.* 2012). The mechanical properties of MA-silk are significantly modulated after supercontraction, where the strain at break is increased and the tensile strength is decreased. The change is also known to be correlated with its capacity to shrink (Liu, Shao and Vollrath 2005); accordingly, structural analysis with WAXS and Raman spectroscopy suggest that oriented β-sheet nanocrystallites and oriented amorphous components in MA-silk lose their orientation upon supercontraction (Grubb and Ji 1999; Shao *et al.* 1999; Sampath and Yarger 2015). The loss of orientation is larger for MA-silk than for MI-silk (Sampath and Yarger 2015), mirroring the propensity for supercontraction. Several amino acid sequence motifs are suggested to be responsible for supercontraction; namely, YGGLGS(N)QGAGR of MaSp1 (Yang *et al.* 2000), GPGXX of MaSp2 (Liu *et al.* 2008) and GXG in MaSp1 (Guan, Vollrath and Porter 2011).

Quantitative and comprehensive compositional analysis of protein constituents of the spider silks is beginning to be uncovered for MA-silk, with high-quality genome data coupled with high-sensitivity mass spectrometry. Kono *et al*. reported that MA-silk contains approximately 1~5% spider-silk constituting element (SpiCE), along with various spidroin paralogs other than MaSp1 or MaSp2 (Kono *et al.* 2019, 2021a). Experiments *in vitro* with recombinant SpiCE proteins suggested that the addition of a minute (1%) amount of SpiCE to artificial silk significantly boosts its mechanical properties (Kono *et al.* 2021a). Early works on the amino acid composition of minor ampullate gland secretions were first reported by Andersen, who found that it had nearly the same

composition as fibroin from the silk of *Bombyx mori* (Andersen 1970). Work and Young performed forcible silking to separate MA-silk and MI-silk using a microscope and successfully analyzed the amino acid composition of both silks. Their observation showed that the content of proline was significantly lower in MI-silk, and the variability of amino acid composition between species was lower in MI-silk than MA-silk (Work and Young 1987). Chaw *et al*. reported proteomic analysis of MA and MI glands in *Latrodectus hesperus*, where they successfully identified multiple silk-gland specific transcripts, but the contribution of these components to the mechanical properties of the silks was yet to be explored (Chaw *et al.* 2015). It was not clear what caused MI-silk not to supercontract, as no comparison of the protein composition of MA-silk and MI-silk had been made using proteomic analysis.

To this end, we established separate silking of MA-silk and MI-silk and used this method to observe differences in the mechanical properties and proteomic compositions of MA-silk and MI-silk of *Araneus ventricosus.* Dragline silk often contains both MA-silk and MI-silk; therefore, we retrieved these silks separately under a microscope. We have especially focused on supercontraction, observing the change in mechanical properties in a time series, where we performed tensile testing 7.5 h, 24 h, and 48 h after immersion until silks were completely dried. Moreover, we analyzed the protein composition of MA-silk and MI-silk of *A. ventricosus* and *Trichonephila clavata* and analyzed the contribution of MiSp protein using recombinant silk to examine component-function relationships.

2.2 Experimental section

2.2.1 Separate forcible silking

Mature *Trichonephila clavata* females were collected in Nagoya city, Aichi, Japan in October 2019 and Tsuruoka city, Yamagata, Japan in November 2021. Mature *A. ventricosus* females originally captured in Tsuruoka city, Yamagata, Japan in September 2018 were bred and reared in the laboratory. Spiders were fed a cricket twice a week. Collection of MA-silk and MI-silk samples was conducted with the forcible silking method (Work and Young 1987; Malay *et al.* 2016; Arakawa *et al.* 2022). Spiders were gently immobilized using two pieces of sponge and locked with rubber bands and then placed under a stereomicroscope. After immobilization, silks from the targeted spinnerets were obtained by tweezers and attached to the end of the bobbin. In this step, to ensure the reeling of MA-silk and MI-silk separately, we observed spinnerets with a stereomicroscope to identify silks while reeling. To prevent contamination, we fixed either of the silks with pieces of masking tape and forcibly silked only one type at a time. For example, when we silked MA-silk from one spinneret, we fixed a pair of MI-silks and vice versa. Silking was constantly monitored under the microscope, confirming the glandular origin of silks (Figure 2-1A). Dedicated reeling devices were used for silking with a constant reeling speed (1.28 m/min).

Forcible silking was continued for 30 to 60 min. The ambient temperature was about 25°C and the relative humidity was about 30% during forcible silking. After forcible silking, the bobbin-reeled silk was put in a plastic bag and stored in a dry box (relative humidity was kept lower than 30%) at room temperature. Fibers were stored in the dry box for 4 months for subsequent analysis. The water content of *A. ventricosus* fibers ranged from 7.0% to 8.6%, according to the Spider Silkome Database (Arakawa *et al.* 2022).

2.2.2 Maximum supercontraction

The supercontraction of MA-silk and MI-silk was evaluated according to a previous method (Guinea *et al.* 2012; Arakawa *et al.* 2022). Test pieces were prepared by cutting fragments of 5 to 10 cm (L_0) from MA-silk and MI-silks reeled from *A. ventricosus.* Small pieces of masking tape were affixed on either end of the test pieces. The fibers were immersed in RO (reverse osmosis) water for 1 min to allow contraction. The length of fibers was measured (L_1) immediately after removal of water, and the percentage contraction was calculated by immersion in water as $(L_0 - L_1)/L_0 \times 100$ and then allowed to air dry for 24 hours in an unrestrained state. The final length of the fiber (L_f) was measured, and the percentage of total contraction after drying was calculated as $(L_0 - L_f)/L_0 \times 100$. Five replicates were performed for each sample. Throughout the experiment, the room temperature was 25℃ and relative humidity was around 20%.

2.2.3 Observation of the drying effect of MA-silk and MI-silk during water immersion and subsequent drying

To observe the transition of mechanical properties of contracted MA-silk and MI-silk fibers during drying after water immersion, we measured the mechanical properties of drying fibers intermittently. First, reeled MA-silk and MI-silk fibers were immersed in water. After immersion, the fibers were dried at 20 °C and 20% relative humidity in an unrestrained state. After 2.5 hours, 7 hours, and 48 hours of immersion, the mechanical properties and morphology of the fibers were analyzed with tensile tests and scanning electron microscopy (SEM). For each time point, we used at least 3 test pieces.

2.2.4 Tensile testing

The tensile properties of the fibers were measured using an EZ-S universal tester (Shimadzu, Kyoto, Japan) with a 1 N load cell in an environmental chamber kept at the same relative humidity as other experimental conditions (approximately 20%). The initial length of the single silk fiber was set to 10

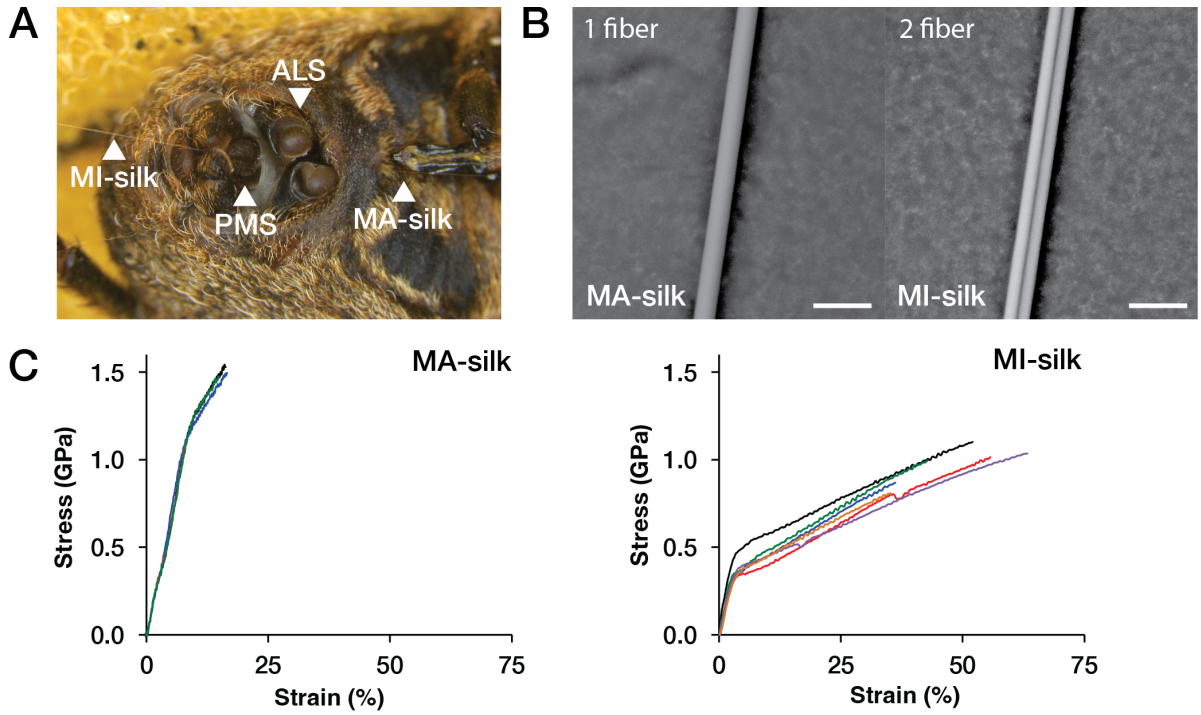

Figure 2-1. Forcible silking of *A. ventricosus* MA-silk and MI-silk, morphology, and stress-strain curve of silks.

(A) Spinnerets during separate forcible silking under the stereomicroscope. MA-silk is spun from spigots on the anterior lateral spinneret (ALS). MI-silk is spun from spigots on the posterior median spinneret (PMS). (B) SEM images showing *A. ventricosus* MA-silk and MI-silk. The scale bar is 10 μm. (C) Stress-strain curve of *A. ventricosus* MA-silk (left) and MI-silk (right). Colors indicate replicates. N = 4 for MA-silk and N = 6 for MI-silk.

mm. The extension speed was applied at 10 mm/min, and the force during testing was measured with a 1 N load cell. For MA-silk and MI-silk, the number of fibers used in the tensile test is one and two, respectively. Tensile strength, Young's modulus, strain at break, and toughness were obtained from the resultant stress-strain curves. For the calculation of tensile strength, the cross-section areas of the fiber samples were calculated based on the diameters determined by SEM observations. For MI-silk, the cross-sectional area was calculated from the diameter of 1 fiber observed by SEM. Then, the cross-sectional area of 1 fiber was doubled and used to calculate the mechanical properties. Analysis of force-displacement data and calculation of mechanical properties were conducted as previously described (Malay et al. 2016). Significant digits of mechanical properties were determined in accordance with a previous report (Arakawa *et al*. 2022).

2.2.5 SEM observation and cross-sectional area calculation

The surface morphology and cross-section of the dragline silk fibers were assessed using SEM (Phenom ProX, Thermo Fisher Scientific, Phenom-World BV, Eindhoven, The Netherlands) at V = 15 kV. Samples were mounted on an aluminum stub with conductive tape. The cross-sectional area was calculated by fiber diameter assuming a circular cross-section. The fiber diameters for calculating the cross-sectional area were measured on each micrograph using ImageJ (NIH, Bethesda, MD, USA).

2.2.6 Birefringence measurement

The retardation provided by the silk fiber was measured with a birefringence measurement system WPA-100 (Photonic Lattice, Inc., Miyagi, Japan) and was analyzed with WPA-VIEW (version 1.05) software, in accordance with a previous method (Arakawa *et al.* 2022). The birefringence of the dragline silk fiber was calculated from the retardation and silk fiber diameter, which was determined via SEM.

2.2.7 Wide-angle X-ray scattering measurement

Synchrotron WAXS measurements were conducted at the BL45XU beamline of Spring-8, Harima, Japan, in accordance with a previous report (Yazawa *et al.* 2020). The X-ray energy was 12.4 keV at a wavelength of 0.1 nm. The sample-to-detector distance for the WAXS measurements was approximately 257 mm. The exposure time for each diffraction pattern was 10 s. The resultant data were converted into one-dimensional radial integration profiles using Fit2D software (Hammersley *et al.* 1996). The resultant data were corrected by subtracting the background scattering.

2.2.8 Simultaneous wide-angle X-ray scattering-tensile test

A sample stretching apparatus (Sentech, Osaka, Japan) was placed in the experimental hutch and controlled outside of the hutch at the BL45XU beamline of Spring-8. The dragline silk fibers were attached to the stretching apparatus. The initial length of the fiber bundle between the fixtures was 13 mm. The strain rate applied to the fibers was 3.3 x 10^{-1} s^{-1}. The exposure time for each scattering pattern was 0.099 s.

2.2.9 Expression and purification of recombinant spidroins

A MiSp recombinant protein with optimized sequences based on *Trichonephila clavipes* was used for the artificial silk. Targeting a size of approximately 50 kDa, we reduced the number of repetitive units of *T. clavipes* MiSp1A1 to seven while keeping the N- and C-terminal domains. The mini-spidroin gene is composed of a 6x His tag (MHHHHHH), a linker (SSGSS), the N-terminal domain, repetitive units, and the C-terminal domain. The complete amino acid sequences used in the article are shown in Figure 2-2. The MaSp1, MaSp2, and MiSp recombinant protein was produced and purified as described previously (Kono *et al.* 2021a). First, designed amino acid sequences were converted to nucleotide sequences. Nucleotide sequences were adapted to *Escherichia coli* codon usage. Oligonucleotide fragments were provided by Fasmac Co. (Kanagawa, Japan) and were then assembled by the overlap extension PCR method (Bryksin and Matsumura 2010). The assembled sequences were cloned into pET-22b (+). The clones were transformed into *E. coli* BLR (DE3). The cells were cultured in a 10-L jar fermenter (Takasugi Seisakusho Co. Ltd.) containing 5.7 L of medium. The medium contained 2.0 g/L glucose, 9.0 g/L KH_2PO_4, 15 g/L yeast extract, 0.04 g/L $FeSO_4$ $7H_2O$, 0.04 g/L $MnSO_4$ $5H_2O$, 0.04 g/L $CaCl_2$ $2H_2O$, GD-113 (NOF Corporation, Tokyo, Japan) at 37°C. The feeding rate, oxygen concentration, and pH configuration used in the fermentation were the same as in the previous study. After 24 h of fermentation, protein expression was induced by adding isopropyl-β-D-thiogalactoside (IPTG). The final concentration of IPTG was 0.1 mM. After 24 hours of induction, the cells were centrifuged and resuspended in lysis buffer containing 20 mM Tris-HCl, 100 mM NaCl, DNase, lysozyme, and phenylmethylsulfonyl fluoride according to the conditions used in the previous study. After the cells were agitated at 37 °C overnight, they were harvested and resuspended in the 50 mM Tris-HCl buffer containing 100 mM NaCl and 3% (w/v) sodium dodecyl sulfate (SDS), and then the pellets were harvested. The pellets were incubated in DMSO containing 1 M LiCl for 30 min at 60 °C. After ethanol precipitation on the supernatant, the solution was centrifuged at 11,000 xg for 30 min. The precipitation was corrected and washed with reverse osmosis purified water, and lyophilization was performed. For the spinning experiment, lyophilized powders were used.

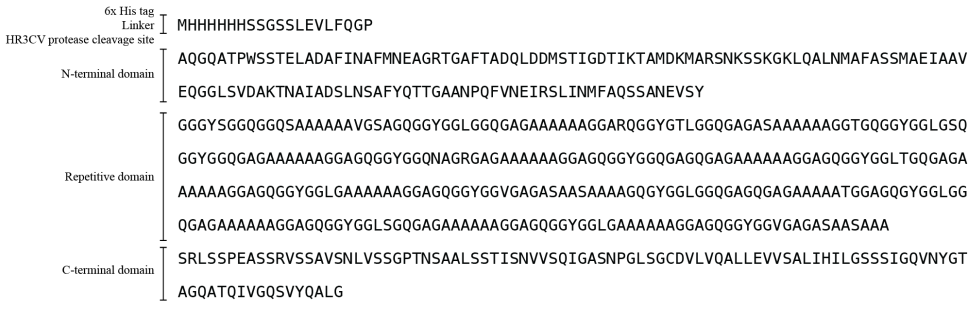

MaSp1 mini-spidroin (*Trichonephila clavata*)

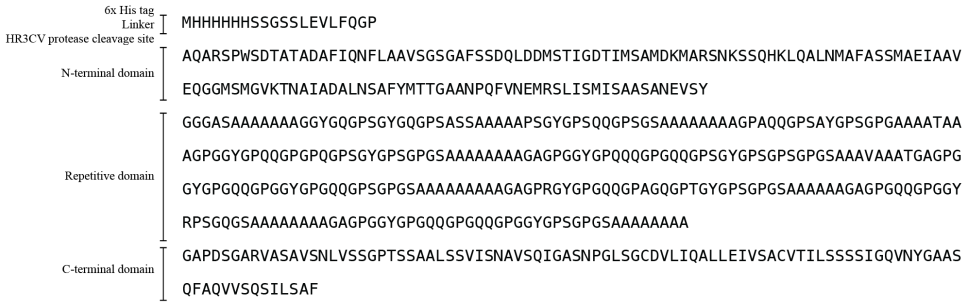

MaSp2 mini-spidroin (*Trichonephila clavata*)

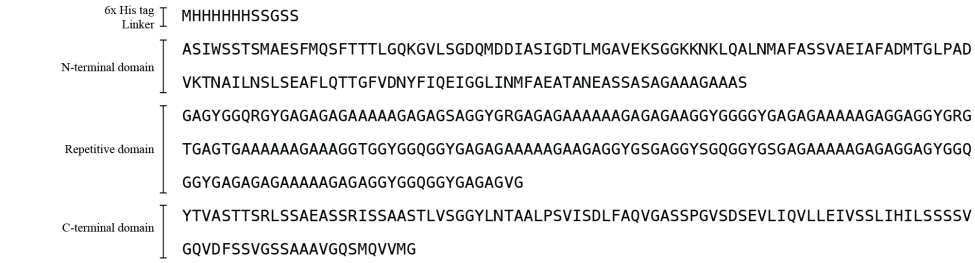

MiSp mini-spidroin (*Trichonephila clavipes*)

Figure 2-2. The amino acid sequences of the recombinant mini-spidroins MaSp1, MaSp2, and MiSp are used in this article.

The annotation of the domains in the sequences are shown in the left column. The amino acid sequences are shown in the right column.

2.2.10 Production of fibers from recombinant spidroins

Lyophilized recombinant MiSp, MaSp1, and MaSp2 proteins of 15% (w/w) were dissolved in DMSO and 2 M LiCl and stirred for 30 min at 80 ℃. The dope was extruded by an N2 pump with a D = 0.1 mm needle at 80 ℃ and spun directly into the first coagulation bath comprising MeOH. Fibers were coagulated with a second coagulation bath also comprising MeOH and then washed and stretched in a water bath up to 6x.

2.2.11 Proteome analysis

Sample preparation for proteome analysis of MA-silk and MI-silk was performed as previously described (Kono *et al.* 2021b). Briefly, reeled silk samples were immersed in 6 M guanidine-HCl buffer (pH 8.5) for MA-silk and 9 M LiBr for MI-silk, followed by freezing and freezing in liquid nitrogen. The samples were thawed and subjected to sonication using a Bioruptor II (BM Equipment Co., Ltd., Tokyo, Japan) for protein extraction. After centrifugation at 15,000 x g for 10 min, the protein concentration of the supernatants was quantified using a Pierce BCA Protein Assay Kit (Thermo Scientific). The extracts containing 10–50 μg of protein were reacted with DTT for 30 min at 37 ℃ followed by iodoacetamide for 30 min at 37 ℃ in the dark. After 5-fold dilution with 50 mM ammonium bicarbonate, the proteins in the samples were digested with chymotrypsin for 16 h at 37 °C. The enzymatic digests were acidified by trifluoracetic acid and desalted using C18 StageTips (Rappsilber, Ishihama and Mann 2003). Nano liquid chromatography tandem mass spectrometry (nanoLC–MS/MS) was performed using a nanoElute ultrahigh-performance LC apparatus and a timsTOFPro mass spectrometer (Bruker Daltonics, Bremen, Germany). Each digested sample was injected into a spray needle column (ACQUITY UPLC BEH C18, 1.7 μm, Waters, Milford, MA, 75 μm i.d. × 250 mm) and separated by linear gradient elution with two mobile phases, A (0.1% formic acid in water) and B (0.1% formic acid in acetonitrile), at a flow rate of 280 μL/min. The composition of mobile phase B was increased from 2% to 35% in 100 min, changed from 35% to 80% in 10 min and kept at 80% for 10 min. The separated peptides were ionized at 1,600 V and analyzed by parallel accumulation serial fragmentation scan (Meier *et al.* 2018). Precursor ions were selected from the 12 most intense ions in a survey scan (precursor ion charge: 0–5, intensity threshold: 1,250, target intensity: 10,000).

De novo sequencing and database searches were performed with an error tolerance of 20 ppm for precursor ions and 0.05 Da for fragment ions using PEAKS X+ software (version 10.5) (Ma *et al.* 2003). The protein sequences generated from our draft genome dataset (Kono *et al.* 2019, 2021a) (GCA_013235015.1 for *A. ventricosus* and GCA_019973975.1 for *T. clavata*) were used as a reference database. The abundance of proteins identified from each sample was estimated using the intensity-based absolute quantification (iBAQ) method (Wiśniewski *et al.* 2014). The LC–MS

raw data and the associated files were then deposited in the ProteomeXchange Consortium (accession number: PXD038879) via the jPOST partner repository (accession number: JPST001957).

2.3 Results

2.3.1 Separate forcible silking of MA-silk and MI-silk

We collected MA-silk and MI-silk from *A. ventricosus* with separate forcible silking. The diameters of MA-silk and MI-silk observed with SEM were 3.40 ± 0.17 μm and 2.11 ± 0.10 μm, respectively (Figure 2-1B). The diameters were consistent with previous reports of forcibly silked MA-silk and MI-silk (Guinea *et al.* 2012). The stress-strain curves of MA-silk and MI-silk obtained by forcible silking from *A. ventricosus* were tested in air (Figure 2-1C). The mechanical properties of the stress-strain curves are summarized in the before immersion rows in Table 2-1. MA-silk has shown higher strength and lower extensibility than MI-silk. The Young's modulus of each silk was almost the same. The trend of mechanical properties of MA-silk and MI-silk is consistent with earlier reports of *Argiope* and *Trichonephila* (Blackledge and Hayashi 2006; Guinea *et al.* 2012).

2.3.2 Wide-angle X-ray scattering of MA-silk and MI-silk

Comparison of the nanostructure of MA-silk and MI-silk of *A. ventricosus* was conducted with synchrotron wide-angle X-ray scattering (WAXS). By subtracting the MI-silk scattering profile from MA-silk, the difference in crystalline state was characterized (Figure 2-3). MA-silk's crystallite size of the *a*-axis and *b*-axis was larger than MI-silk, and the sizes of the *c*-axis were similar for both. In a previous study, *T. clavipes* MI-silk was reported to be more crystalline and to have larger β-sheet crystallites than MA-silk (Sampath and Yarger 2015). The opposite sizes of MA-silk and MI-silk of *A. ventricosus* with *T. clavipes* might suggest that MI-silks of different species have different structural properties. Then, we observed how the crystal structures of MA-silk and MI-silk deformed while drawing fibers by performing WAXS while drawing (Figure 2-4). Compared to MA-silk crystallites, MI-silk crystallites were observed to be more prone to lattice deformation. The difference in lattice deformation propensity might be related to the difference in mechanical properties.

2.3.4 Mechanical properties of MA-silk and MI-silk of A. ventricosus before and after immersion in water

We tested the supercontraction of *A. ventricosus* MA-silk and MI-silk to compare the reaction to

water of each type of silk. To test supercontraction, we immersed silk samples in water and then

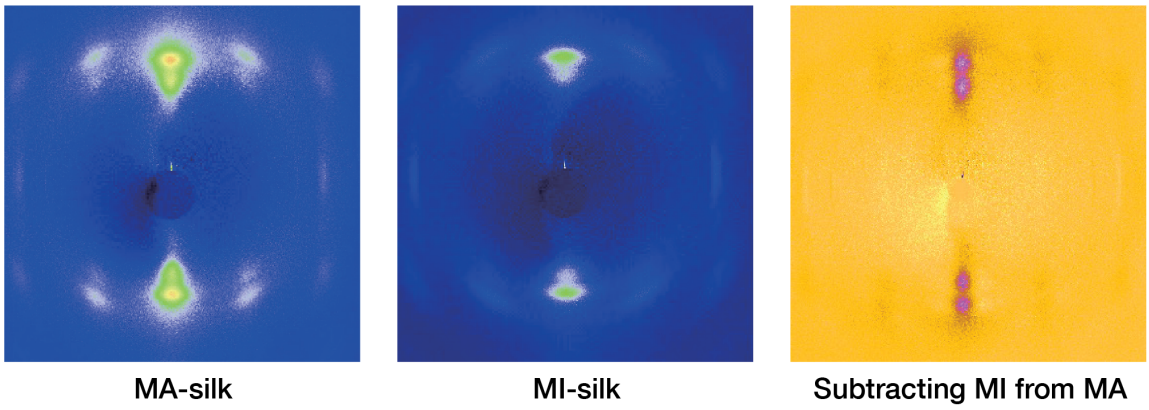

Figure 2-3 WAXS 2D profile of *A. ventricosus* MA-silk and MI-silk.
The rightmost WAXS 2D profile is the MI-silk profile subtracted from MA-silk.

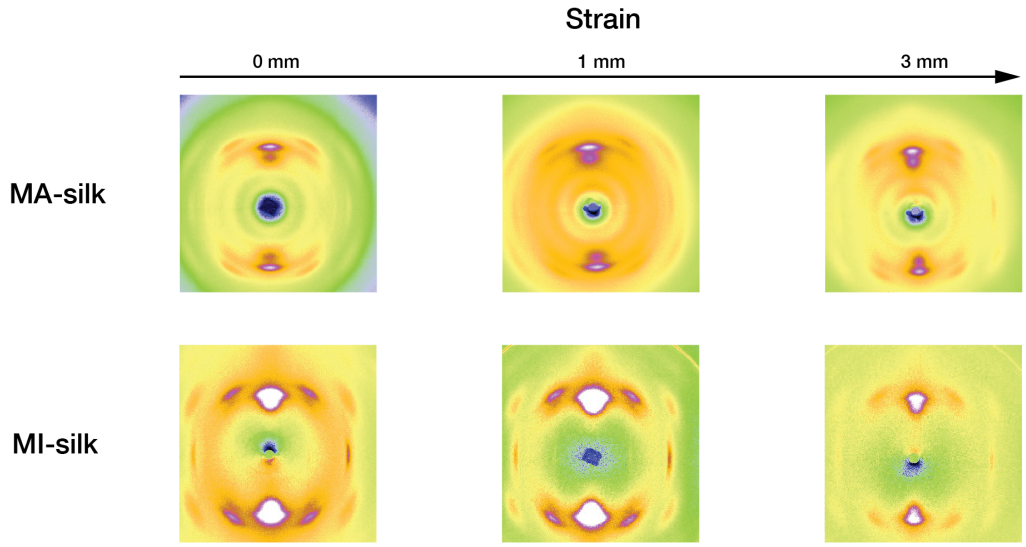

Figure 2-4. Structural analysis of *A. ventricosus* MA-silk and MI-silk upon extension.
The top and bottom rows are 2D WAXS profiles of MA-silk and MI-silk during stretching. The columns represent the strain added to the fibers.

measured length immediately. After complete drying (24 hours later), we measured the length of each sample again. The ratio of the length contracted per initial length was defined as the ratio of contraction. Table 2-2 summarizes the percentage of contraction after immersion in water and subsequent drying. As previous reports described (Work 1977; Guinea *et al.* 2012), MA-silk was more contracted than MI-silk. In accordance with previous reports, the total percentages of contraction of MA-silk and MI-silk of *A. ventricosus* were closer to *Araneus diadematus* (Work 1977) and *Argiope trifasciata* than *Trichonephila inaurata* (Guinea *et al.* 2012). *Trichonephila* MI-silk showed higher percentage of contraction than *Araneus* and *Argiope*. Then, we observed deformation of stress-strain curve by water immersion in MA-silk and MI-silk and reversibility thereof. We thus immersed *A. ventricosus* MA-silk and MI-silk into water and measured their mechanical properties after 2.5 hours, 7 hours, and 48 hours of immersion with tensile testing. As shown in Figure 2-5, supercontraction deformed the stress-strain curve of MA-silk after immersion in water, whereas the stress-strain curve of MI-silk after immersion in water showed relatively low deformation. This difference in the stress-strain curve before and after contraction has similar trends in the ratio of contraction summarized in Table 2-2. In both types of silks, there were clear yield point in stress-strain curve after water immersion which was not observed in the dried state. The diameter of the MA-silk clearly increased by supercontraction, but that of MI-silk remained unchanged. Although the supercontraction of MA-silk and MI-silk was evaluated 24 hours after water immersion, the mechanical properties were evaluated at 2.5 hours, 7 hours, and 48 hours. The mechanical properties of MA-silk and MI-silk after immersion in water do not change much, the contraction is likely to be finished after 2.5 hours of immersion in water. Therefore, the final length after supercontraction is assumed to be the percentage of contraction by water immersion shown in Table 2-2. However, if the mechanical properties of the contracted fibers are not changed during contraction, the percentage of contraction shown in Table 2-2 does not represent the final length after supercontraction. The mechanical properties tested are summarized in Table 2-1. Tensile strength and Young's modulus decreased in MA-silk just after water immersion, and again, changes were minimal in MI-silk. Similarly, the birefringence of MA-silk was reduced by approximately 63% after wetting, agreeing with previous observation of *A. diadematus* MA-silk (Work 1977), whereas that of MI-silk was reduced by only approximately 7%.

2.3.5 Proteome analysis of MA-silk and MI-silk from A. ventricosus and T. clavata

We analyzed the protein components of MA-silk and MI-silk reeled from *A. ventricosus* and *T. clavata* using nanoLC–MS/MS and the iBAQ method. From *A. ventricosus* MA-silk, we detected major and minor ampullate spidroins and candidates of spider silk-constituting elements (SpiCEs) (Figure 2-6). The detected spidroins were MaSp1, MaSp2, MaSp3, MaSp4 and MiSp (Figure 2-7, Figure 2-8, Figure 2-9, Figure 2-10, Figure 2-11, Figure 2-12). Although the protein abundance varied among the samples, the sum of the fractions of MaSp1 and MaSp2 was consistently greater

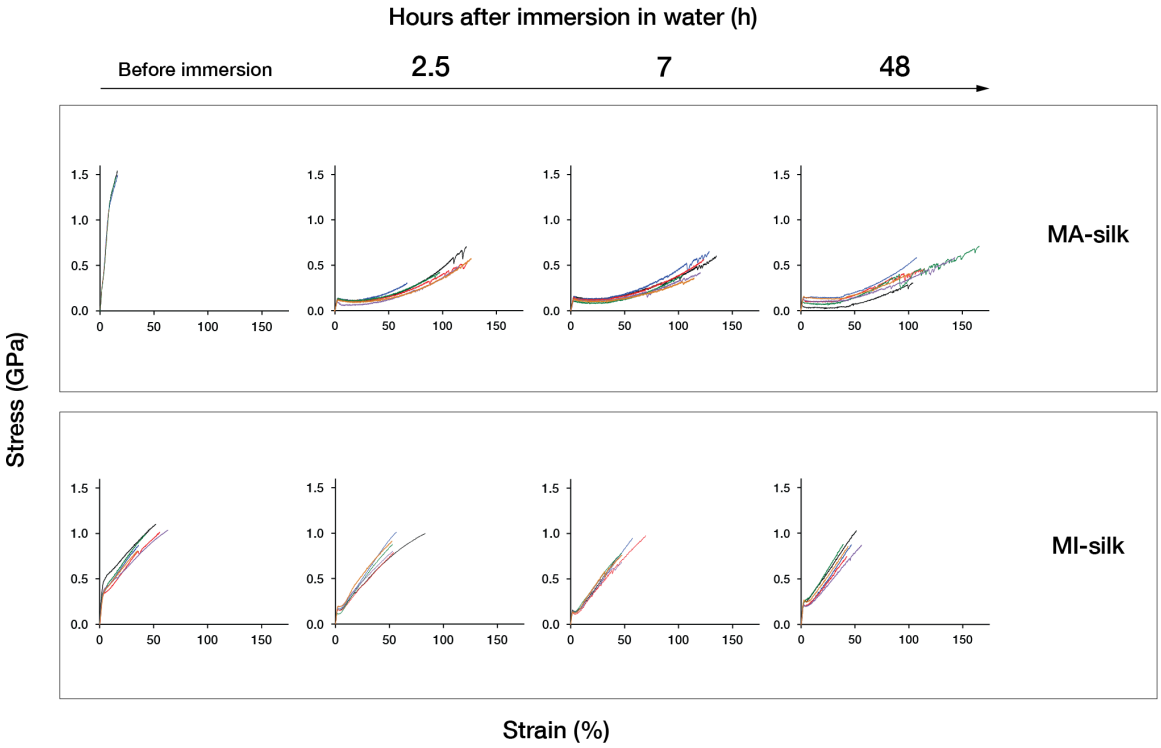

Figure 2-5. Stress-strain curves of *A. ventricosus* MA-silk and MI-silk before and after immersion and subsequent drying.

Colors indicate replicates. For each condition, N > 3.

Table 2-1. Mechanical properties, diameter, and birefringence of *A. ventricosus* MA-silk and MI-silk before immersion in water and subsequent drying.

	Hours after immersion in water (h)	Tensile strength (GPa)	Strain at break (%)	Young's modulus (GPa)	Toughness (MJ * m-3)	Diameter (μm)	Birefringence (*10-3)
MA-silk	Before immersion	1.406 ± 0.198	14.1 ± 3.9	13.62 ± 0.66	0.122 ± 0.052	3.40 ± 0.17	43.43 ± 2.92
	2.5	0.509 ± 0.137	108.6 ± 22.8	5.27 ± 1.08	0.239 ± 0.082	4.83 ± 0.30	-
	7	0.500 ± 0.124	121.1 ± 11.0	4.80 ± 1.38	0.277 ± 0.084	4.92 ± 0.23	-
	48	0.510 ± 0.145	122.9 ± 25.8	5.67 ± 1.03	0.294 ± 0.140	5.02 ± 0.26	16.11 ± 0.98
MI-silk	Before immersion	0.970 ± 0.110	53.8 ± 10.6	13.58 ± 2.05	0.328 ± 0.101	2.11 ± 0.10	46.26 ± 1.13
	2.5	0.898 ± 0.095	58.7 ± 12.1	8.86 ± 0.89	0.308 ± 0.098	2.45 ± 0.04	-
	7	0.812 ± 0.121	51.91 ± 9.9	8.38 ± 0.58	0.234 ± 0.074	2.11 ± 0.13	-
	48	0.879 ± 0.091	53.4 ± 9.3	11.44 ± 1.15	0.249 ± 0.057	2.14 ± 0.15	43.05 ± 1.50

Hours after immersion means the time after immersion in water. Values after ± are standard deviations. Minus signs mean no data.

Table 2-2. Percentage of contraction of *A. ventricosus* MA-silk and MI-silk.

	MA-silk	MI-silk
% contraction by immersion in water	51.2 ± 2.6	6.9 ± 1.7
% total contraction after drying	51.6 ± 2.5	6.9 ± 1.7

The % contraction by immersion in water is 100 × (initial length - contracted length measured immediately after immersion in water) / initial length. The total % contraction after drying is 100 × (initial length - contracted length after immersion in water and subsequent drying) / initial length. The values after ± are standard deviations.

than those of MaSp3 and MaSp4. MiSp was the smallest amount of spidroin for all samples (approximately 1%). Two genes of MaSp4 spidroin were detected from the proteome analysis, MaSp4A1.s1 (GBM28631.1) and MaSp4A1 (GBM28637.1) (Figure 2-11). From *A. ventricosus* MI-silk, we detected major and minor ampullate spidroins and SpiCE candidates. The main component of MI-silk was 5 MiSps, and it also contained MaSp1. SpiCE candidate g6858.t1 was detected from all MA-silk and MI-silk samples (Figure 2-13), suggesting that the expression of SpiCE is common among the major and minor ampullate silks, contributing also to the mechanical properties of MI-silk, as suggested by Kono *et al*. for MA-silk (Kono *et al.* 2021a). From *T. clavata* MA-silk, we detected MaSp1, MaSp2, MaSp3, SpiCEs, and SpiCE candidates, and from MI-silk, MaSp1, MiSp, and SpiCEs (Figure 2-14). Interestingly, the protein composition of MI-silk was strikingly different from that of *A. ventricosus*, where all samples contained a larger fraction of MaSp1 than MiSp. Similar to *A. ventricosus*, there were common SpiCEs contained both in MA-silk and MI-silk (Figure 2-15), of which SpiCE-NMa1 was previously shown to enhance the mechanical properties of MA-silk (Kono *et al.* 2021a).

2.3.6 Fibers of recombinant spidroins

To compare mechanical properties and how each protein reacts against water immersion, we created recombinant mini-spidroins of MaSp1, MaSp2, and MiSp and created artificial spider silks. Each construct consisted of an N-terminal 6×His tag, a linker (SSGSS), N-terminal domain (NTD), a truncated repeat region, and a C-terminal region, where the molecular weight was adjusted to approximately 50 kDa (Figure 2-2). Table 2-3 lists the molecular weights of the recombinant mini-spidroins. SDS-PAGE gel images for each recombinant mini-spidroins are shown in Figure 2-16. For all mini-spidroins, lyophilized protein powder was dissolved in DMSO and 2 M LiCl at a concentration of 15% (w/w) and was coagulated with MeOH during subsequent drawing in a water bath. Spinning conditions were set according to a previous report (Kono *et al.* 2021a). The maximum draw ratio was 6 x for MaSp1 and MiSp and 5.5 x for MaSp2. First, we compared the mechanical properties of artificial spider silks for each type of spidroin by tensile testing. Figure 2-17 shows stress-strain curves of 5 x drawing fiber for each recombinant mini-spidroin. Mechanical properties are shown in Table 2-3. MaSp1 had the highest tensile strength and the lowest strain at break. On the other hand, MaSp2 had the lowest tensile strength and the highest strain at break. Tensile strength and strain at break of MiSp was in between MaSp1 and MaSp2. Then, we tested the contraction of artificial spider silks by measuring the length before and after immersion in water by the same procedure with natural MA-silks and MI-silks. For 5 x drawing fiber (Figure 2-17), the ratio of contraction was 34.67 ± 1.15% for MaSp1, 41.33 ± 1.15% for MaSp2, and 29.33 ± 1.15% for MiSp after drying (Table 2-5). MaSp2 showed the largest contraction ratio, and MiSp showed the smallest contraction ratio. Although natural MI-silk showed approximately 7% contraction, MiSp fiber showed an approximately 4 times larger

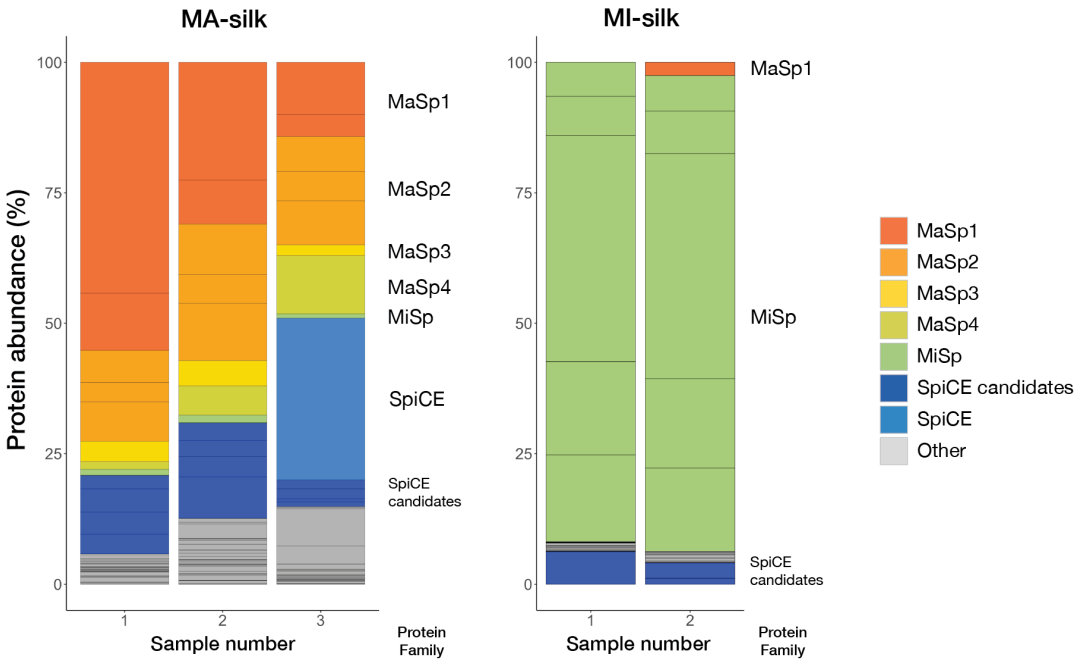

Figure 2-6. Protein abundance of *A. ventricosus* MA-silk and MI-silk

The bar chart shows the protein abundance for each protein in MA and MI silk analyzed by proteome analysis. The X-axis represents the silk samples spun from different individuals. The Y-axis is the ratio of protein abundance calculated by the iBAQ method (Wiśniewski *et al.* 2014). In the bar chart, each section represents individual proteins, and the colors of the sections represent protein families.

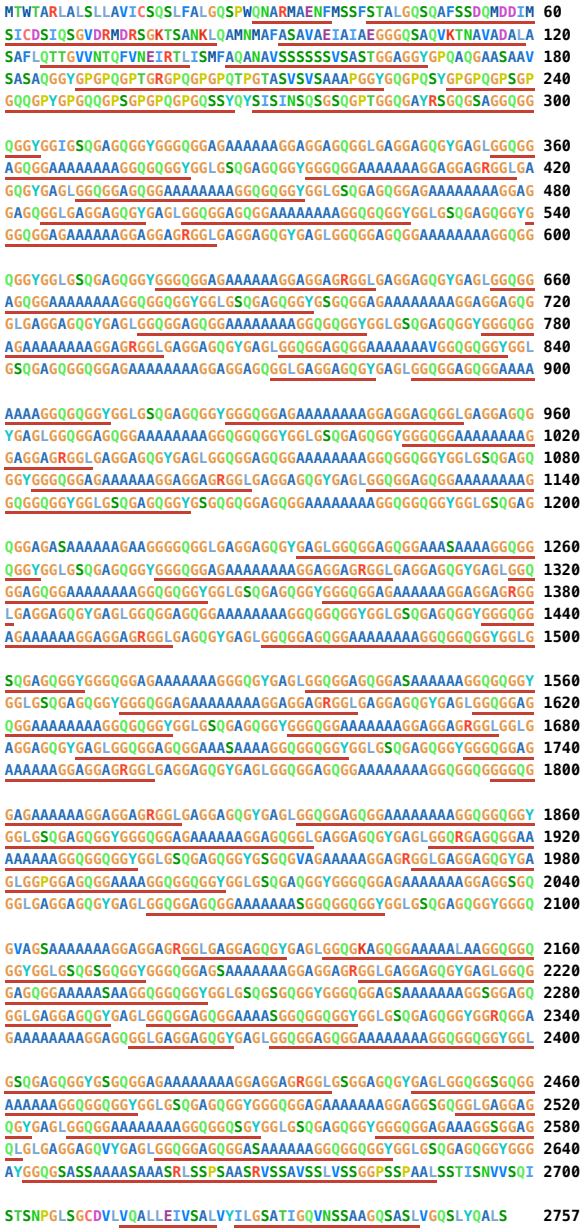

Figure 2-7. nanoLC–MS/MS peptide map of *A. ventricosus* MaSp1 (GenBank ID: GBM54680.1)
Peptides identified by LC-MS/MS from MA-silk were mapped onto the translated, full-length MaSp1 sequence curated from cDNA and genomic reads (Kono *et al.* 2019). The number in the right-most column next to each line denotes the position of the last residue in that row. Peptides detected in the proteomic analysis are underlined in red; when an identical peptide appears multiple times within the highly repetitive spidroin, every occurrence is underlined. Amino-acid coloring follows the Clustal X scheme (Larkin *et al.* 2007).

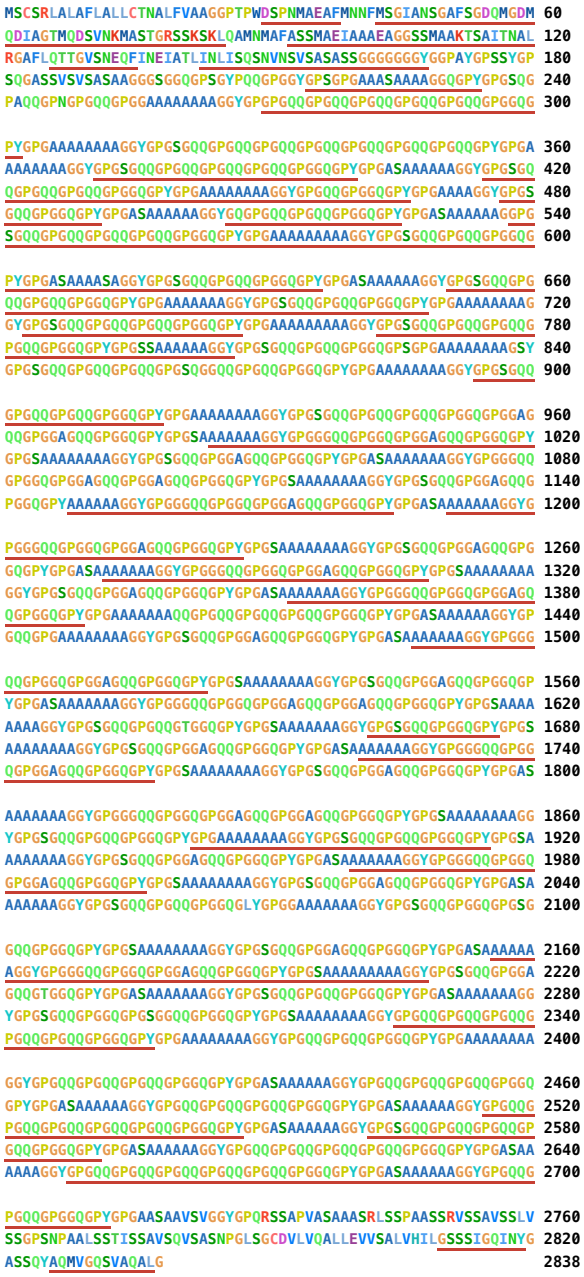

Figure 2-8. nanoLC–MS/MS peptide map of *A. ventricosus* MaSp2A (GenBank ID: GBN00527.1)
Peptides identified by LC-MS/MS from MA-silk were mapped onto the translated, full-length MaSp2A sequence curated from cDNA and genomic reads (Kono *et al.* 2019). The number in the right-most column next to each line denotes the position of the last residue in that row. Peptides detected in the proteomic analysis are underlined in red; when an identical peptide appears multiple times within the highly repetitive spidroin, every occurrence is underlined.

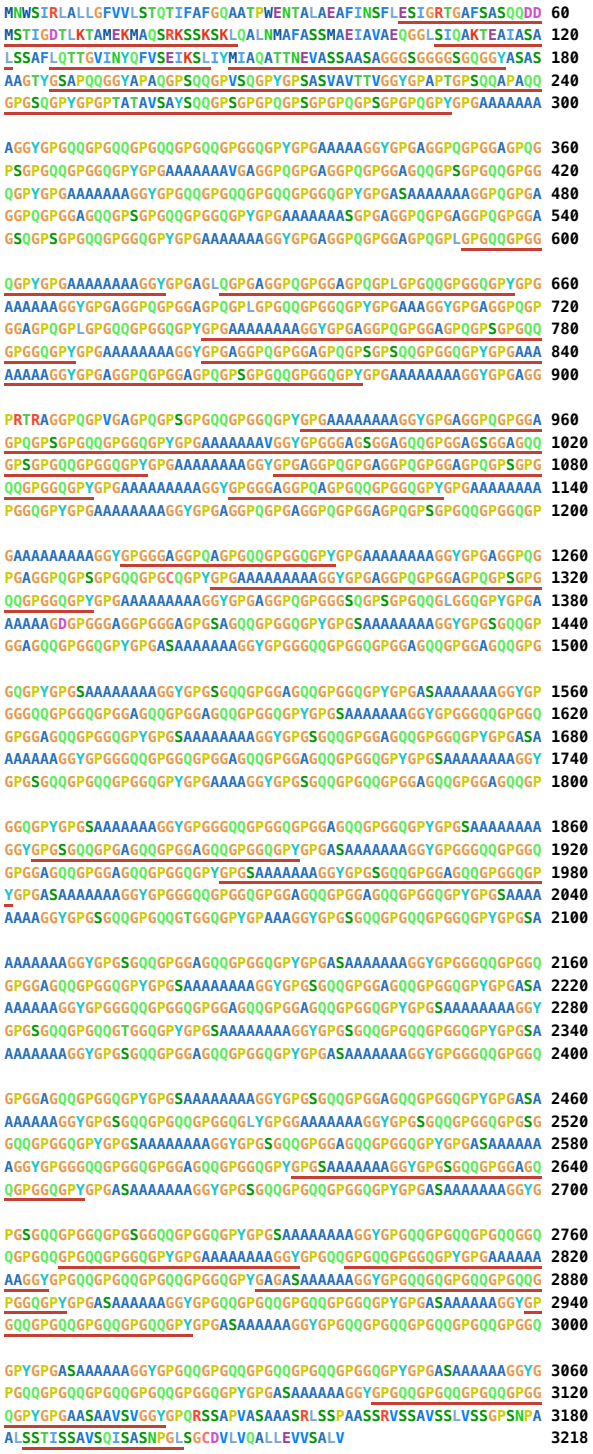

Figure 2-9. nanoLC–MS/MS peptide map of *A. ventricosus* MaSp2B (GenBank ID: GBN00528.1). Peptides identified by LC-MS/MS from MA-silk were mapped onto the translated full-length MaSp2B sequence, which was curated from cDNA and genomic reads (Kono *et al.* 2019). The number in the rightmost column next the sequence indicates position numbers. Peptides detected in the proteome are underlined in red; when a peptide occurs repeatedly within the highly repetitive spidroin, every instance is underlined.

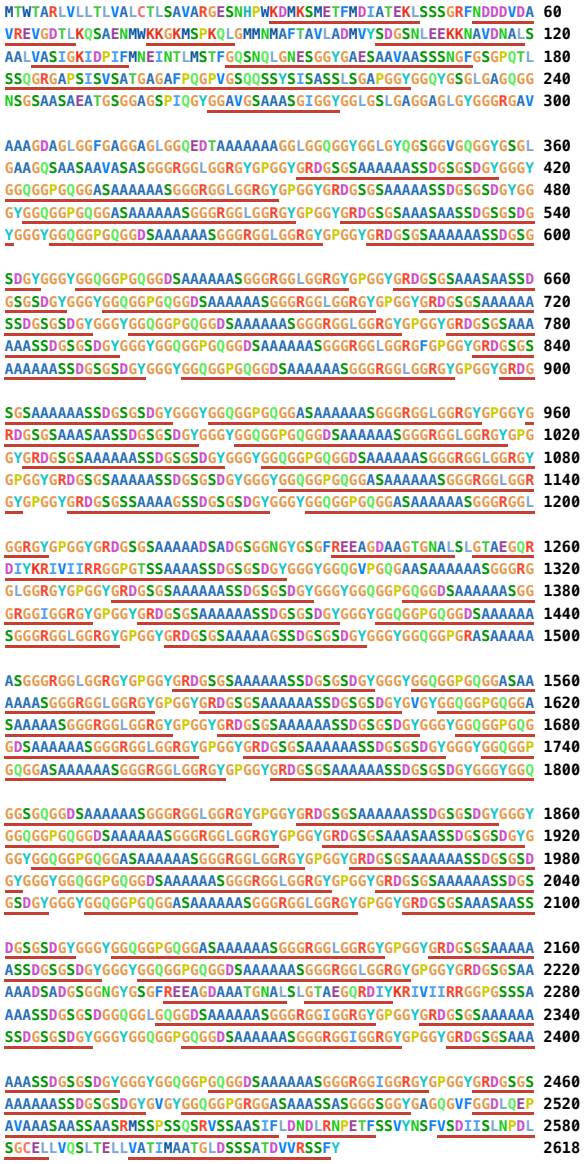

Figure 2-10. nanoLC–MS/MS peptide map of *A. ventricosus* MaSp3 (GenBank ID: GBN25680.1). Peptides identified by LC-MS/MS from MA-silk were mapped onto the translated full-length MaSp3 sequence, which was curated from cDNA and genomic reads (Kono *et al.* 2019). The number in the rightmost column next the sequence indicates position numbers. Amino-acid coloring follows the Clustal X scheme (Larkin *et al.* 2007).

Figure 2-11. nanoLC–MS/MS peptide map of *A. ventricosus* A) MaSp4A1.s1(GenBank ID: GBM28631.1) and B) MaSp4A1 (GenBank ID: GBM28637.1)

A) Peptides identified by nanoLC-MS/MS from MA-silk were mapped onto the translated MaSp4A1.s1 sequence, which was curated from cDNA and genomic reads (Kono *et al.* 2019). The number in the rightmost column next the sequence indicates position numbers. Peptides detected in the proteome are underlined in red; when a peptide occurs repeatedly within the highly repetitive spidroin, every instance is underlined. B) Peptides identified by nanoLC-MS/MS from MA-silk were mapped onto the translated MaSp4A1 sequence.

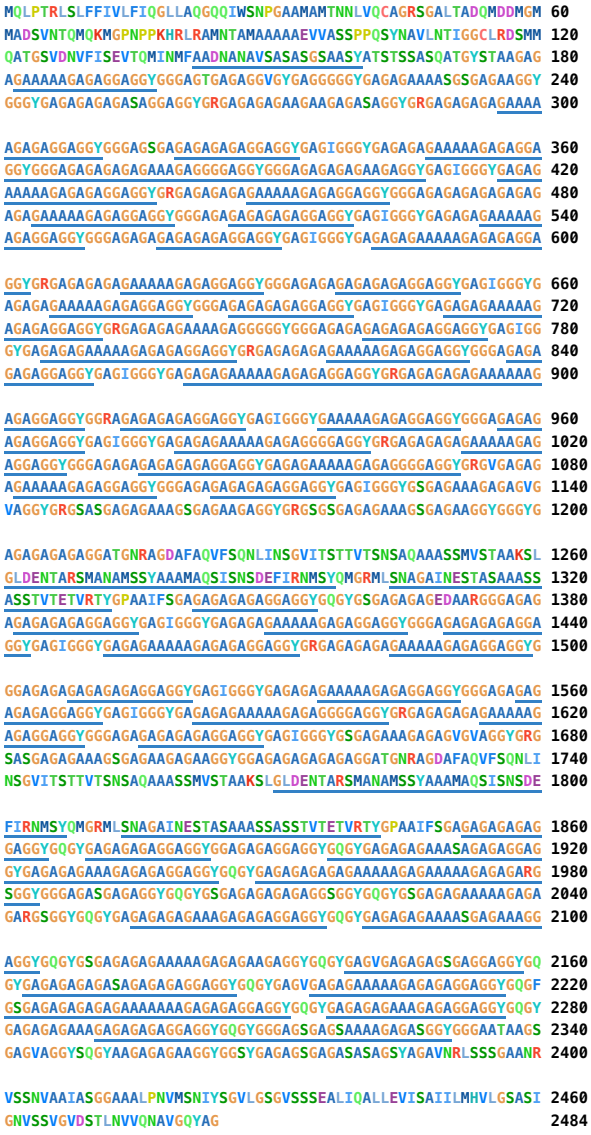

Figure 2-12. nanoLC–MS/MS peptide map of *A. ventricosus* MiSpB (GenBank ID: GBM96188.1). Peptides identified by nanoLC-MS/MS from MI-silk were mapped onto the translated MiSpB sequence, which was curated from cDNA and genomic reads (Kono *et al.* 2019). The number in the rightmost column next the sequence indicates position numbers. Peptides detected in the proteome are underlined in blue; when a peptide occurs repeatedly within the highly repetitive spidroin, every instance is underlined.

Figure 2-13. nanoLC–MS/MS peptide map of *A. ventricosus* SpiCE candidate g6858.t1(GenBank: GBM55674.1) detected in A) MA-silk and B) MI-silk.

A) Peptides identified by nanoLC-MS/MS from MA-silk were mapped onto the translated protein g6858.t1 sequence, which was curated from cDNA and genomic reads (Kono *et al.* 2019). The number in the rightmost column next the sequence indicates position numbers. Peptides detected in the proteome are underlined in red. B) Peptides identified by nanoLC-MS/MS from MI-silk were mapped onto the translated protein g6858.t1 sequence. Peptides detected in the proteome are underlined in blue.

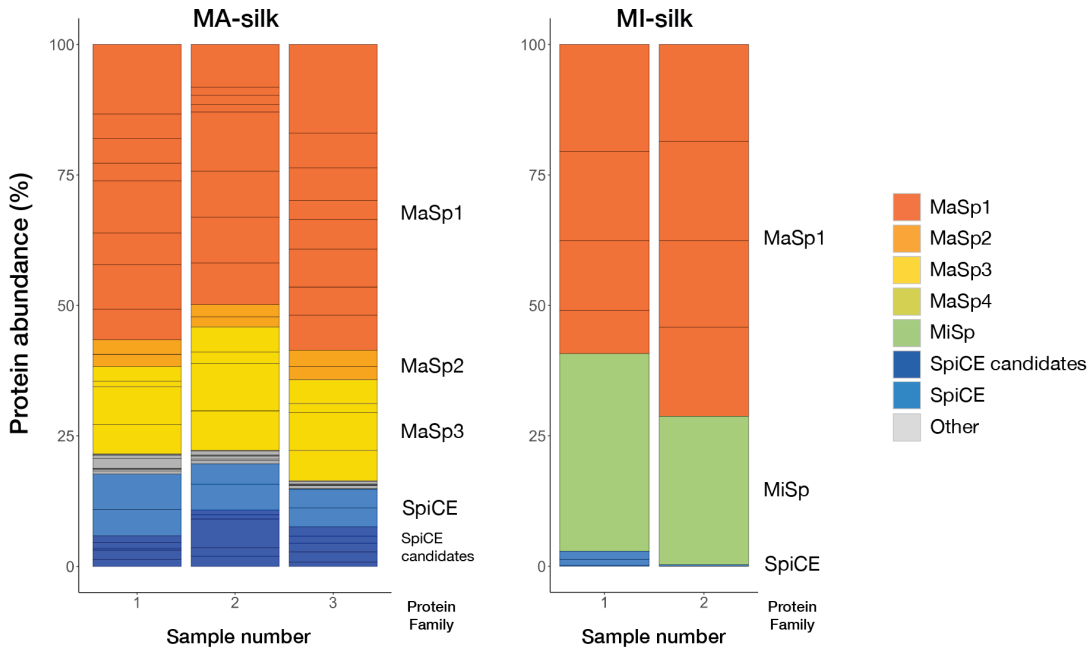

Figure 2-14. Protein abundance of *T. clavata* MA-silk and MI-silk.

The bar chart shows the protein abundance for each protein in MA- and MI-silk analyzed by proteome analysis. The X-axis represents the silk samples spun from different individuals. The Y-axis is the ratio of protein abundance calculated by the iBAQ method. In the bar chart, each section represents individual proteins, and the sections' colors represent protein families.

Figure 2-15. nanoLC–MS/MS peptide map of peptide mapping of *T. clavata* SpiCE-NMi1 (GenBank ID: GFQ84364.1).

Peptides identified by nanoLC-MS/MS from MI-silk were mapped onto the translated protein sequence. The number in the right-most column next to each line indicates the position of the last residue. Peptides detected in the proteomic analysis are underlined in blue.

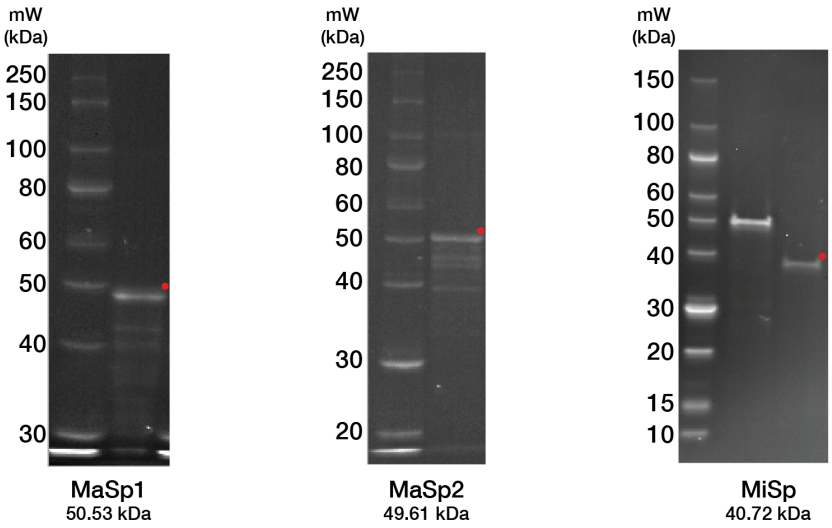

Figure 2-16. SDS-PAGE visualization of purified recombinant MaSp1, MaSp2, and MiSp mini-spidroins.

The gels were stained with InVision™ His-Tag In-Gel Stain (Thermo Fischer Scientific, MA, USA). Molecular weight markers are shown in the leftmost lane of each gel image. Mini-spidroins are indicated by the red dots.

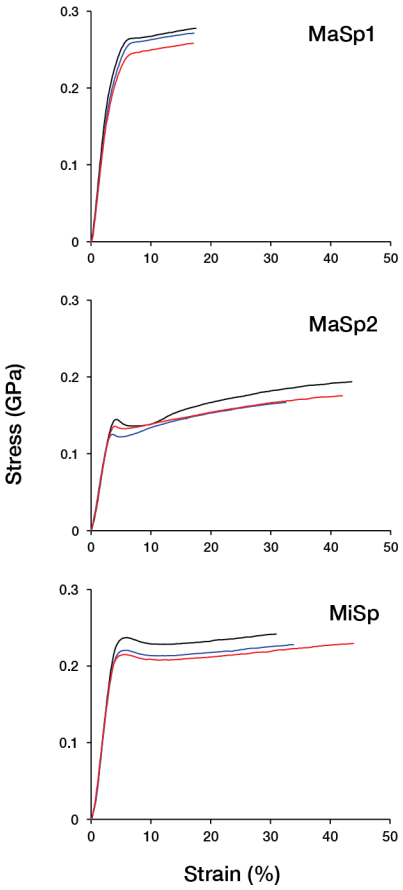

Figure 2-17. Stress-strain curve of artificial fibers of recombinant MaSp1, MaSp2, and MiSp before water immersion.

For all recombinant spidroins, three fiber test pieces from the same bobbin were used for tensile testing. The draw ratio of all artificial fibers was 5x. Colors indicate individual replicates.

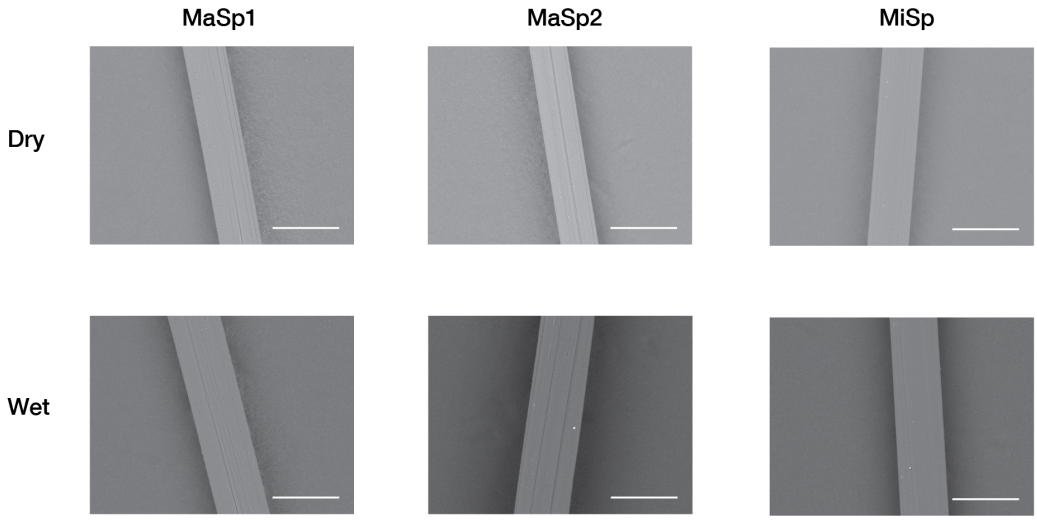

Figure 2-18. Morphology of artificial fiber of MaSp1, MaSp2, and MiSp, before (Dry) and after (Wet) water immersion.

The length of the scale bars in the images is 50 μm.

Table 2-3. Mechanical properties and diameter of recombinant mini-spidroin fibers before water immersion.

	Molecular weight (kDa)	Tensile strength (GPa)	Strain at break (%)	Young's modulus (GPa)	Toughness (MJ * m-3)	Diameter (μm)
MaSp1	50.53	0.269 ± 0.010	20.1 ± 0.4	6.68 ± 0.56	0.039 ± 0.002	33.89 ± 1.00
MaSp2	49.61	0.179 ± 0.014	42.1 ± 6.0	4.37 ± 0.13	0.060 ± 0.013	32.72 ± 1.63
MiSp	40.72	0.233 ± 0.008	39.4 ± 5.5	6.05 ± 0.18	0.076 ± 0.013	33.73 ± 1.10

For each recombinant spidroin, three fibers taken from the same bobbin were tested. Values are reported as mean ± s.d.

Table 2-4. Percentage of contraction for each recombinant mini-spidroins fibers.

	MaSp1	MaSp2	MiSp
% contraction by immersion in water	32.67 ± 3.06	39.33 ± 1.15	26.67 ± 1.15
% total contraction after drying	34.67 ± 1.15	41.33 ± 1.15	29.33 ± 1.15

As in Table 2-2, the % contraction by immersion in water is 100 × (initial length - contracted length measured immediately after immersion in water) / initial length. The total % contraction after drying is 100 × (initial length - contracted length after immersion in water and subsequent drying) / initial length. Values are shown as means ± s.d.

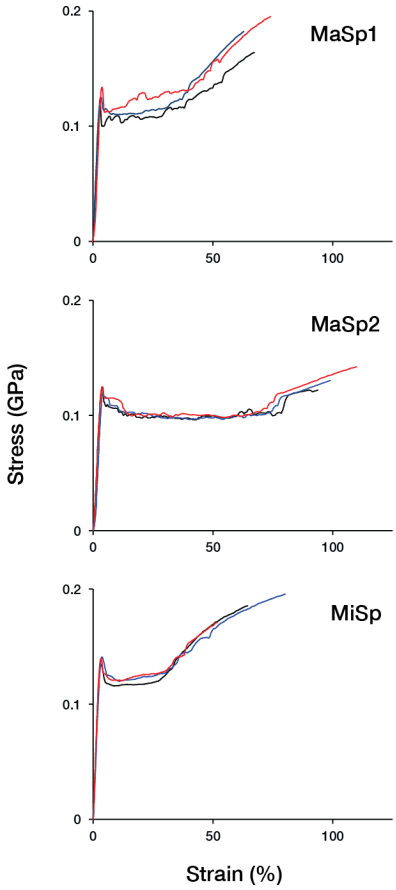

Figure 2-19. Stress-strain curve of artificial fibers of recombinant MaSp1, MaSp2, and MiSp after water immersion.

The draw ratio of all artificial fibers was 5x. Colors indicate individual replicates.

Table 2-5. Comparison of the percentage of contraction of MA-silk and MI-silk from spiders of the Araneidae family.

	Araneus ventricosus (This study)		*Araneus diadematus* (Work 1977)		*Trichonephila inaurata* (Guinea et al., 2012)		*Argiope trifasciata* (Guinea et al., 2012)	
	MA-silk N = 5	MI-silk N = 5	MA-silk N = 9	MI-silk N = 9	MA-silk	MI-silk	MA-silk	MI-silk
% contraction by immersion in water	51.2 ± 2.6	6.9 ± 1.7	53	4	24 ± 3	5.6 ± 0.3	51 ± 1	2.8 ± 0.7
% total contraction after drying	51.6 ± 2.5	6.9 ± 1.7	N.D.	N.D.	41 ± 1	13.4 ± 0.5	60 ± 2	5.3 ± 0.8

For this study, values are means ± s.d. Values from Guinea *et al*., 2012 shown as means ± s.e.m. Values from Work 1977 shown as means. N is the total number of fibers tested.

Table 2-6. Mechanical properties and diameter of recombinant mini-spidroin fibers after immersion in water and subsequent drying

	Tensile strength (GPa)	Strain at break (%)	Young's modulus (GPa)	Toughness (MJ * m-3)	Diameter (µm)
MaSp1	0.180 ± 0.016	70.9 ± 4.5	4.54 ± 0.42	0.089 ± 0.013	42.09 ± 1.65
MaSp2	0.132 ± 0.009	102.8 ± 8.1	3.75 ± 0.57	0.107 ± 0.013	40.03 ± 2.04
MiSp	0.184 ± 0.012	68.1 ± 12.8	5.02 ± 0.19	0.093 ± 0.026	38.25 ± 0.58

Values shown as means ± s.d. For all fibers, at least 3 fibers were tested.

contraction ratio than that. Additionally, while natural MA-silk showed approximately 50% contraction, the contraction ratios of MaSp2 fiber and MaSp1 fiber were lower than that. These differences between natural and artificial fibers were potentially due to differences in microstructural organization between natural and artificial silks, as contraction has been observed for regenerated silkworm silk fiber (Pérez-Rigueiro *et al.* 2019). Tensile testing was also performed for the artificial spider silk samples after water immersion (Figure 2-19 and Table 2-5). After water immersion and subsequent drying, the strain at break of fibers of all mini-spidroins was increased (Table 2-6). MaSp2 had the highest strain at break, and those of MaSp1 and MiSp were similar and approximately half of MaSp2 (Table 2-6). For tensile strength, MaSp2 was lower than MiSp and MaSp1. After water immersion, the stress-strain curves of MaSp1 and MiSp showed similar trends (Table 2-6).

2.4 Discussion

Spider dragline silks are often composed of MA-silk and MI-silk, but the simultaneous analysis of detailed molecular differences between the two remains relatively less explored. Here, we studied the mechanical properties (Figure 2-1), microstructural organization (Figure 2-3 and Figure 2-4), effects of water immersion and subsequent drying (Figure 2-5 and Table 2-1) and protein composition of MA-silk and MI-silk (Figure 2-6 and Figure 2-14) that were separately silked. The mechanical properties of separately silked MA-silk and MI-silk from *A. ventricosus* were in line with previous reports (Blackledge and Hayashi 2006; Guinea *et al.* 2012), confirming the successful separate silking of two types of silks (Table 2-7).

We then performed structural analysis by WAXS to observe nanostructural differences between MA-silk and MI-silk (Figure 2-3). The profile showed that both silks have semicrystalline structures, and the size of crystallites was different in silk types. With WAXS performed while drawing the fibers, we observed that MI-silk crystallites are more prone to deformation than MA-silk crystallites (Figure 2-4), supporting the aforementioned observation of irreversible changes in birefringence in MI-silk. The crystallites of MA-silk were larger than those of MI-silk on the *a*-axis and *b*-axis in *A. ventricosus*, which is different from the crystallite size comparison of *T. clavipes* MA-silk and MI-silk reported by Sampath *et al*., where MI-silk has been reported to have larger crystallites than MA-silk (Sampath and Yarger 2015) and suggests compositional differences between *Araneus* and *Trichonephila* MI-silks.

As previously reported, one of the most striking differences in the mechanical properties of these two fibers is their reaction to wetting (Work 1977; Guinea *et al.* 2012; Sampath and Yarger 2015). We obtained percentages of contraction of the MA-silk and MI-silk of *A. ventricosus* when immersed in water and with subsequent drying (Table 2-1). As expected, compared with the contraction ratio of *T. inaurata*, *A. trifasciata* and *A. diadematus* reported in previous studies, *A.*

Table 2-7. Comparison of the mechanical properties of MA-silk and MI-silk from spiders in the family Araneidae.

Organisms	Silk	Tensile strength (GPa)	Strain at break (%)	Young's modulus (GPa)	Toughness (GJ * m-3)	Source
Araneus ventricosus	MA-silk N = 4	1.406 ± 0.198	14.1 ± 3.9	13.6 ± 0.7	0.122 ± 0.052	This study
	MI-silk N = 6	0.970 ± 0.110	53.8 ± 10.6	13.58 ± 2.05	0.328 ± 0.101	
Trichonephila inaurata	MA-silk N = 6	1.8 ± 0.06	26 ± 1	14.2 ± 0.6	0.264 ± 0.005	(Guinea et al., 2012)
	MI-silk N = 6	1.5 ± 0.2	46 ± 5	11.2 ± 0.7	0.300 ± 0.50	
Argiope trifasciata	MA-silk N = 6	1.3 ± 0.2	17 ± 2	10.7 ± 0.3	0.090 ± 0.030	
	MI-silk N = 6	0.7 ± 0.1	45 ± 2	10.0 ± 0.4	0.240 ± 0.020	
Argiope argentata	MA-silk N = 135	1.495 ± 0.065	20.5 ± 0.5	8.0 ± 0.8	0.136 ± 0.007	(Brackledge and Hayashi, 2006)
	MI-silk N = 51	0.923 ± 0.154	33.0 ± 3.3	10.6 ± 1.2	0.137 ± 0.022	

For this study, values are means ± s.d. Other values are presented as means ± s.e.m. Significant digits are the same as references. N is the total number of fibers tested.

ventricosus MI-silk was more similar to those of *A. trifasciata* and *A. diadematus* (Table 2-5). The difference in the contraction ratio between *Araneus* and *Trichonephila*, likewise the difference in the size of crystallites observed in structural analysis, suggest compositional difference in these genera.

While the stress-strain curve of MA-silk was significantly deformed by water immersion and resulted in increased strain at break and decreased tensile strength and Young's modulus, MI-silk was less affected by water, as shown in Figure 2-5 and Table 2-1. On the other hand, an yield point in the stress-strain curve became observable after wetting both in MA-silk and MI-silk. This indicates the loss of orientation in the micro-organizational structure in MI-silk upon wetting, as observed in the birefringence measurements before and after immersion in water. The decrease in birefringence could be an explanation for this change, mirroring the reports of a similar loss of orientation of the amorphous component in *Trichonephila clavipes* and *Argiope aurantia* MI-silk before and after immersion in water using WAXS by Sampath and Yarger (2015).

Compositional analysis was thus conducted using proteome analysis of MA-silk and MI-silk of *A. ventricosus* and *T. clavata* (Figure 2-6 and Figure 2-14). MA-silk and MI-silk of both species were comprised of spidroins and minor components SpiCE, as previously reported (Kono *et al.* 2019, 2021a), and interestingly, both species showed the inclusion of common SpiCEs both in MA-silk and MI-silk, suggesting that the use and enhancement of mechanical properties by SpiCE is a conserved feature among the major and minor ampullate silks. In particular, SpiCE -NMa1, a SpiCE previously shown to double the tensile strength of artificial spider silk just by 1% (w/w) addition, was included both in MA-silk and MI-silk of *T. clavata*. The sequence similarity of common SpiCEs of *A. ventricosus* and *T. clavata* was low (16% identity), confirming the clade-specific adaptation expected in our previous report (Kono *et al.* 2019).

Notably, MI-silk was composed of MiSp and MaSp1 and not MaSp2. Moreover, the compositional ratio between MaSp1 and MiSp was strikingly different between *A. ventricosus* and *T. clavata*, where it was predominantly comprised of MiSp with little MaSp1 in *A. ventricosus* and a mix of these two with the excess of MaSp1 over MiSp in *T. clavata*. This reciprocal composition of MiSp and MaSp1 in the two species is in accordance with the reversed crystallite size among the two genera, and with the nanostructural organization in MA-silk, the larger crystallite size can therefore be attributed to MaSp1 being the major constituent.

Unlike many other Orbiculariae, *Trichonephila* is known for leaving auxiliary spirals on its orb web. Hasselberg and Vollrath studied the mechanical properties of auxiliary spirals in the orb web of *Trichonephila edulis* and concluded that it was highly unlikely that all scaffolding *T. edulis* silk was MI-silk (Hesselberg and Vollrath 2012). We argue that the MA-silk-like composition of *Trichonephila* MI-silk, with the major component being MaSp1 instead of MiSp, could explain this paradoxical use and mechanical property of MI-silk. The differing supercontraction behaviors

and protein compositions of MI-silk in *A. ventricosus* and *T. clavata* imply a role for MaSp1 in supercontraction. Previous study suggests MaSp1 contribution to the supercontraction (Guan, Vollrath and Porter 2011), however, further investigation is warranted.

The use of only MaSp1 among the MaSp paralogs in MI-silk both in *Araneus* and *Trichonephila* suggests that MaSp1 is the basic component for ampullate silks rather than MaSp2, MaSp3, and MaSp4, which is in good agreement with the suggestion that MaSp2 is relatively newly acquired at the base of Orbiculariae (Blackledge *et al.* 2009; Blamires, Blackledge and Tso 2017).

The proteomic compositional analysis suggests that the supercontraction and irreversible change in mechanical properties by water immersion of MA-silk can be attributed to the inclusion of MaSp2. The -GPG- motif shared in MaSp2, MaSp3 and MaSp4 is suggested to be the cause of supercontraction (Liu *et al.* 2008; Guan, Vollrath and Porter 2011), whereas the mirroring -GXG- motif of MaSp1 was linked to T_g-related contraction, as proposed by Guan *et al*. (Guan, Vollrath and Porter 2011). To better characterize this contribution of different spidroins, we produced artificial spider silk made individually from recombinant mini-spidroins of MiSp, MaSp1, and MaSp2. As expected, artificial MaSp2 fiber was the most affected by water immersion and the percentage of contraction was the highest in these three spidroins, again supporting the fact that MI-silk is predominantly composed of MiSp and MaSp1 and has fewer effects against water immersion (Table 2-4).

2.5 Conclusions

The difference in reaction to water immersion between MA-silk and MI-silk is an interesting model of silk component-structure–function relationships. Here, we analyzed the difference in supercontraction behavior in two types of ampullate silk prepared by separate forcible silking. As previously observed, we confirmed that MI-silk has a lower ratio of contraction and a lower level of mechanical property deformation than MA-silk. We then performed proteome analysis of MA-silk and MI-silk enabled by the silking method. The MI-silk constituents were revealed by MaSp1, MiSp, and SpiCE, and no MaSp2 was observed in their composition. Comparison of protein composition between *A. ventricosus* and *T. clavata* suggests that the difference in composition could explain the different ecological usage of MI-silk in the two species. Furthermore, we created artificial fibers from recombinant MaSp1, MaSp2 and MiSp mini-spidroins and tested supercontraction. The fact that MI-silk does not contain MaSp2 and recombinant MaSp2 has a higher contraction ratio than MaSp1 and MiSp suggests that the reason for the difference in supercontraction is the existence of MaSp2.

Chapter 3
Correlating mechanical properties and sequence motifs in artificial spider silk by targeted motif substitution

3.1 Introduction

Due to its remarkable mechanical properties, including toughness up to 0.45 GJ/m³ (Arakawa *et al.* 2022), and energy-efficient production (Malay *et al.* 2020), MA-silk has been extensively studied to understand how it achieves its superior mechanical properties and forms fibers from soluble spinning dopes (Humenik, Scheibel and Smith 2011; Porter, Guan and Vollrath 2013; Malay *et al.* 2022). Since natural spider silk is primarily composed of proteins, there have been ongoing efforts to artificially reconstruct fibers with similar attractive mechanical properties using recombinant protein technology (Koeppel and Holland 2017; Guo *et al.* 2020; Whittall *et al.* 2021). Furthermore, with the recent attention on marine microplastic pollution derived from synthetic polymers (Andrady 2011; Belzagui *et al.* 2019), biodegradable protein materials are highlighted as sustainable alternatives (Guessous *et al.* 2024). The increasing demand for environmentally sustainable materials has prompted a re-evaluation of natural and artificial protein fibers (European Commission *et al.* 2024). Several startup companies are currently working on scaling up the production of artificial spider silk and some have already launched their products in the market (Miserez, Yu and Mohammadi 2023; Guessous *et al.* 2024). At present, however, most commercial uses of artificial spider silk remain limited to the textile and cosmetics sectors(Guessous *et al.* 2024), and its relatively modest mechanical performance is thought to be a key obstacle to broader market adoption. Thus, predictive design and control of the physical properties of artificial spider silk are crucial for improving alternative materials.

Several associations have been reported between the amino acid sequences of major ampullate spidroins (MaSps), which comprise MA-silk, and their mechanical properties. Blackledge *et al.* observed that the evolutionary acquirement of MaSp2 enhanced toughness by increasing extensibility, while introducing the GGX motif at the base of Entelegynae improved strength and stiffness (Blackledge *et al.* 2012). A phylogenetic analysis by Craig et al. revealed that the serine composition of MaSps are negatively correlated with toughness, while glycine composition is positively correlated with tensile strength, followed by proline composition negatively correlating with Young's modulus (Craig *et al.* 2020). These findings suggest that the sequence and composition of MA-silks significantly affect the physical properties. In studies of artificial spider

silk, it has been demonstrated that modifying protein sequences can alter the physical properties of the material. The mechanical properties of the artificial spider silk created from MaSp1, MaSp2, and MiSp recombinant mini-spidroin showed significant differences: MaSp1 exhibited the highest tensile strength, while MaSp2 had the highest extensibility (Nakamura *et al.* 2023). Greco *et al*. demonstrated that substituting tyrosine with phenylalanine in NT2RepCT reduced the supercontraction of biomimetically spun artificial spider silk (Greco *et al.* 2021). In a recent study, Hu *et al*. investigated the effect of varying the length of poly-alanine in MaSp1-based mini-spidroin, finding that increasing poly-alanine length enhances tensile strength and Young's modulus (Hu *et al.* 2024). These observations suggest that protein sequences can indeed affect the physical properties of artificial spider silk fibers.

To elucidate the comprehensive relationship between protein sequence and physical properties in natural MA-silk, Arakawa *et al*. collected 1,000 spiders from diverse geographical locations and used transcriptomics to sequence the spidroins (Arakawa *et al.* 2022). Additionally, the physical properties of the dragline silk of these spiders were quantified. The study revealed that the third type of MA-silk spidroin, MaSp3, exhibited the strongest correlation with toughness. MaSp3 was initially identified through target capture sequencing in multiple spider species (Collin *et al.* 2018), and whole genome sequencing and multi-omics studies have demonstrated that MaSp3 is one of the most abundant spidroin in the MA-silk of Araneidae species (Kono *et al.* 2019, 2021a; Watanabe and Arakawa 2023). In the 1,000 spider silkome project, it was found that the composition of MaSp1, MaSp2, and MaSp3 primarily affects the physical properties of the silk; however, sequence motifs for each spidroin were also found to have correlations with various physical properties (Arakawa *et al.* 2022). In order to validate these correlations between sequence motifs and mechanical properties, recombinant mini-spidroins with and without these motifs should be spun into artificial spider silk, and the resulting physical properties of the silk should be evaluated.

Consistency in the expression of the recombinant host and the purification process is crucial for ensuring reliable results when comparing various recombinant protein fibers, as the variations in these factors can introduce additional variables that affect the physical properties of the fibers. Among the spidroin subtypes, MaSp2 is currently the most suitable for recombinant expression and purification due to its high expression levels and consistent behavior during purification. To this end, we employed recombinant techniques to create MaSp2-based mini-spidroin mutants, spinning them to test the effects of motifs extracted from the Spider Silkome Database on the physical properties of natural MA-silk (Arakawa *et al.* 2022)

3.2 Experimental section

3.2.1 Artificial spidroin design by motif substitution

Recombinant mini-spidroins used in this work were all based on BP1, an artificial mini-spidroin based on the major ampullate spidroin MaSp2 as previously described (Tachibana *et al.* 2021). The spidroin motifs utilized for the modification of BP1 mini-spidroin were extracted using the following procedure. First, the protein sequences of the MaSp2 that were sequenced from the individuals collected in Japan and the corresponding physical properties were extracted from the Spider Silkome Database. All samples with silk mechanical properties for spiders caught in Japan (271 out 446, 60.8%) were used, which is the majority of the samples. The list of individuals is accessible via the following URL; https://spider-silkome.org/individuals?loc=Japan. Then, we extracted motifs from the sequences by calculating the Pearson correlation between the occurrence values of the motifs, as previously described (Arakawa *et al.* 2022). Finally, we selected the motifs to be tested in vitro, which are those with the highest positive or negative correlation with mechanical properties, crystallinity, birefringence, and supercontraction. The SQ motif and PQ motifs were additionally selected because these motifs serve as alternatives of the QQ in MaSp2 in several Orbiculariae species which suggests relationships with mechanical properties (Arguelles *et al.* 2023). Subsequently, we defined substitution patterns for each motif, such as PGQ→GPQ, where the pattern means substituting PGQ in the BP1 amino acid sequence with GPQ. To ascertain the influence of specific motifs on the physical properties of BP1 silk, two modifications were made to the amino acid sequences. If BP1 already contained the motif of interest, the frequency of the motif was reduced by substituting it with a different sequence, while maintaining the overall amino acid composition. Conversely, if BP1 lacked the desired motif, the motif was introduced by adding or replacing sequences. Table 3-1 shows all BP1 mutants used in this study. The amino acid sequences of these BP1 mutants are detailed in Figures 3-1 to 3-15.

3.2.2 Recombinant protein expression and purification

The modified BP1 spidroin recombinant proteins were expressed and purified according to previously described methods (Kono *et al.* 2021a; Nakamura *et al.* 2023). The designed amino acid sequences of the spidroins were converted to nucleotide sequences using codon usage optimization for *Escherichia coli*. Oligonucleotide fragments were synthesized by Fasmac Co. (Kanagawa, Japan) and assembled using the overlap extension PCR method (Bryksin and Matsumura 2010). The plasmids were inserted into pET-22b (+) and then transformed into *E. coli* BLR (DE3). Cells were cultured in a 10-L jar fermenter (Takasugi Seisakusho Co. Ltd.) under previously described conditions. Protein expression was induced by the addition of 0.1 mM isopropyl-β-D-thiogalactoside (IPTG) after 24 hours of fermentation. After 24 hours of induction, the cells were centrifuged and purified according to previous reports. Proteins were purified, lyophilized, and stored in shaded dry boxes at 25°C for the following spinning experiments.

Table 3-1 Name, substitution pattern, and motif information for BP1 mutants.

Mutant name	Substitution pattern	Motif		
		Motif sequence	Property	Positive effect / Negative effect
BP1-TS-P	AAAAAAGP → AAAAASGP AAAAAGQ → AAAAASGPQ	AAAAASGP	Tensile strength	Positive
BP1-TS_YM_BR-N	GPGQQ → GPQGPQ	GPQ	Tensile strength, Young's modulus, Birefringence	Negative
BP1-TS_YM_BR-N2	PGQ → GPQ SSA → SAS	GPQ	Tensile strength, Young's modulus, Birefringence	Negative
BP1-TS_YM_BR-N3	GQ → QG GPQ → GPA	GPQ	Tensile strength, Young's modulus, Birefringence	Negative
BP1-TS_YM_N	QQ → PQ	PQ	Tensile strength, Young's modulus	Negative
BP1-YM-P	GPG → GPA	PA	Young's modulus	Positive
BP1-SB-P	QGPY → QGPSGY	QGPSG	Strain at break	Positive
BP1-SB-N	AAAAA → AAASA	AAASA	Strain at break	Negative
BP1-TN-P	GPGA → GPAG	PA	Toughness	Positive
BP1-TN-N	GPGQQGP → GPGSQGP	GPGSQGP	Toughness	Negative
BP1-CR-P	GPG → GPAG	GPA	Crystallinity	Positive
BP1-CR-N	GQ → QG	GQ	Crystallinity	Negative
BP1-CR-N2	QQ → SQ	SQ	Crystallinity	Negative
BP1-BR-P	SAA → SSA	SSA	Birefringence	Positive
BP1-SC-P	GPGQ → GPGAQ	GPGA	Supercontraction	Positive
BP1-SC-N	GPGA → GPAG YGP → YGPS	YGPS	Supercontraction	Negative

All BP1 mutants examined in this study are listed. Mutant names follow the format **BP1-{property abbreviation(s)}-{P or N}{index}**, where **P** and **N** denote a positive or negative effect, respectively. Property abbreviations are: tensile strength, **TS**; Young's modulus, **YM**; strain at break, **SB**; toughness, **TN**; crystallinity, **CR**; birefringence, **BR**; and supercontraction, **SC**. When more than one mutant targeted the same motif with the same effect direction, a sequential number was appended to differentiate them.

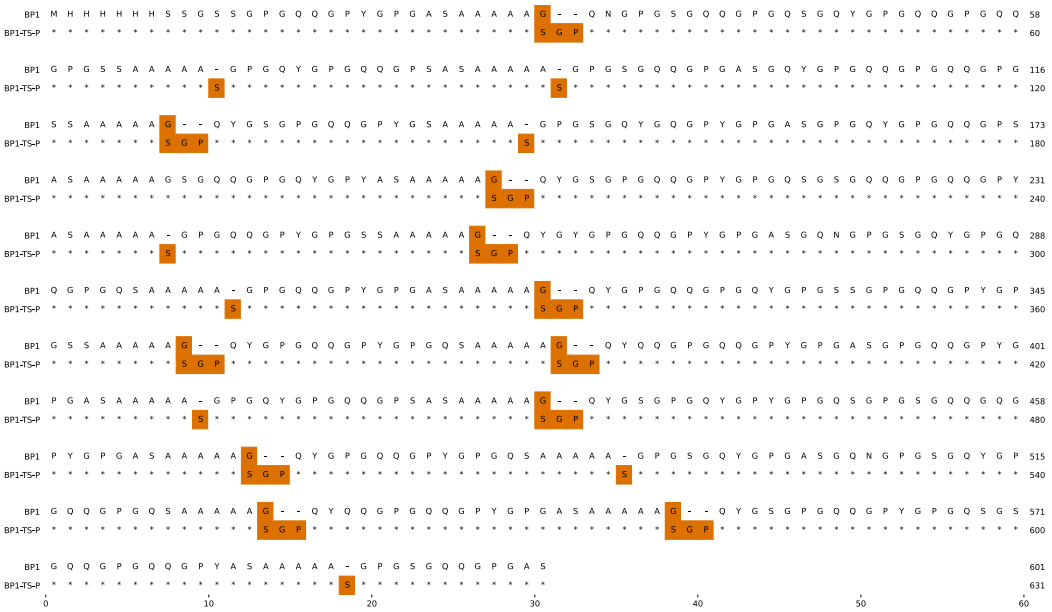

Figure 3-1. Amino acid sequence alignment of the protein BP1 and the tensile strength positive mutant BP1-TS-P.

The left-hand labels identify the reference sequence BP1 and the mutant BP1-TS-P. In the BP1-TS-P line, an asterisk (*) marks residues identical to BP1, and orange shading highlights substituted residues. A dash (–) denotes a gap. The rightmost numbers indicate position number for each sequence. BP1-TS-P is a mutant of BP1 carries the tensile strength positive motif AAAAASGP, which replaces the corresponding segment in BP1.Sequence alignment was done by MUSCLE version 3.8.1551 (Edgar 2004).

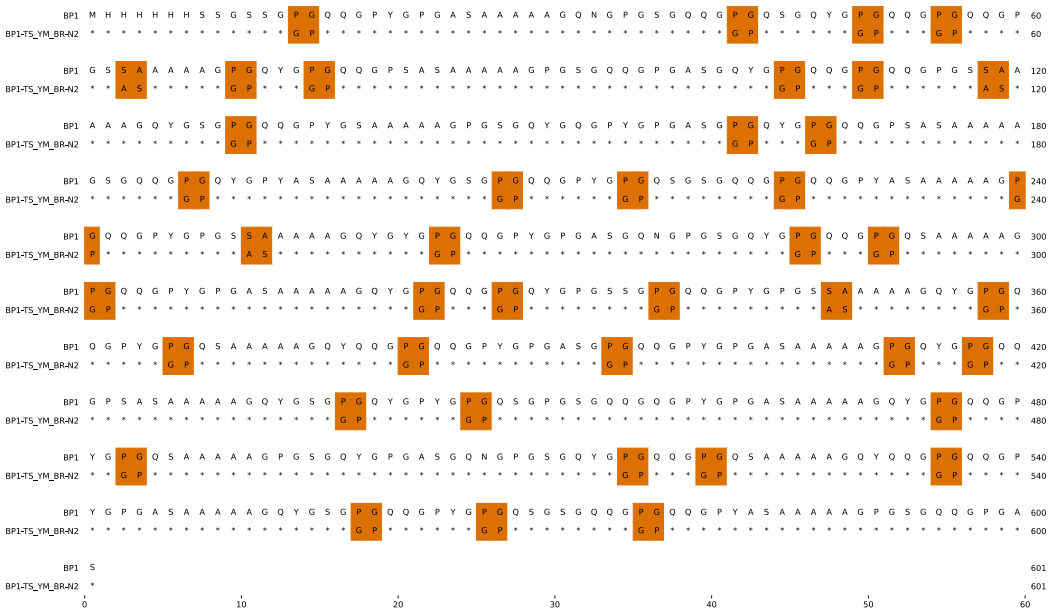

Figure 3-2. Amino acid sequence alignment of the protein BP1 and the tensile strength, Young's modulus and birefringence negative mutant BP1-TS_YM_BR-N2.

The left-hand labels identify the reference sequence BP1 and the mutant BP1-TS_YM_BR-N2. In the BP1-TS_YM_BR-N2 line, an asterisk (*) marks residues identical to BP1, and orange shading highlights substituted residues. A dash (–) denotes a gap. The rightmost numbers indicate position number for each sequence. BP1-TS_YM_BR-N2 is a mutant of BP1 to study the effect of the tensile strength, Young's modulus and birefringence negative motif GPQ. It carries GPQ and reduces birefringence positive motif SSA.

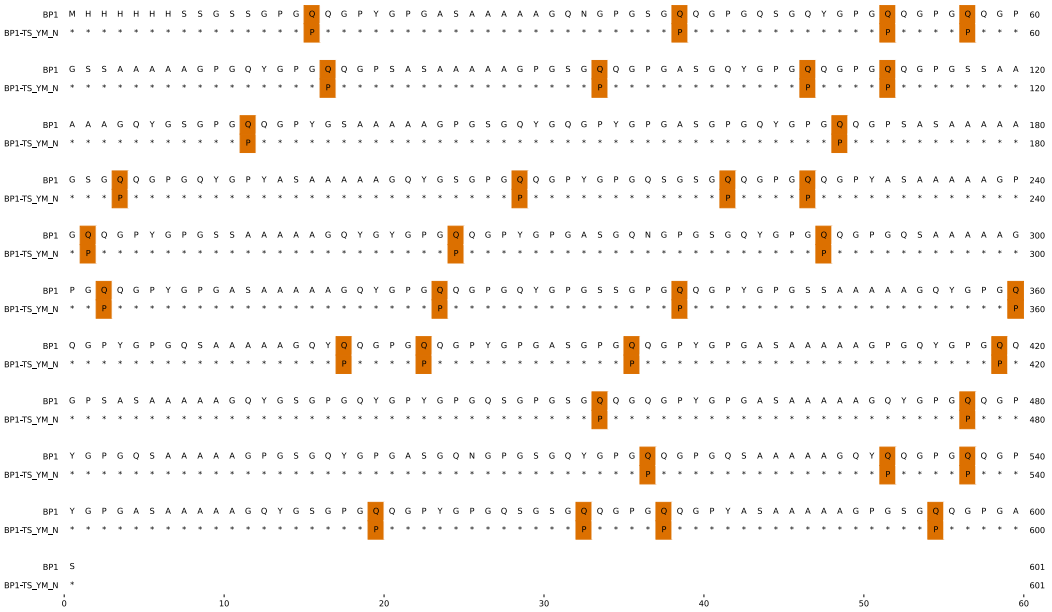

Figure 3-3. Amino acid sequence alignment of the protein BP1 and the tensile strength, Young's modulus negative mutant BP1-TS_YM_N.

The left-hand labels identify the reference sequence BP1 and the mutant BP1-TS_YM_N. In the BP1-TS_YM_N line, an asterisk (*) marks residues identical to BP1, and orange shading highlights substituted residues. A dash (–) denotes a gap. The rightmost numbers indicate position number for each sequence. BP1-TS_YM_N is a mutant of BP1 carries the tensile strength, Young's modulus negative motif PQ.

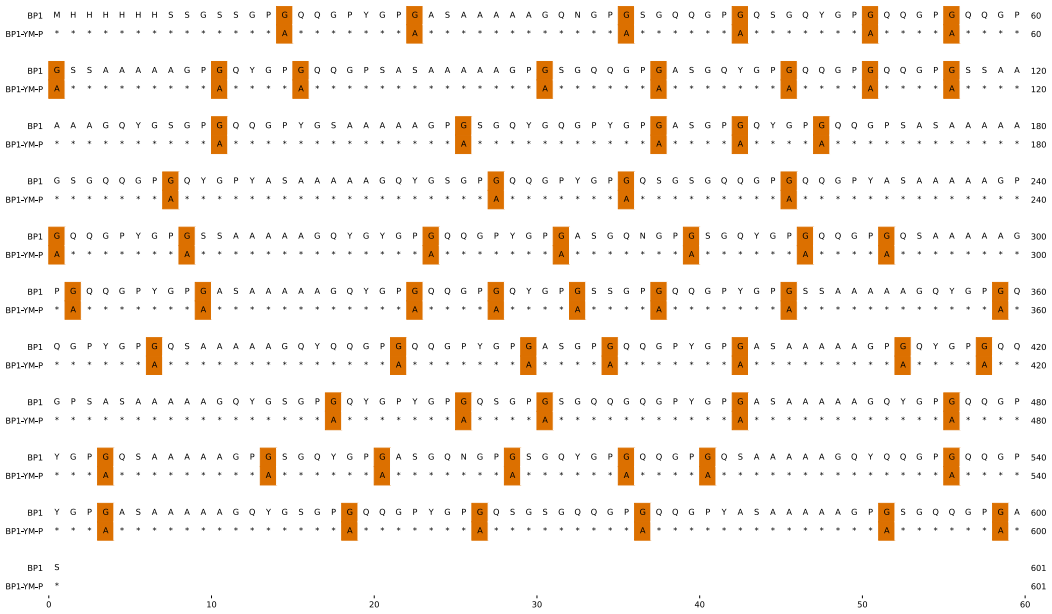

Figure 3-4. Amino acid sequence alignment of the protein BP1 and the Young's modulus positive mutant BP1-YM-P.

The left-hand labels identify the reference sequence BP1 and the mutant BP1-YM-P. In the BP1-YM-P line, an asterisk (*) marks residues identical to BP1, and orange shading highlights substituted residues. The rightmost numbers indicate position number for each sequence. BP1-YM-P is a mutant of BP1 carries the Young's modulus positive motif GPA.

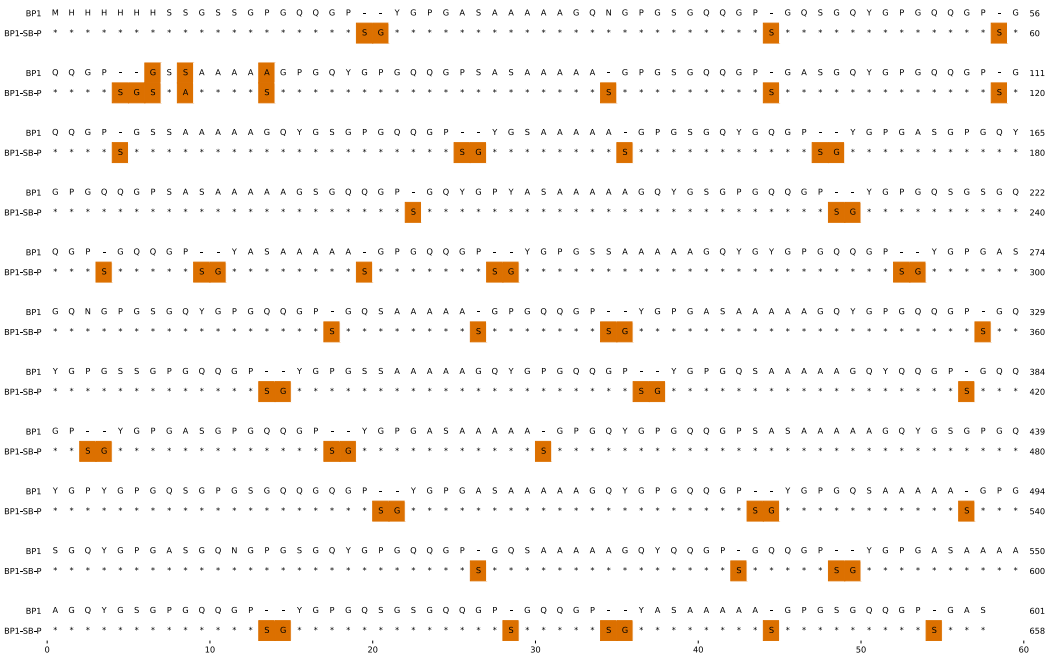

Figure 3-5. Amino acid sequence alignment of the protein BP1 and the strain at break positive mutant BP1-SB-P.

The left-hand labels identify the reference sequence BP1 and the mutant BP1-SB-P. In the BP1-SB-P line, an asterisk (*) marks residues identical to BP1, and orange shading highlights substituted residues. The rightmost numbers indicate position number for each sequence. BP1-SB-P is a mutant of BP1 carries the strain at the break positive motif QGPSG.

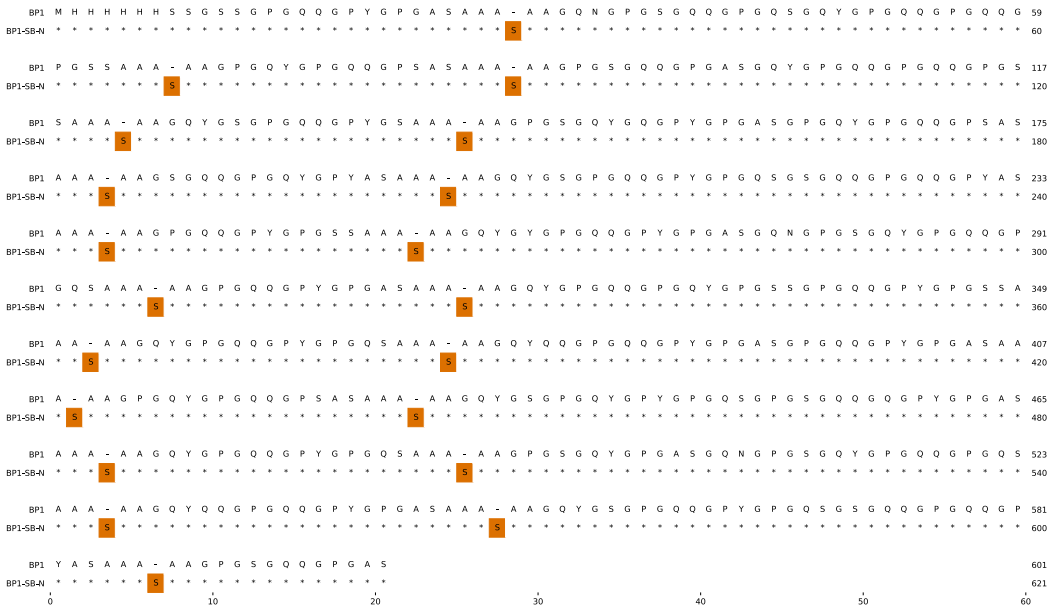

Figure 3-6. Amino acid sequence alignment of the protein BP1 and the strain at break negative mutant BP1-SB-N.

The left-hand labels identify the reference sequence BP1 and the mutant BP1-SB-N. In the BP1-SB-N line, an asterisk (*) marks residues identical to BP1, and orange shading highlights substituted residues. The rightmost numbers indicate position number for each sequence. BP1-SB-N is a mutant of BP1 carries the strain at the break negative motif AAASA.

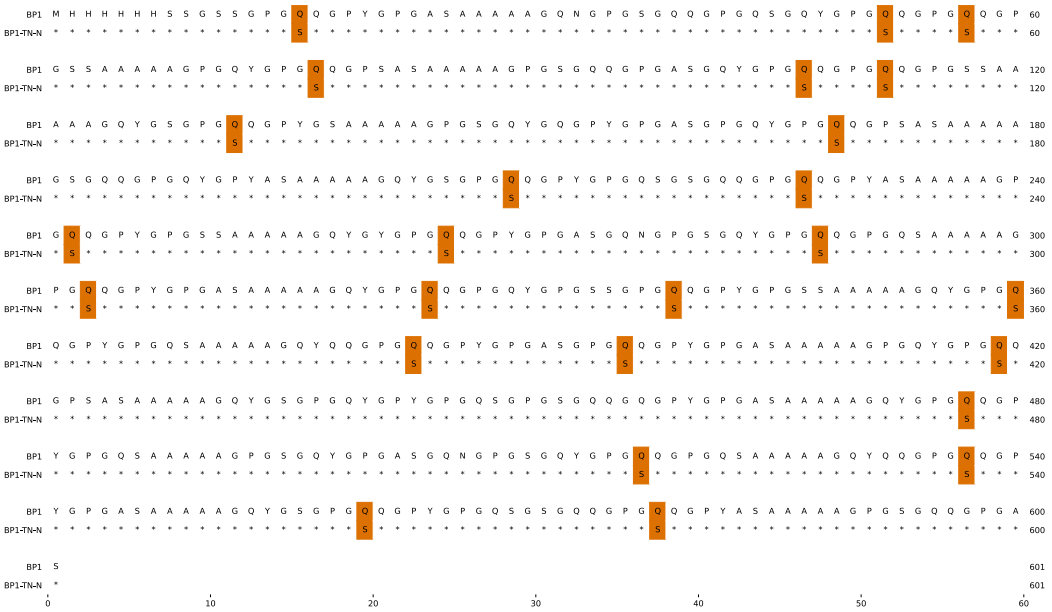

Figure 3-7. Amino acid sequence alignment of the protein BP1 and the toughness negative mutant BP1-TN-N.

The left-hand labels identify the reference sequence BP1 and the mutant BP1-TN-N. In the BP1-TN-N line, an asterisk (*) marks residues identical to BP1, and orange shading highlights substituted residues. The rightmost numbers indicate position number for each sequence. BP1-TN-N is a mutant of BP1 carries the toughness negative motif GPGSQGP.

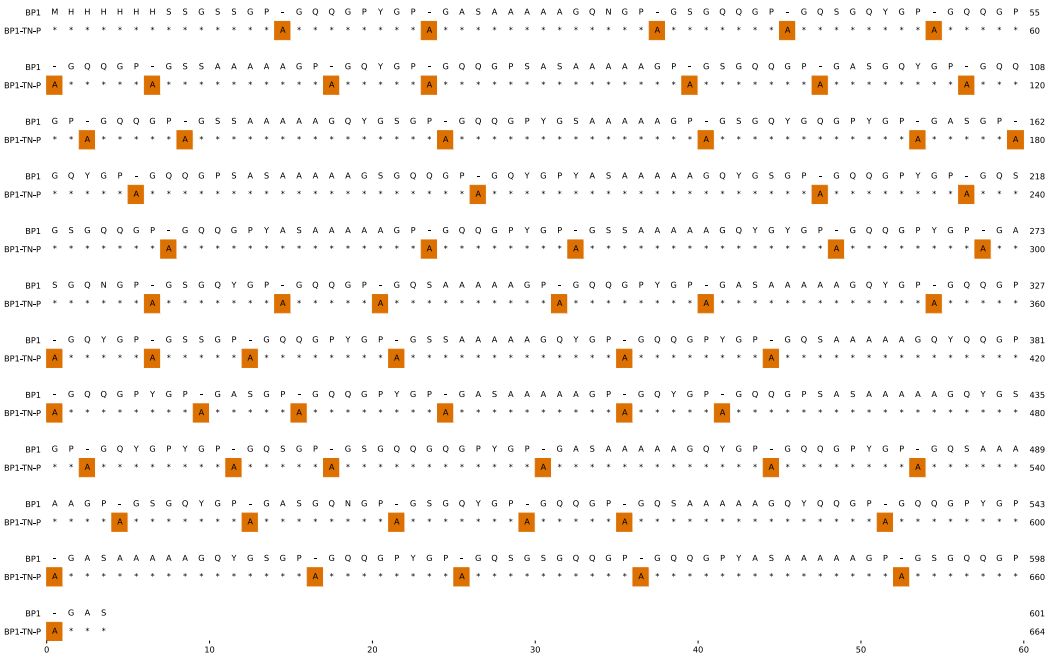

Figure 3-8. Amino acid sequence alignment of the protein BP1 and the toughness positive mutant BP1-TN-P.

The left-hand labels identify the reference sequence BP1 and the mutant BP1-TN-P. In the BP1-TN-P line, an asterisk (*) marks residues identical to BP1, and orange shading highlights substituted residues. The rightmost numbers indicate position number for each sequence. BP1-TN-P is a mutant of BP1 carries the toughness positive motif GPA.

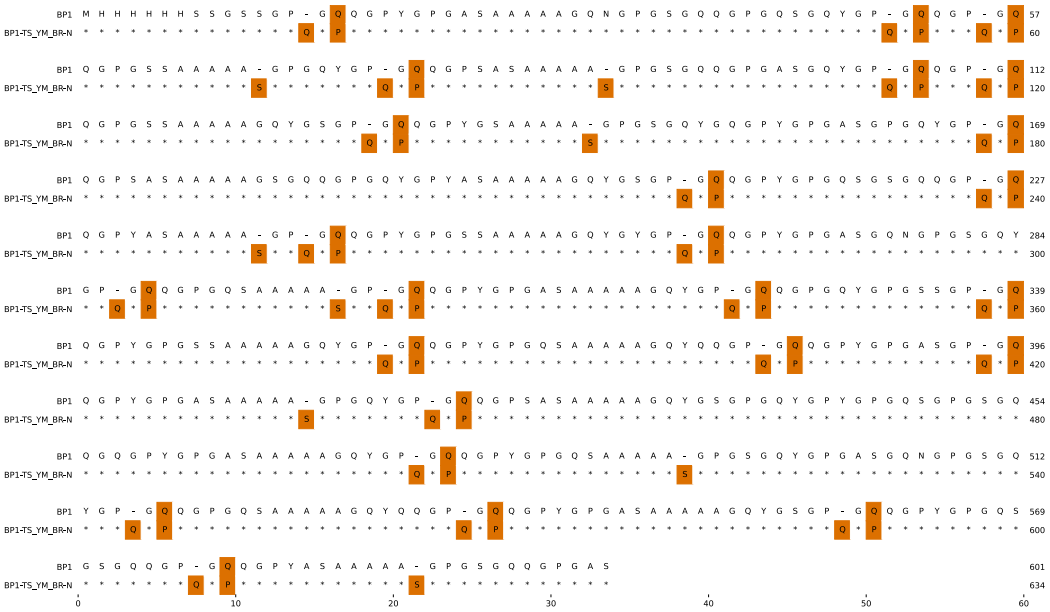

Figure 3-9. Amino acid sequence alignment of the protein BP1 and the tensile strength, Young's modulus, and birefringence negative mutant BP1-TS_YM_BR-N.

The left-hand labels identify the reference sequence BP1 and the mutant BP1-TS_YM_BR-N. In the BP1-TS_YM_BR-N line, an asterisk (*) marks residues identical to BP1, and orange shading highlights substituted residues. The rightmost numbers indicate position number for each sequence. BP1-TS_YM_BR-N is a mutant of BP1 carries the tensile strength, Young's modulus, and birefringence negative motif GPQ.

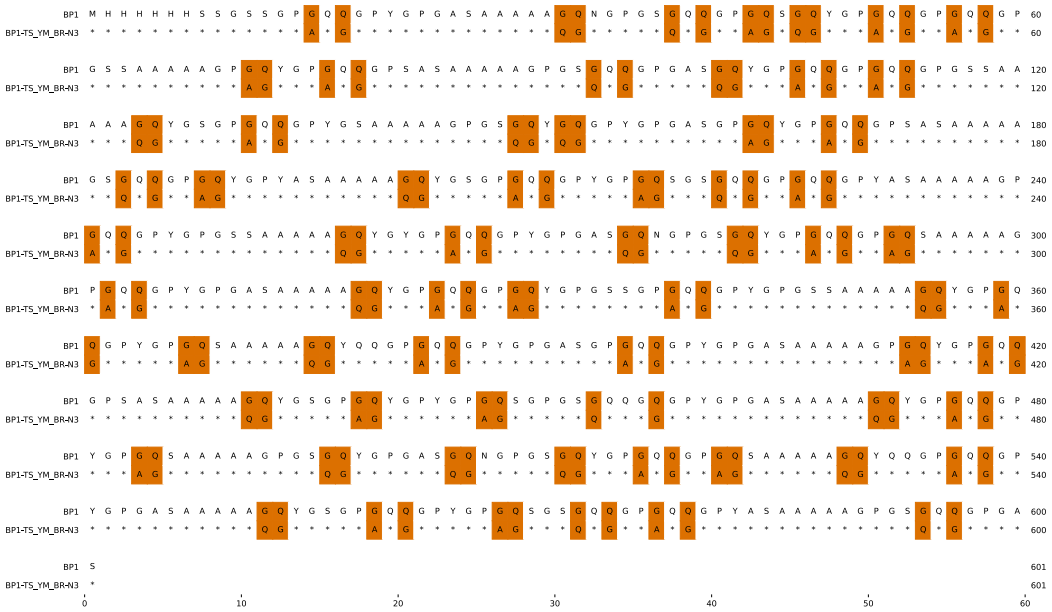

Figure 3-10. Amino acid sequence alignment of the protein BP1 and the tensile strength, Young's modulus, and birefringence negative mutant BP1-TS_YM_BR-N3.

The left-hand labels identify the reference sequence BP1 and the mutant BP1-TS_YM_BR-N3. In the BP1-TS_YM_BR-N3 line, an asterisk (*) marks residues identical to BP1, and orange shading highlights substituted residues. The rightmost numbers indicate position number for each sequence. BP1-TS_YM_BR-N3 is a mutant of BP1 to study the effect of the tensile strength, Young's modulus, and birefringence negative motif GPQ. It substitutes GPQ and crystallinity negative motif GQ.

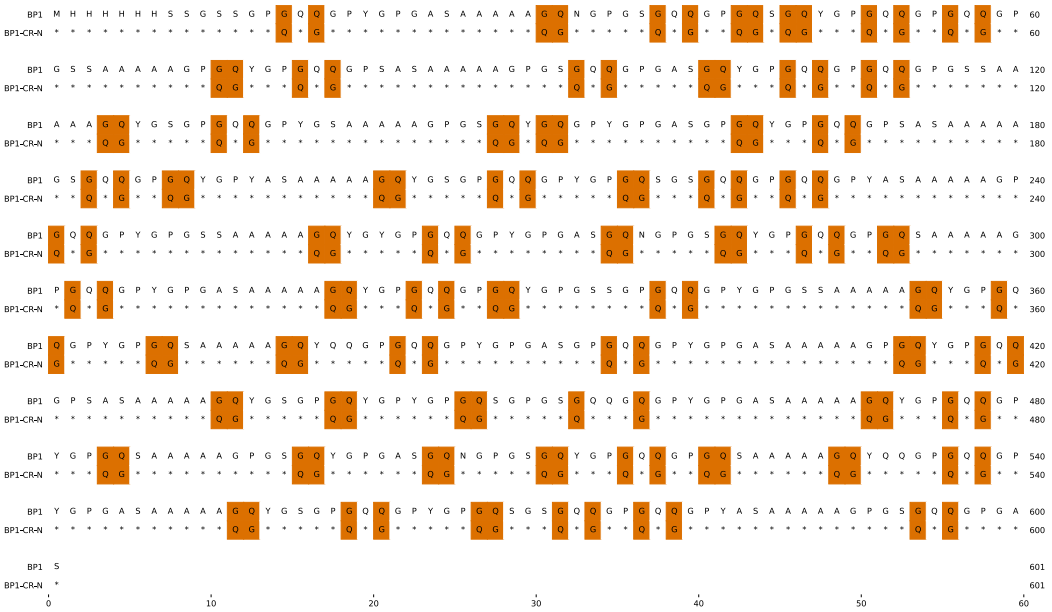

Figure 3-11. Amino acid sequence alignment of the protein BP1 and the crystallinity negative mutant BP1-CR-N.

The left-hand labels identify the reference sequence BP1 and the mutant BP1-CR-N. In the BP1-CR-N line, an asterisk (*) marks residues identical to BP1, and orange shading highlights substituted residues. The rightmost numbers indicate position number for each sequence. BP1-CR-N is a mutant of BP1 to study the effect of the crystallinity negative motif GQ. GQ→QG was modified with a crystallinity negative motif GQ. Since BP1 contains the motifs, GQ→QG reduces GQ by substituting with QG.

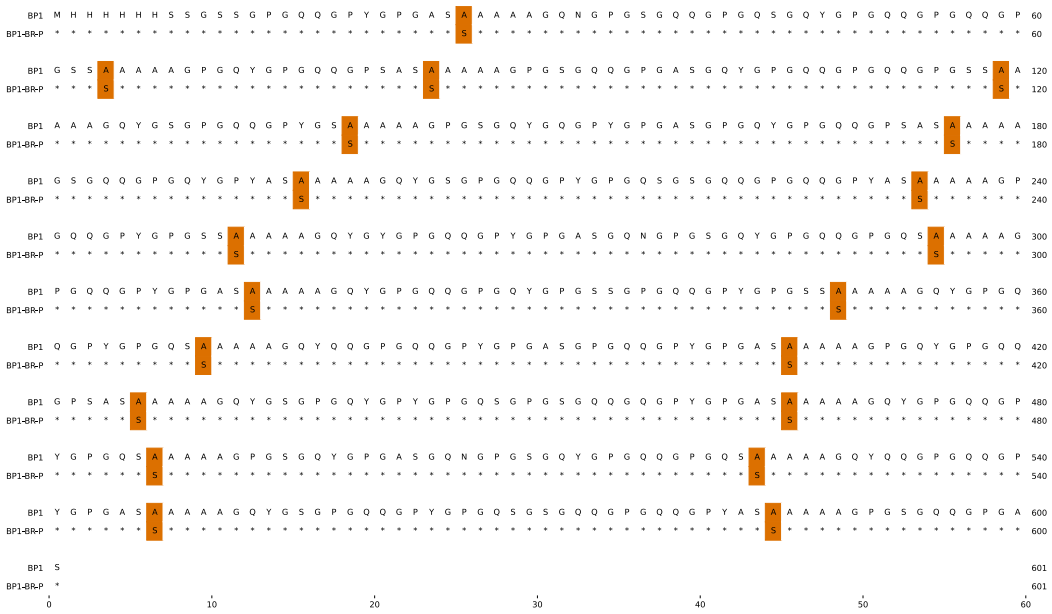

Figure 3-12. Amino acid sequence alignment of the protein BP1 and the birefringence positive mutant BP1-BR-P.

The left-hand labels identify the reference sequence BP1 and the mutant BP1-BR-P. In the BP1-BR-P line, an asterisk (*) marks residues identical to BP1, and orange shading highlights substituted residues. The rightmost numbers indicate position number for each sequence. BP1-BR-P is a mutant of BP1 to study the effect of the birefringence negative motif SSA. BP1-BR-P is a mutant of BP1 carries the birefringence positive motif SSA, which replaces the corresponding segment in BP1.

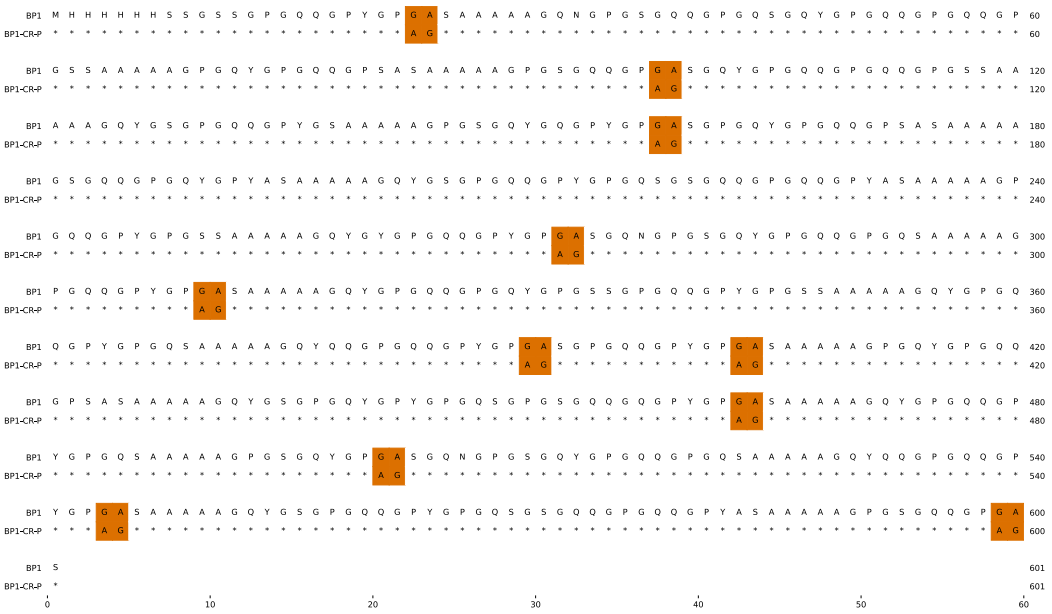

Figure 3-13. Amino acid sequence alignment of the protein BP1 and the crystallinity positive mutant BP1-CR-P.

The left-hand labels identify the reference sequence BP1 and the mutant BP1-CR-P. In the BP1-CR-P line, an asterisk (*) marks residues identical to BP1, and orange shading highlights substituted residues. The rightmost numbers indicate position number for each sequence. BP1-CR-P is a mutant of BP1 to study the effect of the crystallinity positive motif GPGA. Since BP1 contains the motif GPGA, BP1-CR-P replaces GPGA by substituting with GPAG.

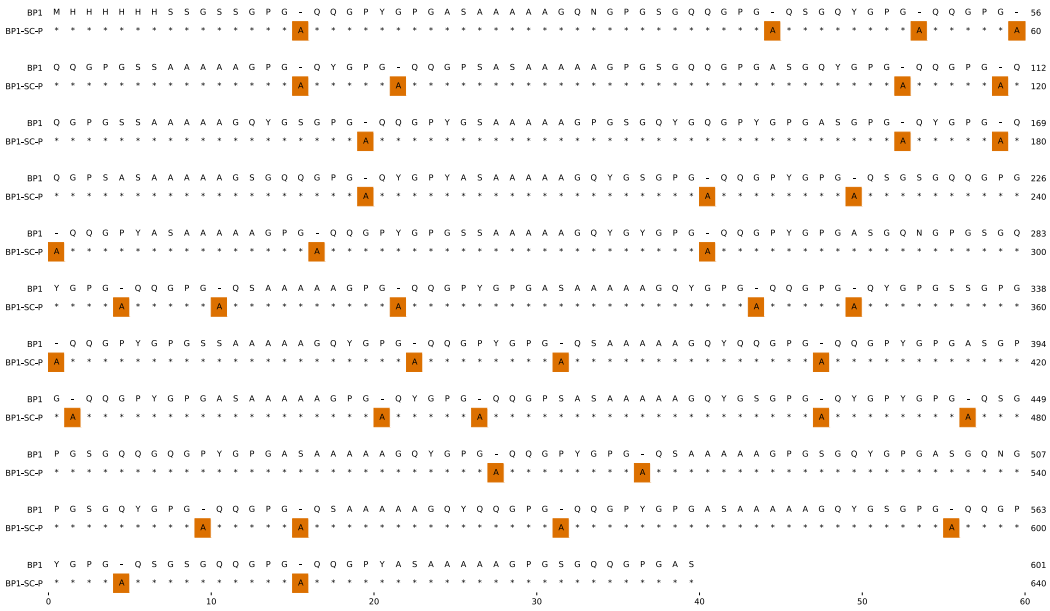

Figure 3-14. Amino acid sequence alignment of the protein BP1 and the supercontraction positive mutant BP1-SC-P.

The left-hand labels identify the reference sequence BP1 and the mutant BP1-SC-P. In the BP1-SC-P line, an asterisk (*) marks residues identical to BP1, and orange shading highlights substituted residues. The rightmost numbers indicate position number for each sequence. BP1-SC-P is a mutant of BP1 carries the supercontraction positive motif GPGA.

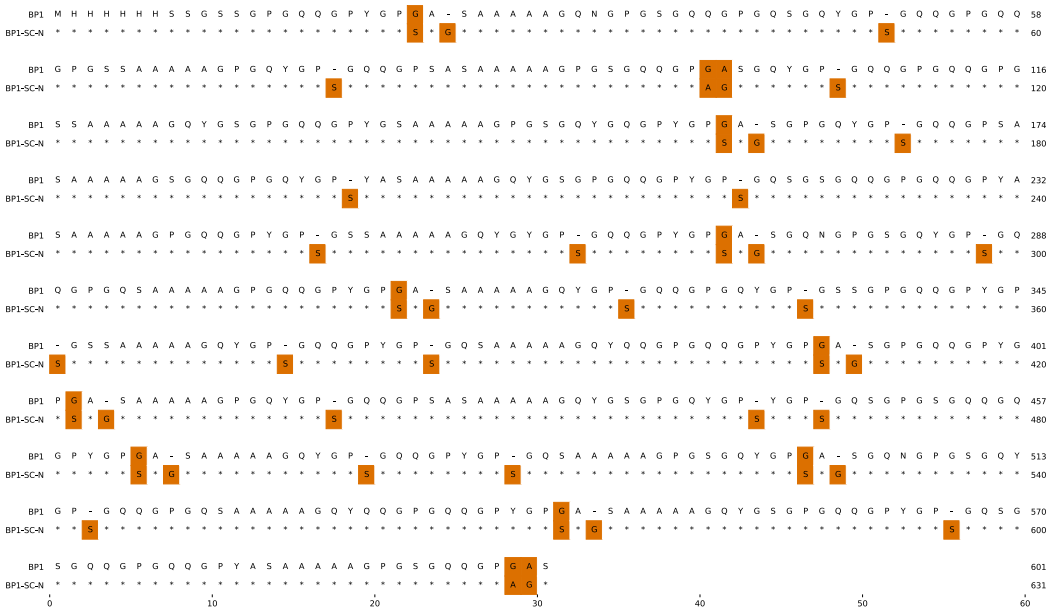

Figure 3-15. Amino acid sequence alignment of the protein BP1 and the supercontraction negative mutant BP1-SC-N.

The left-hand labels identify the reference sequence BP1 and the mutant BP1-SC-N. In the BP1-SC-N line, an asterisk (*) marks residues identical to BP1, and orange shading highlights substituted residues. The rightmost numbers indicate position number for each sequence. BP1-SC-N is a mutant of BP1 to study the effect of the supercontraction negative motif YGPS. It carries the supercontraction negative motif YGPS, while removes supercontraction positive motif GPGA.

3.2.3 Spinning of the artificial fibers from recombinant spidroins

The method used to prepare the artificial spider silk fibers was based on a previously described method (Asakura *et al.* 2022a) with modifications. Lyophilized powders of the recombinant spidroins were dissolved in 98 % formic acid at a concentration of 36 % (w/w) at 40 ℃ and stirred until complete dissolution. The spidroin solution was extruded under pressure using an N^2 pump and a 0.2 mm diameter nozzle at 40 °C. The extruded solution was then spun directly into containing methanol (MeOH) baths at 5 °C without an air gap (Asakura *et al.* 2022a, 2022b), followed by a second MeOH bath and a water bath at room temperature. The second MeOH bath at room temperature is used to extend the coagulation time to 1 minute, and the water bath is used to draw the fiber. The fiber was drawn in the water bath and then wound into bobbins at the winder. As the fiber was drawn solely within the washing bath (Figure 3-16), the draw ratio was calculated by dividing the linear speed of the roller after the washing bath by the linear speed of the roller before the bath. The schematic diagram of the instrument used for spinning is shown in Figure 3-16. The draw ratio of the fiber used in the experiment was 3, 4, 5, and 6 times. Finally, the bobbins were stored in dry boxes at 25 °C and used for subsequent analysis.

3.2.4 Scanning electron microscopy and the cross-sectional area calculation

Surface morphology and cross-sectional structure of the artificial spider-silk fibers were analyzed using the method described in Chapter 2.

3.2.5 Tensile properties of artificial spider silk fibers

The mechanical properties of the fibers were measured using FAVIMAT+ automatic single fiber testing system (Textechno H. Stein GmbH & Co. KG) with a 210 cN load cell at a strain rate of 10 mm/min at 20 °C and RH 65%. The initial length of the single silk fiber was set to 20 mm. The extension speed was applied at 10 mm/min, and the force during the test was measured with a 210 cN load cell. At least ten specimens were prepared for each sample. Tensile strength, Young's modulus, strain at break, and toughness were obtained from the stress-strain curves. To calculate the tensile strength, we determined the cross-sectional areas of the fiber specimens based on their diameters, which were determined by SEM observations. To calculate the mechanical properties, we analyzed the force-displacement data as previously described (Arakawa *et al.* 2022). The significant digits of the mechanical properties were determined according to a previous report (Arakawa *et al.* 2022).

3.2.6 Shrinkage in boiling water measurement

To evaluate the effects of the motifs, which have a positive and negative correlation to the supercontraction, we used the shrinkage in boiling water measurement. The boiling water measurement test is conducted by measuring the length of the fiber immersion to the water and subsequent drying. Usually, evaluating supercontraction in terms of the shrinkage length is done by measuring the difference in the length before and after immersion in the water or exposure to humidity (Work 1977; Shao and Vollrath 1999; Guinea *et al.* 2012; Arakawa *et al.* 2022; Nakamura *et al.* 2023). To assess the fibers' reactivity to an industrial environment, where high-temperature water is employed in processes such as dyeing and washing, we employed shrinkage in boiling water measurement. For this purpose, the fibers were subjected to a temperature of 98°C, which is in accordance with the ISO18066:2015 standard for industrial environments.(International Organization for Standardization 2015) Shrinkage in boiling water and subsequent drying was measured using the following procedures. Test specimens were prepared by cutting the recombinant spidroin fibers to 30 cm (L_0) and bundling 7 cut fibers into a fiber bundle. Both ends of the bundle were fixed with the pieces of tape. We then immersed the fiber bundle in water at 98°C for 10 minutes without any fixation and measured the length immediately after immersion (L_1), and the percentage of shrinkage was calculated by $(L_0 - L_1)/L_0 \times 100$ and then allowed to air dry for 24 hours in an unrestrained state. The final fiber length (L_f) was measured and the percentage shrinkage after drying was calculated as $(L_0 - L_f)/L_0 \times 100$. The percentage of shrinkage was determined by applying the same methodology used in the previous study (Nakamura *et al.* 2023). Three replicates were made for each sample. Throughout the experiment, the room temperature was 25℃ and the relative humidity was around 30%.

3.2.7 Birefringence measurement

The fiber’s birefringence was calculated from its retardation and diameter, following the method described in Chapter 2.

3.2.8 Wide-angle X-ray scattering (WAXS) measurement

WAXS measurements were performed with an X-ray diffractometer (Rigaku XtaLAB-SP X-ray) as previously described (Tachibana *et al.* 2021). Cu-Kα radiation was used at a wavelength of 0.154 nm. The voltage was set to 40 kV and the current was 30 mA. The sample-to-detector distance for the WAXS measurements was 63 mm. The exposure time for each diffraction pattern was 100 seconds. The resulting data were converted into one-dimensional radial integration profiles using. The resulting data were corrected by subtracting the background scattering. The crystallinity was calculated from the area of crystal peaks divided by the total area of crystal peaks and the amorphous halo by fitting the Gaussian function in accordance with the previous work

(Numata *et al.* 2015; Nakamura *et al.* 2023). The orientation of the crystal *a*-axis, *b*-axis, and *c*-axis were calculated by the software Degree of Preferred Orientation Analysis version 3.2.0.0 (Rigaku, Japan).

3.2.9 Molecular dynamics simulation of the repetitive region of the BP1 mutants

Energy minimization and molecular dynamics (MD) calculations were conducted in accordance with the previously described methodology (Nagano *et al.* 2009). The MD calculations were performed using Materials Studio 2023 software (BIOVIA Inc.), with the COMPASS III force field (Akkermans, Spenley and Robertson 2021) and the particle-particle particle-mesh (PPPM) summation method for all simulations. The amino acid sequence was extracted from BP1, which consists of 31 residues with polyalanine in the middle (N-PGQQGPGQQGPGAAAAAAAGPGQYGPGQQGP-C). The peptide structures were generated with Avogadro (Hanwell *et al.* 2012) (v1.2.0), and a total of eight types were generated by replacing polyalanine with serine. The Protein Data Bank (PDB) formatted files of the generated peptides were arranged in Materials Studio Visualizer with 6×6 peptides arranged in antiparallel and 15 Å spacing. The initial structures were generated by energy minimization under controlled conditions of ultra-fine quality mode and external pressure of 0.1 MPa using Geometry Optimization in the Forcite module of the Materials Studio. The final structures were generated using Forcite Dynamics within an NPT ensemble at a temperature of 298.0 K and a pressure of 0.1 MPa, with a time step of 1.0 fs. The total simulation time was 50 ps.

3.3 Results

To confirm the effects of the motifs extracted from the spider silkome database on the mechanical properties of the artificial spider silk and to explore the possibility of controlling the mechanical properties of the artificial spider silk, we conducted experiments to produce artificial spider silk with motif-modified mini-spidroins and then compared the mechanical properties of the fibers produced with the artificial spinning method. As shown in Figure 3-17A, we first created artificial mini-spidroin mutants with modifications based on the motifs that correlated with the physical properties found in natural spidroins. We began by selecting the amino acid sequence motifs of MaSp2 that correlated with physical properties (tensile strength, strain at break, Young's modulus, and toughness) and structural properties (crystallinity and birefringence), as well as supercontraction, based on our previous report on the relationship between amino acid sequences and properties (Arakawa *et al.* 2022). Next, we designed motif-substituted BP1 mutant sequences and then produced the recombinant mini-spidroin. Artificial spider silks were then spun from the mini-spidroin dope solutions using formic acid as the solvent, and methanol as a solvent for the coagulation bath with different drawing ratios. Finally, we performed tensile tests to measure the

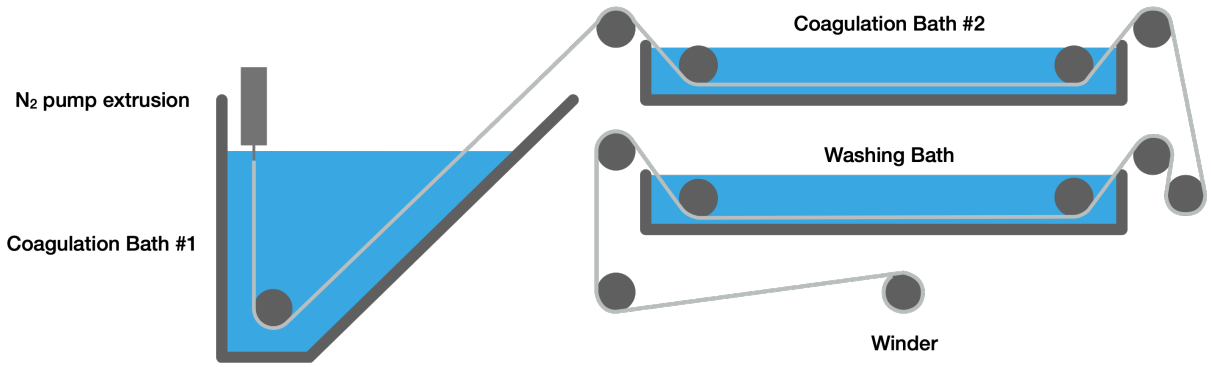

Figure 3-16. Schematic diagram of the spinning instrument used in this study.

The N2 pump is used for the extrusion of the spinning dopes. Coagulation bath #1 was MeOH at 5 °C. Coagulation bath #2 was MeOH at room temperature. The washing bath was tap water at room temperature. The drawing was done in the washing bath. The fibers were wound into bobbins at the winder. All rollers excluding the roller in the coagulation bath #1 were driven at a constant speed by motors.

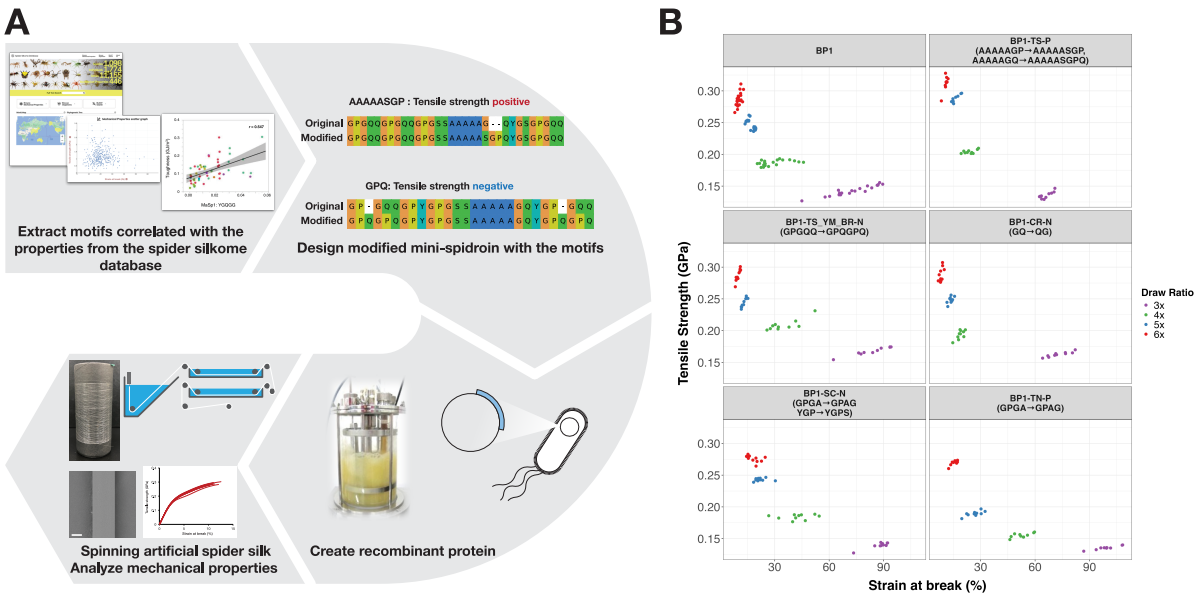

Figure 3-17. Schematic diagram of the experimental workflow (left), and the tensile strength and strain at break of modified BP1 artificial spider silk (right).

In the scatter plot, each box indicates the properties of the natural spider silk that correlate with the motifs used to modify the BP1 sequence, and the colors of the markers indicate the effect of the motifs, the type of marker indicates the draw ratio of the fibers.

mechanical properties of the fiber and analyzed the effects of the motifs on the physical properties of the artificial spider silks by measuring their boiling water shrinkage. Figure 3-17B shows a scatter plot of the tensile strength and strain at break of all tested specimens from the study. This shows the diversity of the stress-strain behavior of the BP1 fibers modulated by the motifs extracted from the Spider Silkome Database.

3.3.1 Spidroin design with the motifs extracted from the 1,000 spider spidroins and the gene construction

Table 3-2 shows the motifs used in this study. Since BP1 is an artificial mini-spidroin based on MaSp2, we selected MaSp2 motifs that correspond to physical and structural properties. For each property, we selected motifs with the highest negative and positive correlations. If the specific pattern we are studying already existed in BP1, we reduced its occurrence by replacing it with a different pattern, ensuring that we keep the same amino acid composition as much as possible. For example, to study the effects of the 'GQ' pattern, which reduces crystallinity, we changed 'GQ' to 'QG' in the mutant. If BP1 does not have the pattern we want to examine, we modified BP1 by adding or replacing the necessary patterns. To ensure that these changes do not introduce side effects, we carefully avoided increasing the molecular weight during these modifications. Figures 3-1 to 3-15 show the amino acid sequences of the mutant BP1s. Interestingly, substitution of the motifs did not result in any negative changes in the expression of the mutant mini-spidroins by *E. coli*, as shown in Figure 3-18.

3.3.2 Effects of the sequence motifs for the mechanical properties of the artificial spider silks

A summary of the effects of the motifs on the mechanical properties of artificial spider silk are shown in Table 3-3 and Table 3-4. Each cell in the table indicates the percentage change in the mechanical properties of the fiber compared to the unmodified BP1 fiber at the same draw ratio. The blank cells indicate no significant changes. The effects of the motifs on tensile strength are consistent with their correlations; motifs positively correlated with tensile strength increase it, whereas those negatively correlated reduce it, as shown in Figure 3-19. The difference in the tensile strength is repeatedly confirmed in the different draw ratios (4 and 5 times). Furthermore, the significance of the difference between the tensile strength is confirmed by the Wilcoxon rank sum test, and the probability is smaller than 0.0001. Detailed data, including stress-strain curves, mechanical properties, SEM images, and fiber birefringence of the BP1 mutants are documented in Figures 3-20 to 3-32. Although the tensile-strength-positive and -negative mutants behaved as expected, Young's modulus showed no significant change for any of the motif substitutions. In the case of toughness, motifs predicted to positively or negatively influence toughness both resulted in an increase, as shown in Figures 3-21 and 3-22. Contrary to the expectations for strain at break,

Table 3-2. MaSp2 motifs extracted from the Spider Silkome Database and their relationship with properties.

Property	Motif	
	Positive effect	Negative effect
Tensile strength	AAAAASGP (0.292)	GPQ (−0.285) PQ (−0.243)
Young's modulus	PA (0.505)	GPQ (−0.267) PQ (−0.249)
Strain at break	QGPSG (0.280)	AAASA (−0.407)
Toughness	PA (0.302)	GPGSQGP (−0.289)
Crystallinity	GPA (0.582)	GQ (−0.324) SQ (−0.258)
Birefringence	SSA (0.434)	GPQ (−0.183)
Supercontraction	GPGA (0.474)	YGPS (−0.561)

The numbers under the motifs are Pearson correlation coefficients for the properties

Table 3-3. Effects of the motifs for recombinant artificial spider silks.

Property	Motif	Substitution pattern	Positive / Negative effects in natural spidroins	Effects in recombinant artificial spider silk (%)			
				Tensile strength	Young's modulus	Strain	Toughness
Tensile strength	AAAAASGP	AAAAAAGP → AAAAASGP AAAAAGQ → AAAAASGPQ	Positive	9.3			
	GPQ	GPGQQ → GPQGPQ PGQ → GPQ SSA → SAS	Negative	-5.1			
Young's modulus	PA	GPG → GPA	Positive				
	GPQ	GPGQQ → GPQGPQ GQ → QG GPQ → GPA	Negative				
Strain at break	QGPSG	QGPY → QGPSGY	Positive	13.4	7.8	-26.6	-19.7
	AAASA	AAAAA → AAASA	Negative	14.9	7.0		26.2
Toughness	PA	GPGA → GPAG	Positive	-5.9		49.3	58.4
	GPGSQGP	GPGQQGP → GPGSQGP	Negative			38.2	38.0
Crystallinity	GPA	GPG → GPAG	Positive			26.0	34.1
	GQ	GQ → QG	Negative			25.3	23.9
Birefringence	SSA	SAA → SSA	Positive	ND	ND	ND	ND
	GPQ	PGQ → GPQ SSA → SAS	Negative	-5.1			
Supercontraction	GPGA	GPGQ → GPGAQ GPGA → GPAG	Positive	6.2		-33.0	-36.9
	YGPS	GPGA → GPAG YGP → YGPS	Negative			80.4	95.8

100%
-100%

Substitution pattern describes substitution formatted by from → to pattern. The number in the effects in recombinant artificial spider is the percentage of the properties of the fiber with 6 times drawing ratio compared to the fibers with the same drawing ratio of BP1.

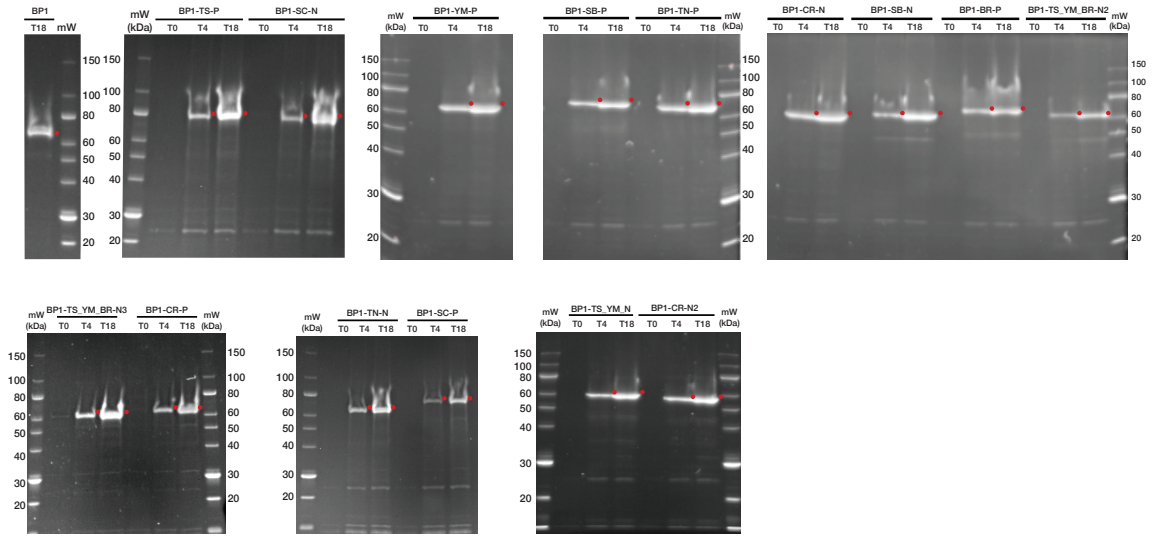

Figure 3-18. SDS-PAGE visualization of BP1 and BP1 mutants recombinant protein expression.
Whole-cell lysates of *E. coli* BL21(DE3) expressing the parental protein BP1 or the indicated BP1 mutants were collected immediately before induction (T0) and after 4 h (T4) and 18 h (T18) of expression at 37 °C with IPTG. Samples were separated on 15 % polyacrylamide gels, and proteins were visualised with InVision™ His-Tag stain. "mW" denotes the molecular-weight ladder (kDa). Red dots mark the bands corresponding to the His-tagged recombinant proteins. The left-most panel shows BP1; the remaining panels are grouped by mutant name as indicated above each gel.

motifs predicted to increase strain actually decreased it, and those predicted to decrease strain had no effect. However, both types of strain at break motifs unexpectedly increased tensile strength. Fiber birefringence was also examined: BP1-TS_YM_BR-N2 modified with motifs predicted to reduce birefringence (PGQ→GPQ, SSA→SAS) exhibited lower birefringence than unmodified BP1 at all draw ratios, as shown in Figure 3-32. Finally, as detailed in Table 3-5, modifications of motifs associated with positive or negative effects on crystallinity did not significantly alter fiber crystallinity at any draw ratio (Figure 3-33). Motif to increase birefringence with a specific motif change (BP1-BR-P: SAA→SSA) was not successful, which will be discussed further in subsequent sections.

3.3.3 Effects of the sequence motifs for the boiled water shrinkage rate

Measurements were performed to investigate the response of the recombinant artificial spider silk fiber in water at 98°C. Table 3-6 shows the boiled water shrinkage rate, shrinkage after drying, and total shrinkage for each motif-substituted mutant. The boiled water shrinkage rate for the BP1-BR-P (substitution pattern: 'SAA→SSA') could not be measured due to the unavailability of the fiber sample. For mutants BP1-TS-P (substitution pattern: 'AAAAAAGP→AAAAASGP, AAAAAGQ→AAAAASGPQ'), BP1-CR-N (substitution pattern: 'GQ→QG') , and BP1-SC-N (substitution pattern: 'GPGA→GPAG, YGP→YGPS'), the boiled water shrinkage rate could not be measured due to fiber breakage in the hot bath or after drying. Most of the shrinkage assays showed no significant difference from the control. However, BP1-TS_YM_N (substitution pattern: 'QQ→SQ') and BP1-CR-N2 (substitution pattern: 'QQ→PQ') had significantly lower total shrinkage rates than the control (see Table 3-7 and Figure 3-34). For both the control and the motif-substituted mutant, we observed an increase in boiled water shrinkage with increasing draw ratio. In addition, we observed a decrease in shrinkage after drying with increasing draw ratio.

3.3.4 The SSA motif makes significant changes in the spinnability of the artificial spider silk

The mutant with the birefringence-positive motif SSA, BP1-BR-P (Figure 3-12) did not form fibers under the tested conditions. After the coagulate on bath, the fibers drawn in the water bath dissolved. To observe the surface morphology of the fiber, we reeled it without passing through the water bath. The SEM image in Figure 3-35B shows that the fiber was extremely brittle and weakened. The effects of the modification were valuated using molecular dynamics simulation. Since BP1-BR-P has two and three serine residues before polyalanine, we created the models with two and three serine residues before polyalanine. The simulation results showed a slightly distorted polyalanine β-sheet structure when the three serine residues precede the polyalanine as shown in Figure nine as shown in Figure 3-35C.

Table 3-4. Mechanical properties of the motif substituted BP1 mutants and percentage changes in mechanical properties compared to BP1.

Motif Substitution Pattern	Draw Ratio	Property	Average Value	p value (Wilcoxon rank sum test)	Percentage Change (%)
AAAAAGP→AAAAASGP AAAAAGQ→AAAAASGPQ	4	Strain (%)	24.0	0.0862	-18.2
	5		16.0	0.2525	-5.4
	6		10.8	0.2262	4.8
	4	Tensile strength (GPa)	0.204	0.0000	9.3
	5		0.287	0.0000	16.2
	6		0.312	0.0001	9.1
	4	Toughness (GJ/m^3)	0.042	0.5526	-13.1
	5		0.036	0.2619	9.5
	6		0.024	0.0263	13.4
	4	Young's modulus (GPa)	6.23	0.0083	7.1
	5		7.28	0.0003	11.4
	6		7.20	0.8088	1.2
GPGQQ→GPQGPQ	4	Strain (%)	35.1	0.0503	19.7
	5		13.1	0.0001	-22.9
	6		9.9	0.3910	-4.0
	4	Tensile strength (GPa)	0.209	0.0000	11.9
	5		0.244	0.2437	-1.3
	6		0.288	0.6441	0.4
	4	Toughness (GJ/m^3)	0.065	0.0101	35.9
	5		0.025	0.0001	-25.1
	6		0.020	0.9124	-1.7
	4	Young's modulus (GPa)	4.86	0.7918	-16.4
	5		5.74	0.0006	-12.1
	6		6.94	0.2098	-2.6
PGQ→GPQ SSA→SAS	4	Strain (%)	26.1	0.4891	-11.0
	5		14.2	0.0017	-16.0
	4	Tensile strength (GPa)	0.180	0.0010	-3.8
	5		0.235	0.0002	-5.1
	4	Toughness (GJ/m^3)	0.040	0.4891	-15.7
	5		0.027	0.0009	-18.3
	4	Young's modulus (GPa)	6.00	0.1502	3.2
	5		6.81	0.0528	4.2
GPG→GPA	4	Strain (%)	21.6	0.0005	-26.2
	5		15.6	0.2098	-8.2
	6		7.8	0.0000	-24.1
	4	Tensile strength (GPa)	0.202	0.0000	8.5
	5		0.257	0.0146	3.8
	6		0.273	0.0030	-4.7
	4	Toughness (GJ/m^3)	0.035	0.0019	-26.7
	5		0.030	0.1658	-7.7
	6		0.015	0.0001	-29.2
	4	Young's modulus (GPa)	6.00	0.0712	3.3
	5		6.58	0.7918	0.7
	6		7.11	0.8775	-0.2
GQ→QG GPQ→GPA	4	Strain (%)	28.7	0.7749	-2.0
	5		14.9	0.0146	-12.3
	6		9.4	0.1591	-8.5
	4	Tensile strength (GPa)	0.240	0.0000	28.4
	5		0.287	0.0000	16.1
	6		0.330	0.0000	15.1
	4	Toughness (GJ/m^3)	0.059	0.0366	23.4
	5		0.033	0.8431	-0.7
	6		0.022	0.4414	3.9
	4	Young's modulus (GPa)	6.42	0.0000	10.3
	5		6.77	0.1289	3.6
	6		7.47	0.0477	4.8
QGPY→QGPSGY	4	Strain (%)	18.7	0.0002	-36.1
	5		12.4	0.0000	-26.6
	4	Tensile strength (GPa)	0.218	0.0000	16.7
	5		0.280	0.0000	13.4
	4	Toughness (GJ/m^3)	0.035	0.0068	-27.6
	5		0.026	0.0001	-19.7
	4	Young's modulus (GPa)	7.50	0.0000	29.0
	5		7.04	0.0030	7.8
AAAAA→AAASAA	4	Strain (%)	42.3	0.0007	44.3
	6		10.9	0.1402	5.5
	4	Tensile strength (GPa)	0.201	0.0000	7.4
	6		0.329	0.0000	14.9
	4	Toughness (GJ/m^3)	0.077	0.0002	61.7
	6		0.026	0.0003	26.2
	4	Young's modulus (GPa)	6.51	0.0000	11.9
	6		7.62	0.0059	7.0
GPGA→GPAG	4	Strain (%)	52.7	0.0000	79.7
	5		26.6	0.0000	56.9
	6		15.4	0.0000	49.3
	4	Tensile strength (GPa)	0.155	0.0000	-17.0
	5		0.189	0.0000	-23.4
	6		0.269	0.0001	-5.9
	4	Toughness (GJ/m^3)	0.076	0.0001	58.0
	5		0.044	0.0014	32.8
	6		0.033	0.0000	58.4
	4	Young's modulus (GPa)	5.592	0.0277	-3.8
	5		5.562	0.0000	-14.8
	6		6.736	0.0502	-5.4

(continued)

GPGQQGP→GPGSQGP	4	Strain (%)	55.1	0.0000	87.7
	5		23.7	0.0000	39.8
	6		14.3	0.0000	38.2
	4	Tensile strength (GPa)	0.212	0.0000	13.3
	5		0.251	0.2619	1.6
	6		0.258	0.0000	-10.0
	4	Toughness (GJ/m^3)	0.103	0.0000	115.8
	5		0.051	0.0000	54.7
	6		0.029	0.0001	38.0
	4	Young's modulus (GPa)	6.20	0.0021	6.6
	5		6.74	0.2711	3.2
	6		6.24	0.0001	-12.4
GPG→GPAG	4	Strain (%)	47.4	0.0001	61.7
	5		21.2	0.0002	25.1
	6		13.0	0.0008	26.0
	4	Tensile strength (GPa)	0.187	0.9825	0.1
	5		0.244	0.5235	-1.4
	6		0.282	0.3671	-1.5
	4	Toughness (GJ/m^3)	0.079	0.0001	64.2
	5		0.042	0.0004	28.8
	6		0.028	0.0009	34.1
	4	Young's modulus (GPa)	5.58	0.0584	-4.1
	5		6.46	0.7580	-1.1
	6		7.04	0.5822	-1.2
GQ→QG	4	Strain (%)	18.7	0.0000	56.6
	5		13.5	0.0001	25.9
	6		8.2	0.0002	25.3
	4	Tensile strength (GPa)	0.194	0.0078	-3.7
	5		0.248	0.6129	-0.4
	6		0.288	0.7749	-0.7
	4	Toughness (GJ/m^3)	0.031	0.0001	55.8
	5		0.025	0.0001	29.1
	6		0.017	0.0034	23.9
	4	Young's modulus (GPa)	6.12	0.0078	-5.0
	5		6.56	0.8430	-0.5
	6		7.51	0.0328	-5.2
GPGQ→GPGAQ	4	Strain (%)	33.4	0.0615	13.9
	5		18.0	0.5379	6.1
	6		10.5	0.7083	2.1
	4	Tensile strength (GPa)	0.191	0.0186	2.2
	5		0.188	0.0000	-23.9
	6		0.294	0.0503	2.6
	4	Toughness (GJ/m^3)	0.055	0.0679	15.6
	5		0.026	0.0001	-20.1
	6		0.022	0.2099	6.8
	4	Young's modulus (GPa)	5.80	0.9824	-0.3
	5		4.95	0.0000	-24.2
	6		7.11	0.7413	-0.2
GPGA→GPAG **YGP→YGPS**	4	Strain (%)	42.2	0.0012	44.0
	5		22.2	0.0001	30.9
	6		18.6	0.0000	80.4
	4	Tensile strength (GPa)	0.184	0.1797	-1.3
	5		0.243	0.3910	-1.8
	6		0.276	0.0045	-3.8
	4	Toughness (GJ/m^3)	0.069	0.0026	44.7
	5		0.045	0.0000	36.4
	6		0.041	0.0000	95.8
	4	Young's modulus (GPa)	5.88	0.4545	1.1
	5		6.74	0.2263	3.1
	6		7.35	0.2712	3.3
QQ→SQ	4	Strain (%)	35.8	0.0294	22.0
	5		16.5	0.4544	-2.5
	6		11.0	0.1289	7.0
	4	Tensile strength (GPa)	0.194	0.0014	4.0
	5		0.199	0.0000	-19.3
	6		0.301	0.0010	5.2
	4	Toughness (GJ/m^3)	0.062	0.0165	29.1
	5		0.025	0.0002	-25.3
	6		0.024	0.0186	13.9
	4	Young's modulus (GPa)	5.51	0.0013	-5.3
	5		4.81	0.0000	-26.4
	6		6.87	0.1657	-3.5
QQ→PQ	4	Strain (%)	17.4	0.0000	-40.6
	5		14.6	0.0034	-14.0
	6		10.6	0.4157	2.9
	4	Tensile strength (GPa)	0.176	0.0005	-5.5
	5		0.242	0.1291	-2.0
	6		0.280	0.1083	-2.2
	4	Toughness (GJ/m^3)	0.026	0.0000	-45.7
	5		0.028	0.0019	-15.9
	6		0.022	0.4157	3.7
	4	Young's modulus (GPa)	5.95	0.1795	2.2
	5		6.68	0.3222	2.3
	6		6.83	0.0614	-4.1

Motif substitution pattern, draw ratio, property, average values of the properties, *p* values determined by the Wilcoxon rank sum test, and percentage changes in the mechanical properties compared to BP1.

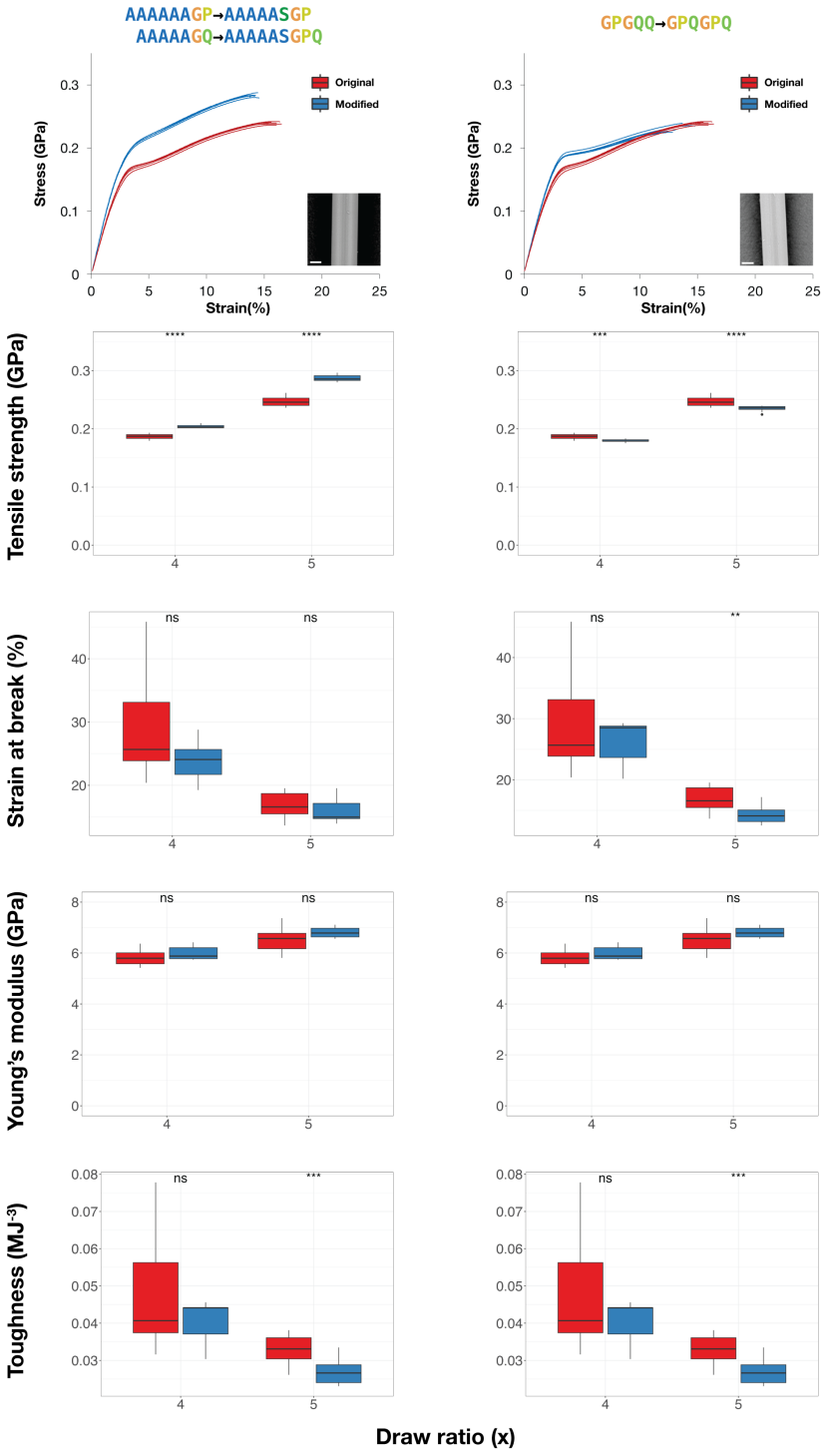

Figure 3-19. Stress-strain curve, SEM image, and mechanical properties with different draw ratios of BP1 and modified with tensile strength A) positive and B) negative motifs.

The stress-strain curves represent the fiber with a drawing ratio of 5. The number of test pieces in the stress-strain curve is 10. The scale bar in the SEM image is 20 μm. The marks above the box and whisker plots denote statistical significance. ns not significant, * $0.01 < p \leq 0.05$, ** $0.001 < p \leq 0.01$, *** $0.0001 < p \leq 0.001$, and **** $p \leq 0.0001$, as determined by the Wilcoxon rank sum test.

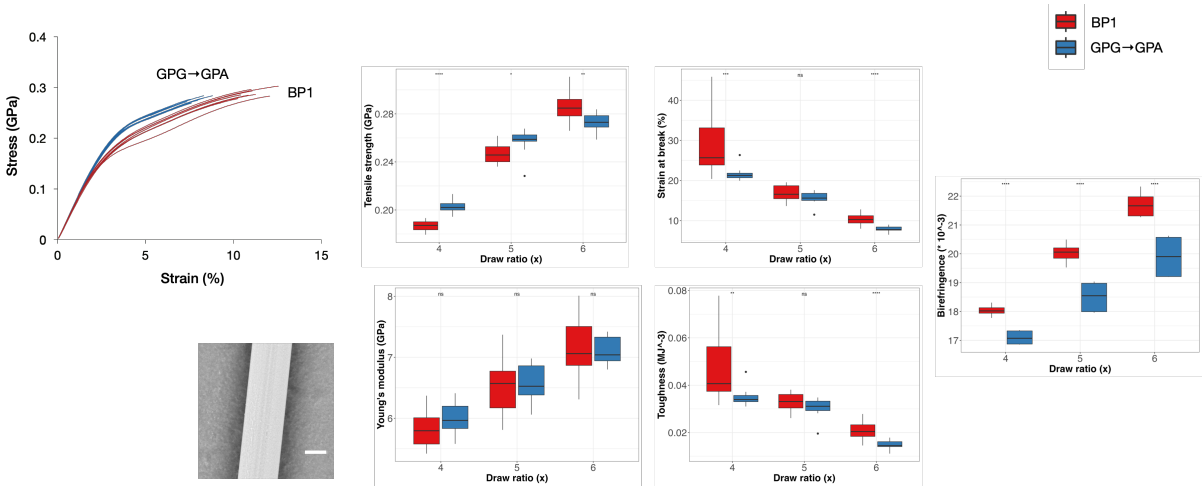

Figure 3-20. Stress-strain curve, SEM image, mechanical properties and birefringence of the fibers with different drawing ratio of BP1 and BP1-YM-P (substitution pattern: GPG→GPA).

The stress-strain curves and SEM images are 6 time drawing ratio of fiber. The number of test pieces in the stress-strain curve is 10. The scale bar in the SEM image is 20 μm. The marks above the box and whisker plots denote statistical significance. ns not significant, * $0.01 < p \leq 0.05$, ** $0.001 < p \leq 0.01$, *** $0.0001 < p \leq 0.001$, and **** $p \leq 0.0001$, as determined by the Wilcoxon rank sum test.

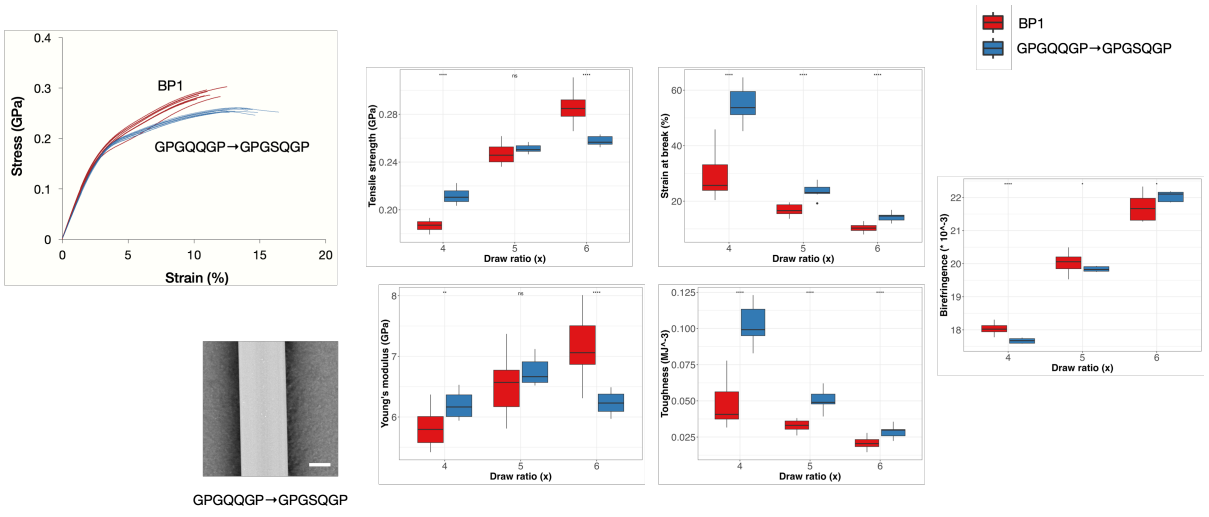

Figure 3-21. Stress-strain curve, SEM image, mechanical properties and birefringence of the fibers with different drawing ratio of BP1 and BP1-TN-N (substitution pattern: GPGQQGP→GPGSQGP).

The stress-strain curves and SEM images are 6 time drawing ratio of fiber. The number of test pieces in the stress-strain curve is 10. The scale bar in the SEM image is 20 μm. The marks above the box and whisker plots denote statistical significance. ns not significant, * $0.01 < p \leq 0.05$, ** $0.001 < p \leq 0.01$, *** $0.0001 < p \leq 0.001$, and **** $p \leq 0.0001$, as determined by the Wilcoxon rank sum test.

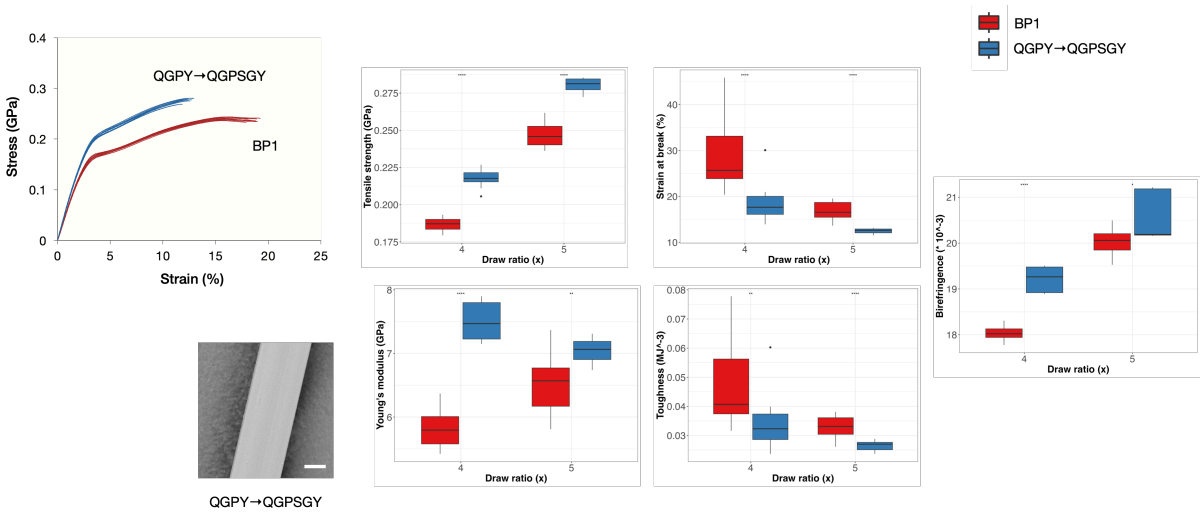

Figure 3-22. Stress-strain curve, SEM image, mechanical properties and birefringence of the fibers with different drawing ratio of BP1 and BP1-SB-P (substitution pattern: QGPY→QGPSGY).

The stress-strain curves and SEM images are 5 time drawing ratio of fiber. The number of test pieces in the stress-strain curve is 10. The scale bar in the SEM image is 20 μm. The marks above the box and whisker plots denote statistical significance. ns not significant, * $0.01 < p \leq 0.05$, ** $0.001 < p \leq 0.01$, *** $0.0001 < p \leq 0.001$, and **** $p \leq 0.0001$, as determined by the Wilcoxon rank sum test.

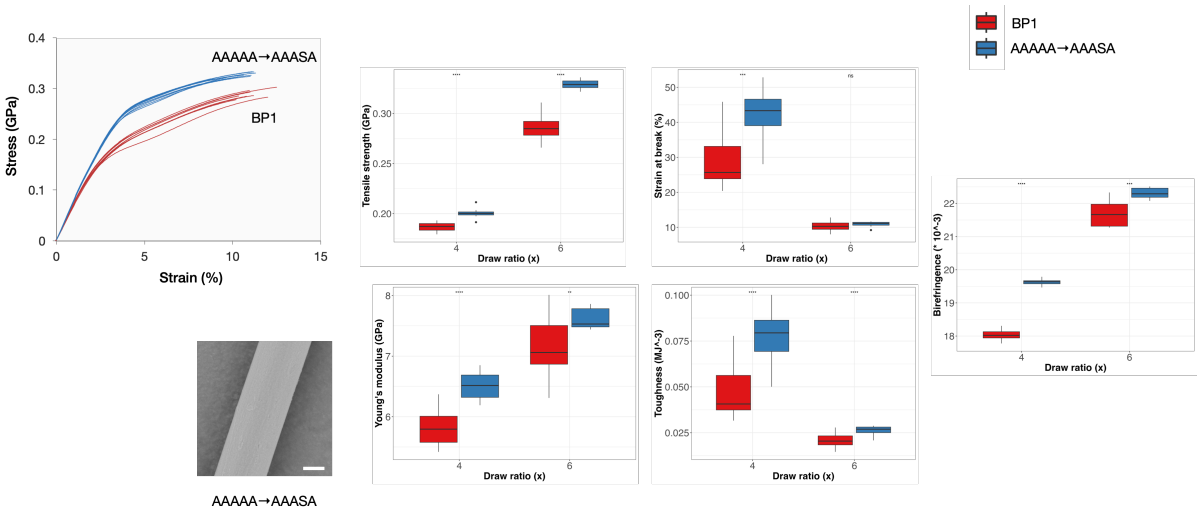

Figure 3-23. Stress-strain curve, SEM image, mechanical properties and birefringence of the fibers with different drawing ratio of BP1 and BP1-SB-N (substitution pattern: AAAAA→AAASA).

The stress-strain curves and SEM images are 6 time drawing ratio of fiber. The number of test pieces in the stress-strain curve is 10. The scale bar in the SEM image is 20 μm. The marks above the box and whisker plots denote statistical significance. ns not significant, * $0.01 < p \leq 0.05$, ** $0.001 < p \leq 0.01$, *** $0.0001 < p \leq 0.001$, and **** $p \leq 0.0001$, as determined by the Wilcoxon rank sum test.

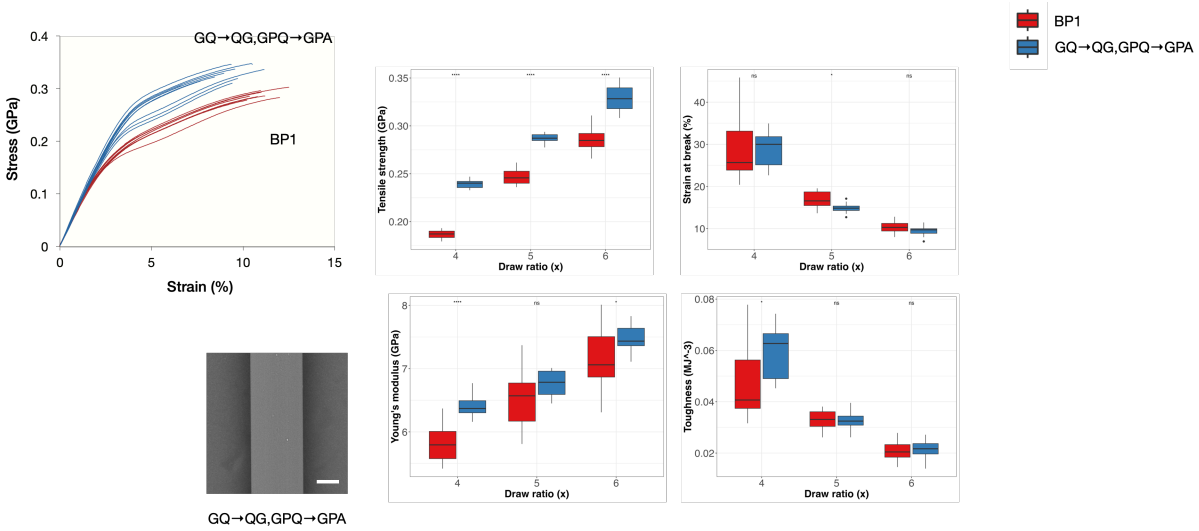

Figure 3-24. Stress-strain curve, SEM image, mechanical properties and birefringence of the fibers with different drawing ratio of BP1 and BP1-TN-P (substitution pattern: GPGA→GPAG).

The stress-strain curves and SEM images are 6 time drawing ratio of fiber. The number of test pieces in the stress-strain curve is 10. The scale bar in the SEM image is 20 μm. The marks above the box and whisker plots denote statistical significance. ns not significant, * $0.01 < p \leq 0.05$, ** $0.001 < p \leq 0.01$, *** $0.0001 < p \leq 0.001$, and **** $p \leq 0.0001$, as determined by the Wilcoxon rank sum test.

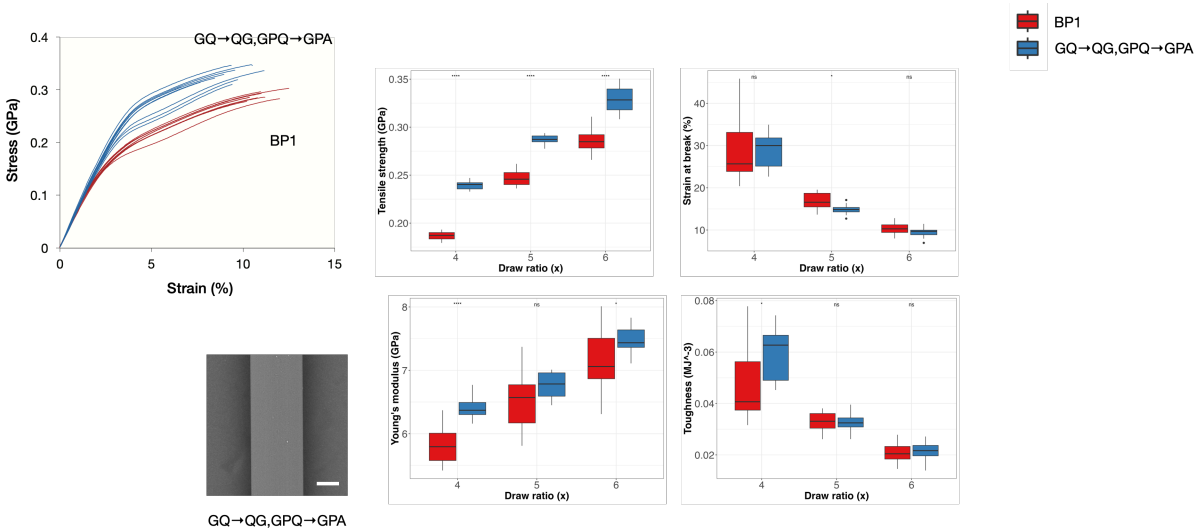

Figure 3-25. Stress-strain curve, SEM image, mechanical properties of the fibers with different drawing ratio of BP1 and BP1-TS_YM_BR-N3 (substitution pattern: GQ→QG,GPQ→GPA).

The stress-strain curves and SEM images are 6 time drawing ratio of fiber. The number of test pieces in the stress-strain curve is 10. The scale bar in the SEM image is 20 μm. The marks above the box and whisker plots denote statistical significance. ns not significant, * $0.01 < p \leq 0.05$, ** $0.001 < p \leq 0.01$, *** $0.0001 < p \leq 0.001$, and **** $p \leq 0.0001$, as determined by the Wilcoxon rank sum test.

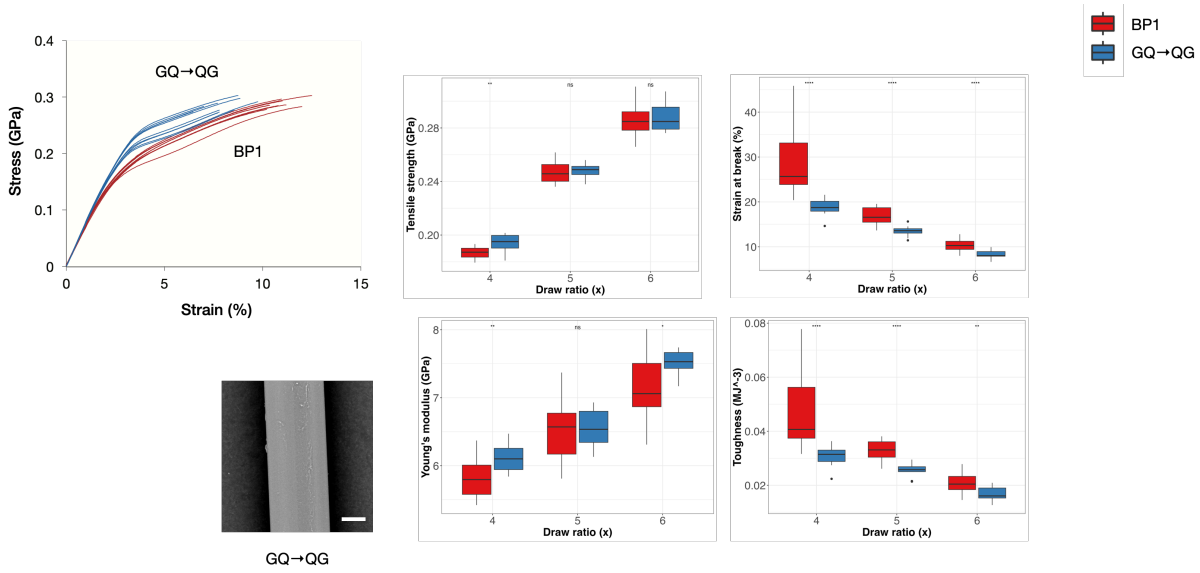

Figure 3-26. Stress-strain curve, SEM image, mechanical properties of the fibers with different drawing ratio of BP1 and BP1-CR-N (substitution pattern: GQ→QG).

The stress-strain curves and SEM images are 6 time drawing ratio of fiber. The number of test pieces in the stress-strain curve is 10. The scale bar in the SEM image is 20 μm. The marks above the box and whisker plots denote statistical significance. ns not significant, * $0.01 < p \leq 0.05$, ** $0.001 < p \leq 0.01$, *** $0.0001 < p \leq 0.001$, and **** $p \leq 0.0001$, as determined by the Wilcoxon rank sum test.

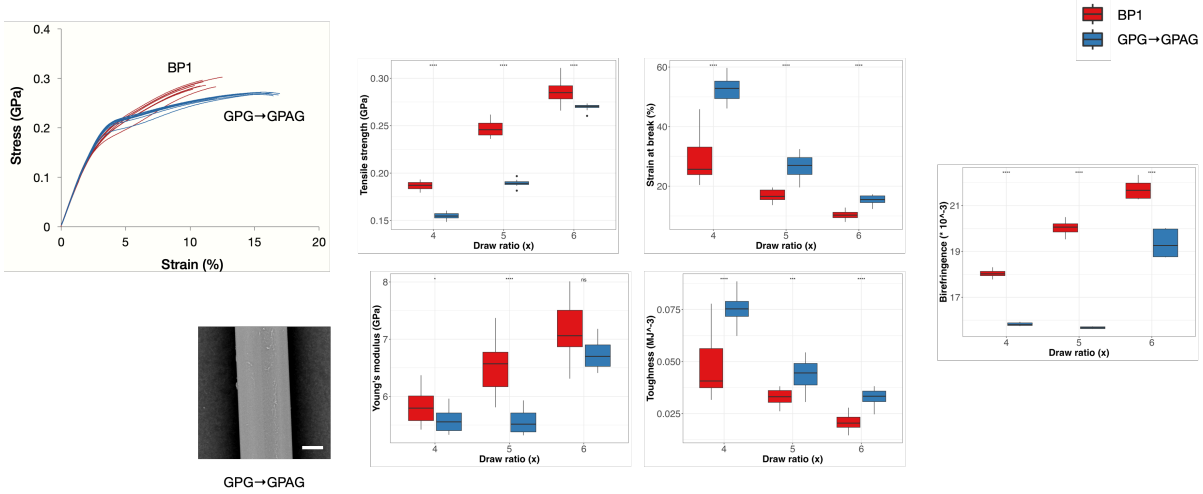

Figure 3-27. Stress-strain curve, SEM image, mechanical properties of the fibers with different drawing ratio of BP1 and BP1-CR-P (substitution pattern: GPG→GPAG).

The stress-strain curves and SEM images are 6 time drawing ratio of fiber. The number of test pieces in the stress-strain curve is 10. The scale bar in the SEM image is 20 μm. The marks above the box and whisker plots denote statistical significance. ns not significant, * $0.01 < p \leq 0.05$, ** $0.001 < p \leq 0.01$, *** $0.0001 < p \leq 0.001$, and **** $p \leq 0.0001$, as determined by the Wilcoxon rank sum test.

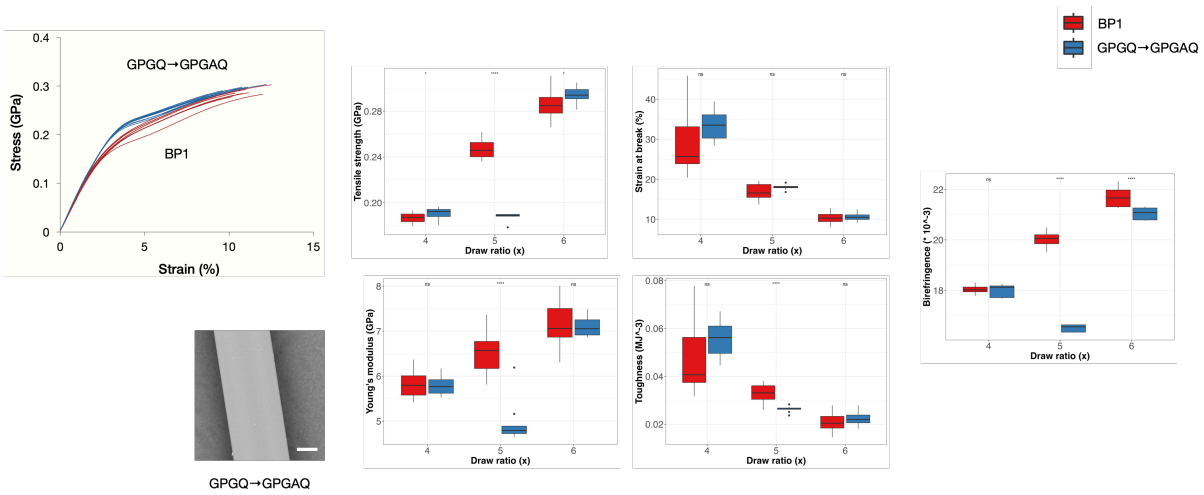

Figure 3-28. Stress-strain curve, SEM image, mechanical properties of the fibers with different drawing ratio of BP1 and BP1-SC-P (substitution pattern: GPGQ→GPGAQ).

The stress-strain curves and SEM images are 6 time drawing ratio of fiber. The number of test pieces in the stress-strain curve is 10. The scale bar in the SEM image is 20 μm. The marks above the box and whisker plots denote statistical significance. ns not significant, * $0.01 < p \leq 0.05$, ** $0.001 < p \leq 0.01$, *** $0.0001 < p \leq 0.001$, and **** $p \leq 0.0001$, as determined by the Wilcoxon rank sum test.

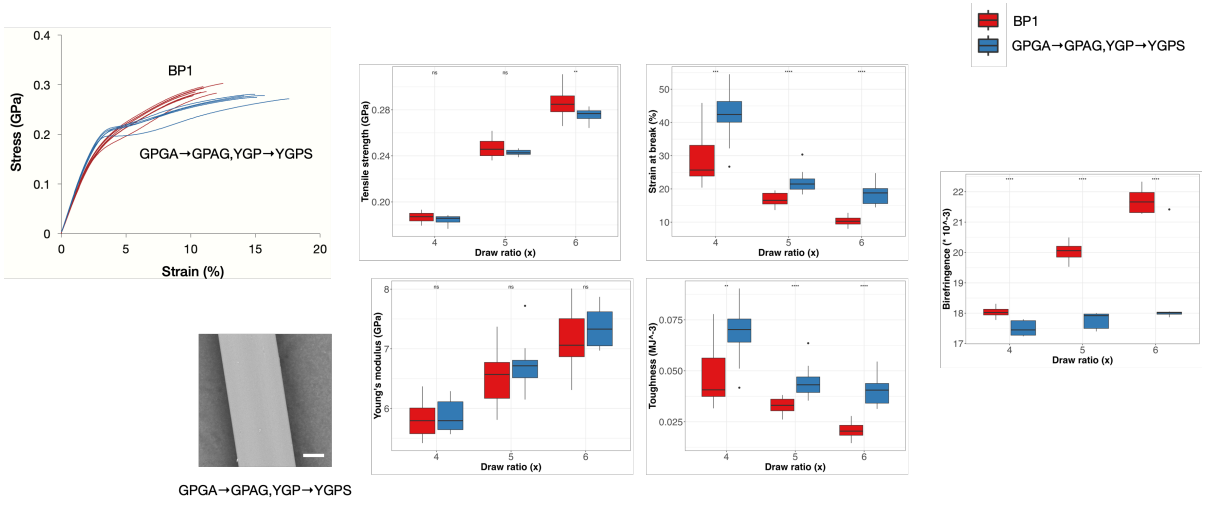

Figure 3-29. Stress-strain curve, SEM image, mechanical properties of the fibers with different drawing ratio of BP1 and BP1-SC-N (substitution pattern: GPGA→GPAG,YGP→YGPS).

The stress-strain curves and SEM images are 6 time drawing ratio of fiber. The number of test pieces in the stress-strain curve is 10. The scale bar in the SEM image is 20 μm. The marks above the box and whisker plots denote statistical significance. ns not significant, * $0.01 < p \leq 0.05$, ** $0.001 < p \leq 0.01$, *** $0.0001 < p \leq 0.001$, and **** $p \leq 0.0001$, as determined by the Wilcoxon rank sum test.

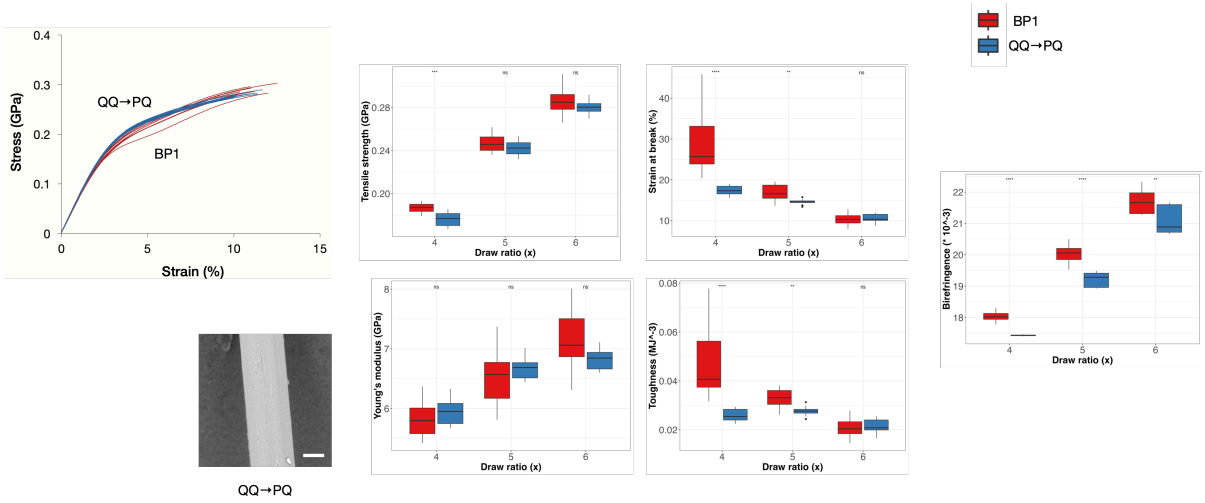

Figure 3-30. Stress-strain curve, SEM image, mechanical properties of the fibers with different drawing ratio of BP1 and BP1-TS_YM_N (substitution pattern: QQ→PQ).

The stress-strain curves and SEM images are 6 time drawing ratio of fiber. The number of test pieces in the stress-strain curve is 10. The scale bar in the SEM image is 20 μm. The marks above the box and whisker plots denote statistical significance. ns not significant, * $0.01 < p \leq 0.05$, ** $0.001 < p \leq 0.01$, *** $0.0001 < p \leq 0.001$, and **** $p \leq 0.0001$, as determined by the Wilcoxon rank sum test.

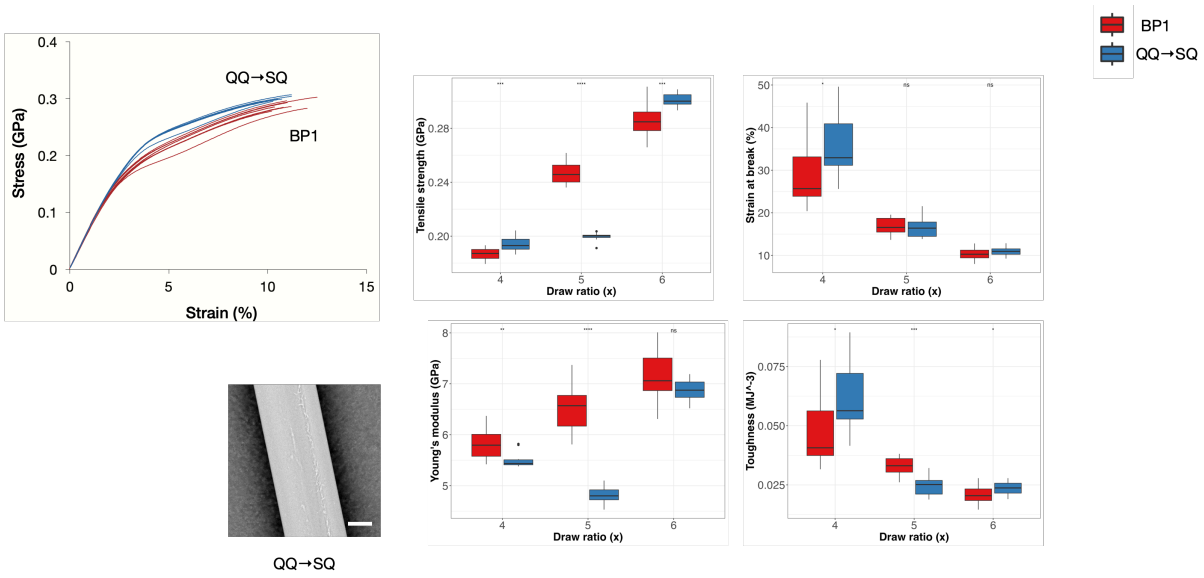

Figure 3-31. Stress-strain curve, SEM image, mechanical properties of the fibers with different drawing ratio of BP1 and BP1-CR-N2 (substitution pattern: QQ→SQ).

The stress-strain curves and SEM images are 6 time drawing ratio of fiber. The number of test pieces in the stress-strain curve is 10. The scale bar in the SEM image is 20 μm. The marks above the box and whisker plots denote statistical significance. ns not significant, * $0.01 < p \leq 0.05$, ** $0.001 < p \leq 0.01$, *** $0.0001 < p \leq 0.001$, and **** $p \leq 0.0001$, as determined by the Wilcoxon rank sum test.

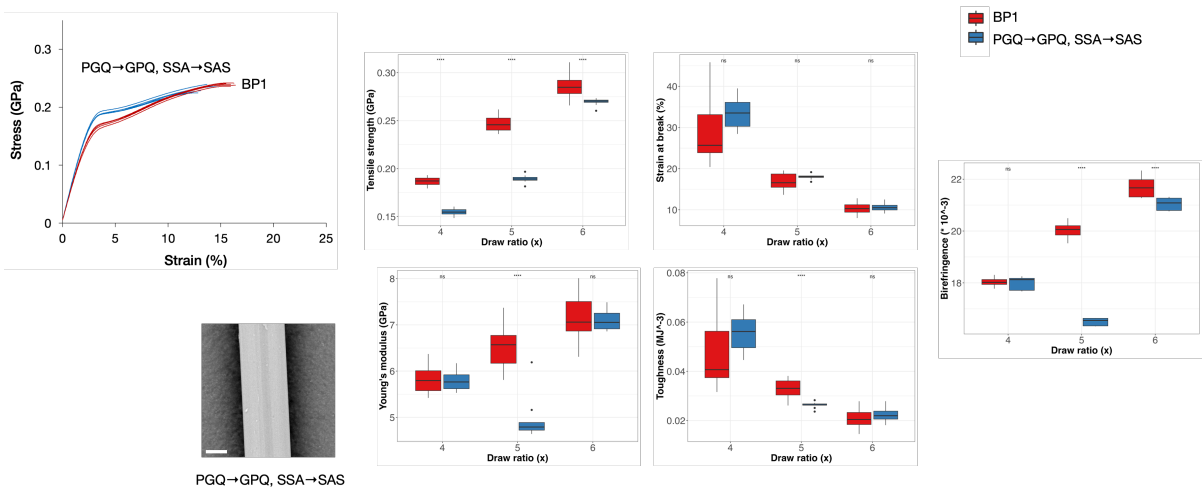

Figure 3-32. Stress-strain curve, SEM image and mechanical properties with different drawing ratio of BP1 and BP1-TS_YM_BR-N2 (substitution pattern: PGQ→GPQ, SSA→SAS).

The stress-strain curves are 5 time drawing ratio of fiber. The number of test pieces in the stress-strain curve is 10. The scale bar in the SEM image is 20 μm. The marks above the box and whisker plots denote statistical significance. ns not significant, * $0.01 < p \leq 0.05$, ** $0.001 < p \leq 0.01$, *** $0.0001 < p \leq 0.001$, and **** $p \leq 0.0001$, as determined by the Wilcoxon rank sum test.

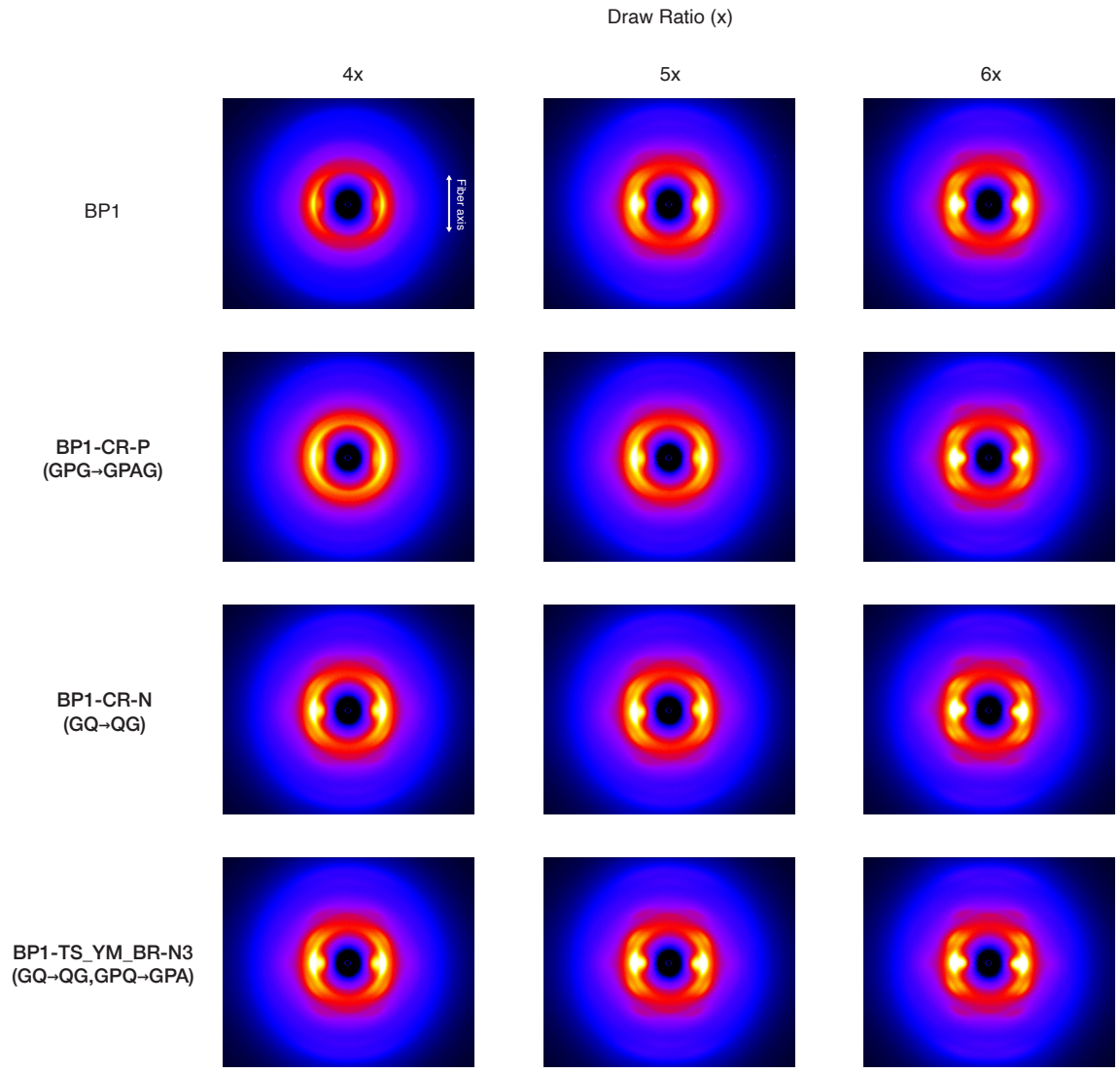

Figure 3-33. Two-dimensional WAXS profiles of the modified BP1.

The two-dimensional WAXS profiles of BP1 and BP1 mutants modified with the motifs predicted to affect the crystallinity. The axis of all profiles is the same as the top left profile.

Table 3-5. Crystallinity and orientation of the poly Alanine crystallites of the modified BP1.

Name	BP1			BP1-CR-P			BP1-CR-N			BP1-TS_YM_BR-N3		
Substitution pattern				GPG→GPAG			GQ→QG			GQ→QG,GPQ→GPA		
Draw ratio (x)	4	5	6	4	5	6	4	5	6	4	5	6
Crystallinity (%)	20.0	19.5	19.5	19.7	18.8	18.4	18.7	18.4	19.2	18.6	18.6	18.8
Orientation *a* (%)	78.8	83.0	85.4	75.7	81.5	86.3	83.5	83.5	86.6	83.2	85.1	86.3
Orientation *b* (%)	81.2	84.4	86.8	79.1	83.4	87.8	84.3	85.2	87.9	84.9	86.6	88.0
Orientation *c* (%)	ND	87.3	82.5	ND	ND	82.5	87.5	87.1	84.9	87.7	86.1	86.6

The crystallinity and the orientations of the crystallites in the fibers of BP1 and BP1 mutants. Draw ratio is the fiber's draw ratio.

Table 3-6. Boiled water shrinkage, shrinkage after drying, and total shrinkage.

Property	Motif	Substitution pattern	Positive / Negative effects in natural spidroins	Draw ratio (x)	n	Effects in recombinant artificial spider silk (%)		
						Boiled water shrinkage (%)	Shrinkage after drying (%)	Total shrinkage (%)
Control	-	-	-	4	5	45.5 ± 0.6	17.7 ± 2.2	63.2 ± 1.8
				5	6	53.6 ± 2.2	14.8 ± 1.4	68.4 ± 2.8
				6	2	58.0 ± 1.0	14.3 ± 1.4	72.4 ± 0.5
Tensile strength	AAAAASGP	AAAAAAGP → AAAAASGP AAAAAGQ → AAAAASGPQ	Positive	4	0	ND	ND	ND
				5	0	ND	ND	ND
				6	0	ND	ND	ND
	GPQ	GPGQQ → GPQGPQ	Negative	4	2	47.0 ± 0.4 ns	17.4 ± 0.5 ns	64.3 ± 0.0 ns
				5	3	51.4 ± 1.6 ns	15.6 ± 1.0 ns	66.9 ± 0.8 ns
				6	3	55.4 ± 0.8 *	13.4 ± 0.6 ns	68.8 ± 0.2 ns
		PGQ → GPQ SSA → SAS		4	1	48.0	14.3	62.3
				5	1	53.3	20.0	73.3
Young's modulus	PA	GPG → GPA	Positive	4	3	43.8 ± 0.7 ns	16.8 ± 0.4 ns	60.5 ± 0.7 ns
				5	3	48.7 ± 0.9 *	16.5 ± 0.7 ns	65.2 ± 0.5 ns
				6	3	55.0 ± 3.1 ns	13.6 ± 1.7 ns	68.5 ± 2.0 ns
	GPQ	GPGQQ → GPQGPQ		4	2	47.0 ± 0.4 ns	17.4 ± 0.5 ns	64.3 ± 0.0 ns
				5	3	51.4 ± 1.2 ns	15.6 ± 1.0 ns	66.9 ± 0.8 ns
				6	3	55.4 ± 0.8 *	13.4 ± 0.6 ns	68.8 ± 0.2 ns
		GQ → QG GPQ → GPA	Negative	4	3	45.1 ± 0.4 ns	25.7 ± 1.5 *	70.8 ± 1.3 *
				5	1	52.7	19.0	71.7
				6	2	57.9 ± 0.2 ns	18.5 ± 0.3 ns	76.4 ± 0.5 ns
	PQ	QQ → PQ		4	3	42.4 ± 1.0 *	17.0 ± 0.6 ns	59.4 ± 1.3 *
				5	3	47.2 ± 0.9 ***	14.3 ± 0.7 ns	61.6 ± 0.2 **
				6	3	53.8 ± 0.2 ns	13.1 ± 0.4 ns	66.9 ± 0.5 **
Strain at break	QGPSG	QGPY → QGPSGY	Positive	4	3	47.6 ± 1.2 ns	18.0 ± 1.2 ns	65.5 ± 0.7 *
				5	2	52.5 ± 1.1 ns	17.5 ± 2.6 ns	70.0 ± 1.4 ns
				6	3	59.5 ± 0.7 ns	14.9 ± 0.7 ns	74.3 ± 0.0 ns
	AAASA	AAAAA → AAASA	Negative	4	5	44.5 ± 2.2 ns	21.0 ± 2.9 ns	65.5 ± 0.7 *
				5	4	51.8 ± 2.4 ns	19.0 ± 2.3 *	70.8 ± 0.2 ns
				6	6	57.0 ± 0.7 ns	17.0 ± 0.8 ns	73.9 ± 0.6 ns
Toughness	PA	GPGA → GPAG	Positive	4	1	44.0	18.7	62.7
				5	0	ND	ND	ND
				6	0	ND	ND	ND
	GPGSQGP	GPGQQGP → GPGSQGP	Negative	4	3	43.9 ± 1.3 ns	18.2 ± 1.2 ns	62.1 ± 1.7 ns
				5	2	51.0 ± 0.4 *	17.0 ± 1.0 ns	68.0 ± 1.4 ns
				6	3	55.8 ± 1.0 ns	14.2 ± 0.4 ns	70.0 ± 0.7 *
Crystallinity	GPA	GPG → GPAG	Positive	4	2	37.5 ± 10.6 ns	21.7 ± 4.7 ns	59.2 ± 15.3 ns
				5	2	63.7 ± 9.0 ns	14.4 ± 5.2 ns	78.0 ± 3.8 ns
				6	3	56.7 ± 0.9 ns	16.0 ± 0.9 ns	72.6 ± 0.6 ns
	SQ	QQ → SQ	Negative	4	3	44.8 ± 0.2 ns	17.6 ± 1.2 ns	62.3 ± 1.0 ns
				5	3	49.7 ± 0.6 **	11.9 ± 0.2 **	61.6 ± 0.5 **
				6	3	55.1 ± 0.7 ns	13.5 ± 0.4 ns	68.7 ± 0.9 **
	GQ	GQ → QG		4	0	ND	ND	ND
				5	0	ND	ND	ND
				6	0	ND	ND	ND
Birefringence	SSA	SAA → SSA	Positive	4	ND	ND	ND	ND
				5	ND	ND	ND	ND
				6	ND	ND	ND	ND
	GPQ	PGQ → GPQ SSA → SAS	Negative	4	1	48.0	14.3	62.3
				5	1	53.3	20.0	73.3
Supercontraction	GPGA	GPGQ → GPGAQ	Positive	4	3	45.1 ± 0.7 ns	20.9 ± 0.7 *	66.0 ± 1.3 *
				5	2	51.7 ± 0.5 ns	17.9 ± 0.2 **	69.5 ± 0.3 ns
				6	2	56.8 ± 0.7 ns	15.7 ± 0.5 ns	72.5 ± 1.1 ns
		GPGA → GPAG		4	1	44.0	18.7	62.7
				5	0	ND	ND	ND
				6	0	ND	ND	ND
	YGPS	GPGA → GPAG YGP → YGPS	Negative	4	0	ND	ND	ND
				5	0	ND	ND	ND
				6	0	ND	ND	ND

For the number of N means the number of the test pieces which was able to measure the length in the test. ND means no data. The marks next to the values in the boiled water shrinkage, shrinkage after drying, and total shrinkage columns are statistically significant. ns not significant, * $0.01 < p \leq 0.05$, ** $0.001 < p \leq 0.01$, *** $0.0001 < p \leq 0.001$, and **** $p \leq 0.0001$, as determined by the Student's *t*-test. ND in the column n means we cannot conduct experiments due to lack of the fibers. 0 in the column n means we cannot measure the length because the fiber samples broke in the test.

Table 3-7. Mechanical properties and shrinkage after being immersed in hot water of fiber with the various drawing ratios of SQ/PQ motif substituted BP1.

motif	Draw ratio (x)	Tensile strength (GPa)	Strain at break (%)	Young's modulus (GPa)	Toughness (GJ * m-3)	No. of shrinkage tests	Boiled water shrinkage (%)	Shrinkage after drying (%)	Total shrinkage (%)
QQ (BP1)	4 N = 20	0.187 ± 0.004	29.3 ± 7.7	5.82 ± 0.27	0.048 ± 0.014	6	47.0 ± 1.7	16.6 ± 2.2	62.1 ± 1.3
	5 N = 20	0.247 ± 0.008	17.0 ± 2.0	6.53 ± 0.45	0.033 ± 0.004	6	54.5 ± 1.2	15.0 ± 1.4	69.9 ± 2.0
	6 N = 20	0.286 ± 0.011	10.3 ± 1.2	7.12 ± 0.51	0.021 ± 0.003	6	58.8 ± 1.2	14.3 ± 1.4	72.4 ± 0.5
SQ (BP1-CR-N2)	4 N = 10	0.194 ± 0.006	35.8 ± 7.6	5.51 ± 0.16	0.062 ± 0.015	3	44.8 ± 0.2	17.6 ± 1.2	62.3 ± 1.0
	5 N = 10	0.199 ± 0.003	16.5 ± 2.4	4.81 ± 0.16	0.025 ± 0.004	3	49.7 ± 0.6	11.9 ± 0.2	61.6 ± 0.5
	6 N = 10	0.301 ± 0.005	11.0 ± 1.1	6.87 ± 0.21	0.024 ± 0.003	3	55.1 ± 0.7	13.5 ± 0.4	68.7 ± 0.9
PQ (BP1-TS_YM_N)	4 N = 10	0.176 ± 0.007	17.4 ± 1.1	5.95 ± 0.22	0.026 ± 0.003	3	42.4 ± 1.0	17.0 ± 0.6	59.4 ± 1.3
	5 N = 10	0.242 ± 0.007	14.6 ± 0.7	6.68 ± 0.20	0.028 ± 0.002	3	47.2 ± 0.9	14.3 ± 0.7	61.6 ± 0.2
	6 N = 10	0.280 ± 0.006	10.6 ± 1.0	6.83 ± 0.19	0.022 ± 0.003	3	53.8 ± 0.2	13.1 ± 0.3	66.9 ± 0.5

For the number of N means the number of the test pieces which was able to measure the length in the test. ND means no data. The marks next to the values in the boiled water shrinkage, shrinkage after drying, and total shrinkage columns are statistically significant. ns not significant, * $0.01 < p \leq 0.05$, ** $0.001 < p \leq 0.01$, *** $0.0001 < p \leq 0.001$, and **** $p \leq 0.0001$, as determined by the Student's *t*-test. ND in the column n means we cannot conduct experiments due to lack of the fibers. 0 in column n means we cannot measure the length because the fiber samples broke in the test.

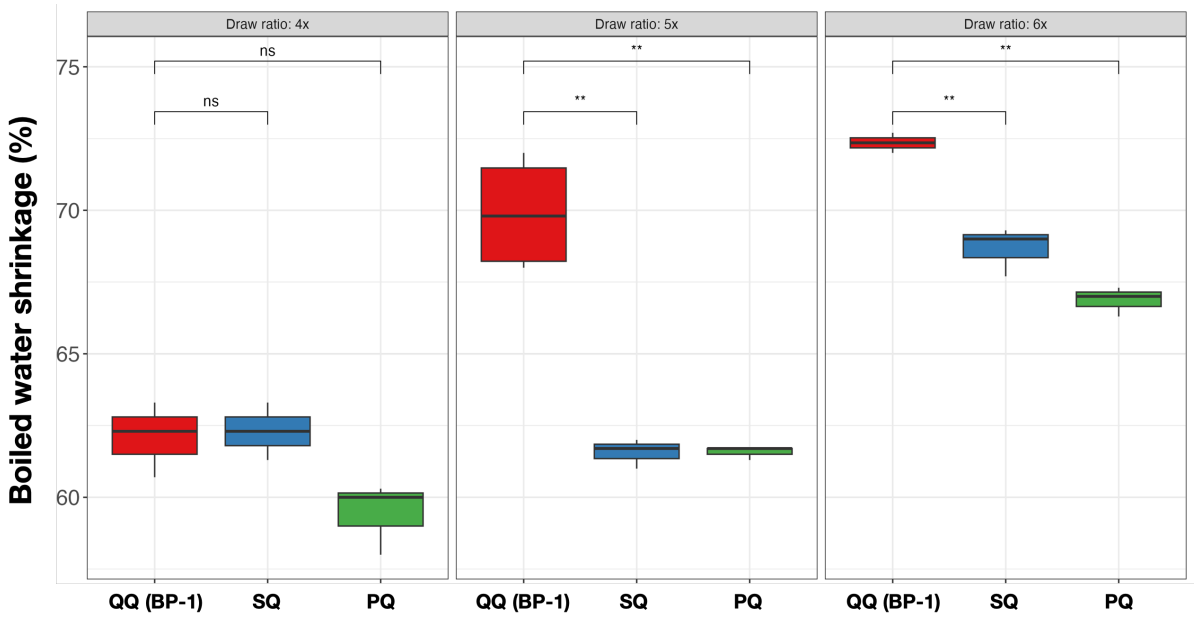

Figure 3-34. Comparison of total shrinkage rate of QQ (BP1-) to PQ (BP1-TS_YM_N), SQ (BP1-CR-N2) motif substitution.

Each box represents the drawing ratio of the fibers. The marks above the box and whisker plots denote statistical significance. ns not significant, * $0.01 < p \leq 0.05$, ** $0.0001 < p \leq 0.01$, *** $0.001 < p \leq 0.001$, and **** $p \leq 0.0001$, as determined by the Student's *t*-test.

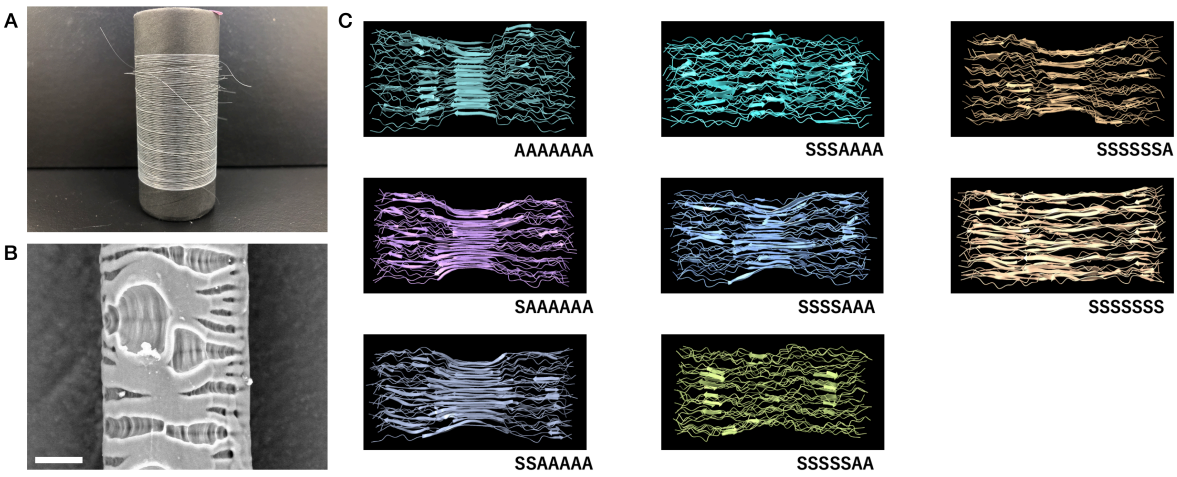

Figure 3-35. SAA→SSA substitution makes it impossible to form fibers in the artificial spider silk spinning system.

A) The SAA→SSA substituted mutant BP1-BR-P dissolved in the washing bath (water, RT), therefore the photo of the bobbin are fibers after the MeOH coagulation bath. B) SEM image of the fiber of SAA →SSA substituted spidroin. The scale bar in the SEM image is 20 μm C) Molecular dynamics simulation of the repetitive region of BP1 with polyalanine x7 (AAAAAAA), where an alanine is replaced by serine one by one. suggests SSSAAAA motif prevents to form of a regular poly-Ala anti-parallel β-sheet. The arrows indicate an anti-parallel β-sheet.

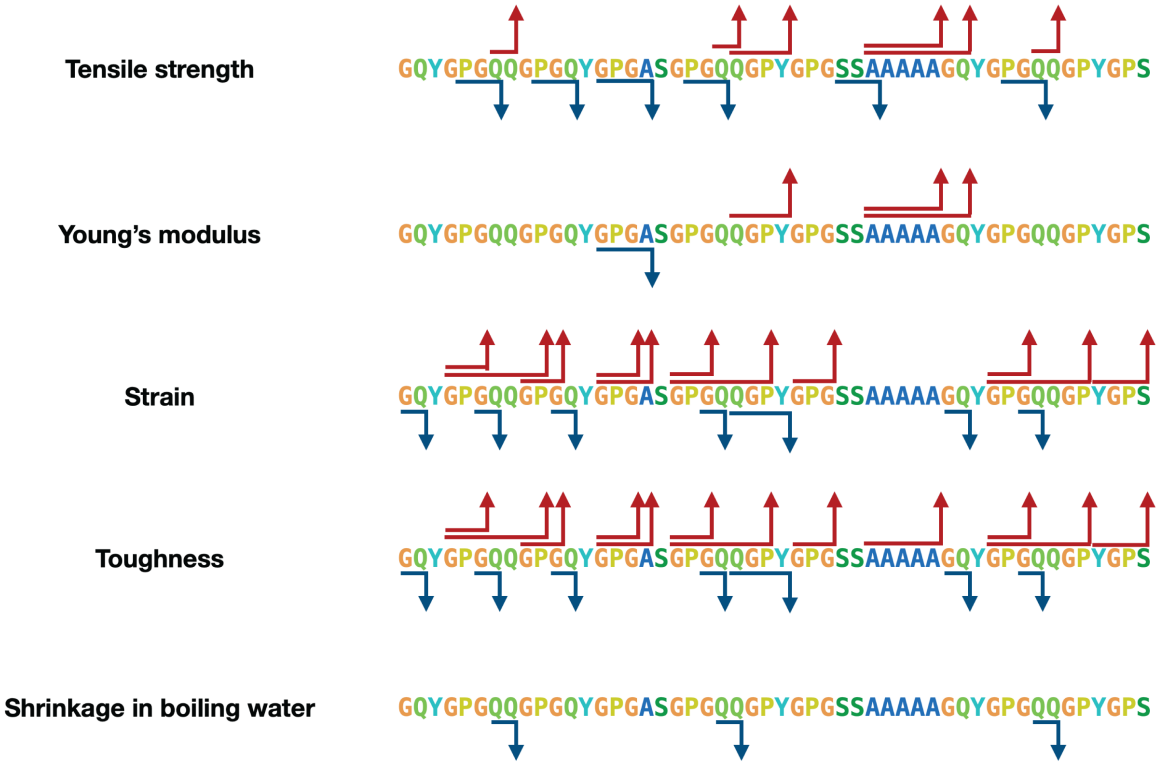

Figure 3-36. The location of the substitution and its effect on the fiber properties.

The sequence represents the BP1 repeat region. The effect of the substitutions on each property is indicated by red and blue arrows, where red indicates a positive effect and blue indicates a negative effect.

3.4 Discussion

In this study, we modified BP1 (MaSp2) with motifs correlated with physical properties, which were identified through the analysis of spidroins collected from 1,000 spider species (Arakawa *et al.* 2022) and observed the effects on the mechanical properties of artificial spider silk fibers. This approach allowed us to investigate the relationship between the primary sequence motifs of spidroins and the mechanical properties of the fibers, a topic of considerable interest due to the complex composition of natural spider silk, which includes multiple spidroins such as MaSp1, MaSp2, MaSp3, and other non-spidroin component, spider silk-constituting elements (SpiCEs) (Kono *et al.* 2019, 2021a). The complexity of natural spider silk, which contains multiple spidroins and SpiCEs, plays a significant role in its mechanical properties (Kono *et al.* 2021a), raising questions about the feasibility of replicating these properties using artificial fibers composed of a single spidroin. However, the observation of the effects of single spidroin motifs on the mechanical properties in this experiment confirms the correlation between the primary sequences of spidroins and their mechanical properties.

The series of experiments has demonstrated the potential to control the mechanical properties of artificial spider silk using motifs derived from natural spidroins. While some properties were easier to manipulate, others presented challenges. For example, while the effects of motifs on tensile strength were as predicted for both positive and negative effects, strain at break showed an opposite trend. Positive and negative predicted effects on toughness were both found to increase it, potentially due to the influence of strain dependence on modifications across the entire repeat region, as suggested in Figure 3-19. Tensile stress, which is influenced by the crystalline region and its vicinity, appears to be more easily controlled. Interestingly, substitutions of both positive (QGPY→QGPSGY) and negative (AAAAA→AAASA) motifs increased tensile strength and birefringence (Figure 3-22 and Figure 3-23). This result was not expected, but the birefringence of the fibers are higher than the control, which is consistent with reports that tensile strength and orientation order are correlated in natural dragline silk (Du *et al.* 2006; Madurga *et al.* 2015). In the natural dragline silk, these motifs may help orient crystalline regions, and it may affect the strain at break in the natural dragline silk because the orientation of the crystallites is correlated with the strain (Madurga *et al.* 2015). The motif substitutions in BP1 were introduced with care to maintain the overall amino-acid composition, and each replacement was chosen for its close sequence similarity to the original motif. Nevertheless, unintended side-chain interactions or local changes in secondary structure cannot be ruled out, and these unforeseen effects may help explain the discrepancies between motif behavior in natural spider silk and in the artificial fibers.

As shown in Figure 3-19, the experiment revealed correlations between the locations of motif substitutions and insertions and the affected mechanical properties. For example, the strength and Young's modulus of the dragline silk were found to have influence from alterations in or around

crystalline regions. This observation aligns with previous studies that have identified crystalline regions as the primary source of the Young's modulus and tensile strength of dragline silk (Madurga *et al.* 2015; Johansson and Rising 2021). On the other hand, strain at the break was mainly influenced by modifications in amorphous regions. Toughness showed changes with modifications in both crystalline and amorphous regions, suggesting that different mechanical properties can be influenced by modifying different regions of the fiber.

Substitution of SAA to SSA motifs, which positively affect birefringence, resulted in fiber dissolution during extension in the water bath, preventing fiber formation. Prior research indicates a correlation between orientation and supercontraction (Pérez-Rigueiro *et al.* 2021). This may be associated with the dissolution occurring in the water bath and the birefringence, which represents the orientation of the molecules within the fiber. This may be due to differences in the spinning mechanisms between natural and artificial silk or to specific issues related to the modified protein sequence. Molecular dynamics simulations suggested that β-sheets may be slightly distorted when serine is present three times compared to twice before a polyalanine sequence, indicating that certain modifications can render artificial spinning infeasible.

As previously discussed, the mechanical properties of the artificial spider silks are contingent upon the structural properties, including the crystallinity and orientation of the crystalline and amorphous regions. The artificial spinning process employed in this work does not fully recapitulate the natural spinning conditions, and therefore the approach of this work is inherently limited in this respect. This is especially true for the highly lowered strain at break in comparison to natural silks and may be the reason for discrepancies of the current results from prediction, as in motifs predicted to positively or negatively influence toughness actually resulted in an increase (Table 3-2). On the other hand, the observation in Figure 3-19 that the location of the modification is related to the modified properties, and that the modification around the crystalline region changes tensile strength as well as birefringence suggests that the sequence motifs somewhat affect the structure of the spidroin even in this artificial setting. This extends to the alterations to the amorphous region impacting on the toughness and strain at break, which may also influence the secondary structure of the spidroin.

Interestingly, motifs with positive/negative effects on crystallinity were found to increase toughness, consistent with the analysis of spidroins from 1,000 spider species, which showed a high correlation between crystallinity and toughness (Arakawa *et al.* 2022). However, as shown in Table 3-5, the crystallinity and the orientation of the crystallites of the modified proteins did not differ from the control in the artificial spider silk. In the natural spider silk, the major ampullate silk has hierarchical structures that are bundles of nanofibrils (Lin *et al.* 2017), whereas the artificial spider silk produced in this study does not have a hierarchical structure because the mini-spidroins are dissolved in the organic solvent and coagulated in the methanol. In the natural spinning process used by spiders, the crystallization of poly-alanine anti-parallel β-sheets is

induced by the shear force in the spinning duct (Knight and Vollrath 2002; Chen *et al.* 2024). However, in the artificial spinning processes using organic solvent and methanol coagulation bath, the crystallization of the poly-alanine occurs immediately in the coagulation bath, resulting in the fiber lacking the hierarchical structure (Rising and Johansson 2015; Koeppel and Holland 2017). The structural difference is therefore presumably the consequence of the difference in spinning procedures in the natural and artificial spider silk.

Formic acid was employed in the study as the solvent of artificial spidroins as it is commonly used in the investigation of regenerated silk, and the effects of this solvent has been discussed in previous works. Suzuki *et al*. observed that the Gly-Pro-Gly-X motif of MaSp2 forms a type II β-turn structure in formic acid, which is analogous to that observed in MaSp2 present in silk fibers (Suzuki *et al.* 2022). Furthermore, it was observed that the mobility of the glycine-rich region is lower than that of the polyalanine region, which provides insight into the underlying reason for the stability of MaSp2 in formic acid (Suzuki *et al.* 2022). Furthermore, MaSp2 film prepared with formic acid forms a β-sheet structure, which is not observed in the DMSO-prepared sponge or the HFIP-prepared film (Suzuki *et al.* 2022). This observation indicates that the secondary structure of MaSp2 in formic acid may possess common structural properties with the natural MaSp2 aqueous solution in support of the sequence-property relationships observed in the current study. However, there are also notable differences between the natural spinning system and the artificial system utilizing formic acid and methanol, especially in terms of the formation of hierarchical structures. In the artificial spinning system employed in the study, the spidroin is dissolved in formic acid and subsequently coagulated and crystallized through desolvation. The desolvation process was observed to occur immediately upon extrusion of the spidroin into the coagulation bath, resulting in the immediate crystallization of the poly-alanine. In contrast, the natural spinning system utilized by spiders involves the dissolution of the spidroin in an aqueous solution, where it undergoes fibrillation due to the dimerization of the N-terminal domain, which is activated by a pH gradient (Kronqvist *et al.* 2014; Malay *et al.* 2020). In the spinning system, the formation of nanofibril bundles within the fiber is achieved through the rapid self-assembly of a nanofibril network in mild acidification. The resulting hierarchical structure, comprising the nanofibril network, endows the major ampullate silk with its distinctive mechanical properties (Porter, Guan and Vollrath 2013; Malay *et al.* 2022; Watanabe and Arakawa 2023). This discrepancy may be the reason why the sequence property relationships observed in natural spider silk could not be fully replicated, particularly those related to the strain at break. To enhance the reproducibility of the motif-property relationships observed in the natural spider silk, the utilization of the biomimetic spinning system (Andersson *et al.* 2017; Malay *et al.* 2020; Greco *et al.* 2021; Saric and Scheibel 2023; Chen *et al.* 2024) would be a reasonable future direction to recapitulate the natural spinning process.

In this study, the substitution of the di-glutamine (QQ) motif with serine-glutamine (SQ) and

proline-glutamine (PQ) in our experiments measuring boiled water shrinkage has demonstrated a marked decrease in the extent of contraction upon immersion and subsequent drying (see Table 3-7 and Figure 3-34). Notably, the QQ motif, which is prevalent in MaSp2, is linked to the GP sequence within the characteristic GPGXX motif of MaSp2 (Gatesy *et al.* 2001; Rising *et al.* 2007; Malay, Arakawa and Numata 2017). It is hypothesized that the QQ motif plays a role in maintaining the hierarchical structure of major ampullate silk although its function remains to be elucidated (Malay, Arakawa and Numata 2017; Arguelles *et al.* 2023). The observed reduction in shrinkage upon substitution suggests a possible interaction of these motifs with water and thermally induced fiber deformation, potentially akin to the supercontraction phenomenon which is induced by water immersion (Work 1977, 1981). Previous research on supercontraction has identified the MaSp2 and the proline-rich GPGXX motif as the primary contributor to supercontraction, associated with torsional fiber deformation (Liu *et al.* 2008, 2019; Savage and Gosline 2008b; Guan, Vollrath and Porter 2011). Our results implicate the QQ motif in supercontraction alongside the GPG motif. Nonetheless, given the lack of supercontraction data specific to the SQ and PQ motifs in our previous research, further investigation is required to unravel the underlying supercontraction mechanisms and the individual contributions of the QQ, SQ, and PQ motifs.

The experiments did not show simultaneous improvements in strength and elongation, suggesting a possible trade-off between these properties. Overcoming this trade-off would be highly beneficial for industrial applications and would require technologies capable of controlling both properties simultaneously. As shown in Figure 3-19, the separate control of strength and elongation by different regions suggests the possibility of using different motifs with distinct effects simultaneously as a potential modification strategy.

3.5. Conclusions

This study describes the influence of motifs in the primary sequence of spidroin on the mechanical properties of artificial spider silk. Our results confirm that specific motifs extracted from a comprehensive analysis of 1,000 spider species significantly modify mechanical properties such as tensile strength. In particular, motifs identified as influencing tensile strength do so in both positive and negative ways. However, manipulating strain at break proved to be more challenging, highlighting the complex interaction between primary sequence and mechanical properties. In addition, our results confirm the role of motif placement within the primary sequence in achieving the desired changes, consistent with previous discussions. Our study suggests that the di-glutamine motif may contribute to response to water and temperature changes of the fibers, confirming our previous analysis of the natural spider silk (Arakawa *et al.* 2022). This would add a link between the primary sequence and the supercontraction phenomena observed in dragline silk, in addition to the previous findings for proline in MaSp2 (Liu *et al.* 2008, 2019; Boutry and Blackledge 2010;

Guan, Vollrath and Porter 2011) -GXG- in the MaSp1 (Guan, Vollrath and Porter 2011), and hydroxyproline (Craig *et al.* 2019). These results confirm the intrinsic relationship between the primary sequence and the mechanical properties of artificial spider silk and suggest promising approaches for future applications in the emerging artificial silk industry. Continued exploration of motif combinations and refined control of mechanical properties promise to advance artificial spider silk.

Chapter 4
Concluding remarks

4.1. Progress and challenges in controlling physical properties of artificial spider silk

This thesis aimed to control the physical properties of artificial spider silk using sequence–property relationships derived from natural spider silk. A multi-omics analysis of natural MA- and MI-silk established these relationships and then verified with artificial spider silks (Nakamura *et al.* 2023). Building on these results, motifs from a database of 1,000 spider silk transcriptomes were substituted via protein design to systematically alter physical properties. As a result, substituting motifs positively or negatively correlated with tensile strength successfully altered the property of the artificial silk (Nakamura *et al.* 2024). Overall, these findings confirm the feasibility of engineering artificial spider silks by applying the sequence–property relationships of natural spider silk.

In Chapter 2, the mechanical, supercontraction, and structural properties of MA- and MI-silk were analyzed. Proteomic analysis revealed that MI-silk does not contain MaSp2. Artificial spider silk composed of MaSp1, MaSp2, and MiSp showed clear differences in supercontraction: MiSp-based fibers contracted the least, whereas MaSp2-based fibers showed the greatest contraction. These findings suggest that the presence of MaSp2 spidroin largely explains the difference in how MA- and MI-silks respond to water immersion. Furthermore, reconstructing these differences in artificial spider silk confirms that MaSp2 strongly influences supercontraction.

Differences were also observed in the mechanical properties of MaSp1-, MaSp2-, and MiSp-based artificial spider silk. MaSp1-based fibers exhibited the highest tensile strength and the lowest strain at break, while MaSp2-based fibers showed the opposite pattern. MiSp-based fibers had a high strain at break similar to MaSp2, but a higher tensile strength than MaSp2. These observations demonstrate that variations in the protein sequence strongly affect the mechanical properties of artificial spider silk.

MaSp2 is thought to promote the supercontraction of MA-silk because its repetitive region contains the GPGXX motif, which introduces a high proportion of proline residues; proline is known to disrupt secondary structure within glycine-rich peptide sequences (Work and Young 1987; Savage and Gosline 2008b; Liu *et al.* 2008). The study presented in this thesis is the first to show that MI-silk lacks MaSp2 whereas MA-silk contains it, providing strong evidence that MaSp2 drives the supercontraction observed in MA-silk. Furthermore, the study revealed that MI-silks from both *Araneus* and *Trichonephila* contain MaSp1, indicating that MaSp1—rather than other MaSp paralogs—is the basic component of ampullate silks, consistent with suggestions from

previous studies (Blackledge *et al.* 2009; Blamires, Blackledge and Tso 2017).

In Chapter 3, the MaSp2 mini-spidroin was modified by substituting motifs that correlate with specific mechanical properties. These motifs were extracted from the spidroins of 1,000 spider species; 17 motifs were identified that correlate with seven physical properties (tensile strength, Young's modulus, strain at break, toughness, crystallinity, birefringence, and supercontraction). Each motif was introduced (or removed) in a MaSp2 mini-spidroin called BP1, and the recombinant constructs were then expressed in bacteria. Using identical artificial spinning conditions, the resulting fibers were created and evaluated.

Consistent with the correlation data, motifs positively correlated with tensile strength increased tensile strength of the fiber, whereas those negatively correlated decreased it. Interestingly, both positively and negatively correlated motifs boosted toughness to some degree. However, the expected directional changes in strain at break were not observed: motifs positively correlated with strain at break actually decreased it, and the motif negatively correlated with strain at break produced no significant effect. We hypothesize that these unexpected results stem from structural discrepancies in the fibers, which likely arise from differences between natural and artificial spinning systems.

Because the artificial spinning system uses organic solvents, spidroin is denatured in solution; therefore, the resulting fibers likely lack the hierarchical structure found in natural spider silk. This structural discrepancy may explain inconsistencies between the predicted and observed effects of the motifs. Despite these limitations, our results confirm that sequence motifs extracted from natural spider silks can be used to modulate the mechanical properties of artificial spider silk.

To date, many efforts have been made to tailor the properties of artificial spider silk. Teulé *et al.* (2007) designed putative spidroin variants composed of alternating GPGGX and poly-alanine motifs and showed that the identity of the fifth residue (X) strongly influences fiber elasticity. Xia *et al.* (2010) created a 284.9 kDa recombinant spidroin and obtained fibers with markedly higher tensile strength. Heidebrecht *et al.* (2015), produced a recombinant ADF-4 analogue with an extended amorphous domain that achieved toughness comparable to natural spider silk. Greco *et al.* (2021) modulated supercontraction by substituting tyrosine residues in the amorphous region. Each of these studies successfully tuned a single mechanical attribute. In contrast, the work presented in this thesis is the first to manipulate multiple physical properties of artificial spider silk by leveraging sequence–property relationships extracted from a comprehensive catalogue of natural spidroin sequences and their associated physical properties of fiber.

In Chapter 3, we showed that the position of a motif substitution dictates which mechanical property is altered. Changes in the amorphous region affected strain at break and toughness, whereas changes in the crystalline region altered tensile strength. This pattern follows earlier studies: Teulé *et al.* (2007) found that replacing the X residue in the amorphous-region GPGGX

motif modulates elasticity, and Hu *et al.* (2024) reported that increasing the length of the crystalline region improves the tensile strength of artificial spider silk. Tyrosine substitutions in amorphous segments have likewise been shown to modify supercontraction (Greco *et al.* 2021), a finding that aligns with our own results, where the substitution was also directed at the amorphous region. Although our mutants lacked tyrosine substitutions, replacing the di-glutamine motif in the amorphous region reduced shrinkage in boiling water. Together, these studies reinforce the connection between the location of a substitution and the mechanical property it influences.

4.2. Future perspectives

In the studies presented in this thesis, I successfully established a protein sequence design methodology to control the mechanical properties of artificial spider silk by using sequence–property relationships extracted from natural spider silk. Although the feasibility of this methodology was demonstrated, several issues remain for future work. First, as discussed in Chapter 3, there are inconsistencies in the effects of motifs between natural and artificial spider silk. In addition, there may be a threshold between proteins that are processable and those that are not. For instance, as seen with the SAA→SSA substitution, there is a boundary that critically affects fiber-forming ability. Furthermore, the effects of combining multiple motifs have not yet been verified.

In Chapter 3, while motifs positively and negatively correlated with tensile strength were able to control that property in artificial spider silk, motifs correlated with strain at break did not produce the intended results. As discussed in the chapter, the significant differences between natural and artificial spinning systems, particularly in the resulting fiber structures, may be the cause of this discrepancy. To confirm this hypothesis, the effects of these motifs should be tested using a biomimetic spinning system. Unlike artificial spinning, which denatures spidroins, biomimetic spinning preserves them and leverages fibrillation driven by the NTD and CTD domains. This process produces fibers with hierarchical structures. Comparing the mechanical properties of motif-substituted mutants under both systems would therefore provide valuable confirmation.

We also observed that the SAA→SSA-substituted mutant was unable to form fibers using the artificial spinning system. The fiber dissolved in the water-filled washing bath after coagulation. Molecular dynamics simulations suggest that increasing the number of serine residues immediately before the poly-alanine region may have prevented the formation of antiparallel β-sheets. This observation implies that certain modifications can hinder fiber formation during spinning. Consequently, when designing or altering protein sequences, the boundary between structural and non-structural proteins must be considered. Identifying and understanding this boundary and the limitations of structural proteins will be essential for designing artificial structural proteins more freely.

Finally, in this thesis, the combined effects of motifs correlated with different mechanical properties were not examined. To control multiple physical properties, it will be necessary to combine the motif substitutions identified in this study. For instance, using motifs that increase tensile strength alongside those that increase strain at break could potentially enhance both properties, though there may be conflicts between motifs. Therefore, further investigation into the relationships among multiple motifs is warranted for effective protein sequence design.

Addressing these outstanding issues will improve the design methodology for structural proteins, paving the way for future industrial applications of such designs.

References

Akkermans RLC, Spenley NA, Robertson SH. COMPASS III: automated fitting workflows and extension to ionic liquids. *Mol Simul* 2021;**47**:540–551.

Andersen SO. Amino acid composition of spider silks. *Comp Biochem Physiol* 1970;**35**:705–711.

Andersson M, Chen G, Otikovs M *et al.* Carbonic anhydrase generates CO_2 and H^+ that drive spider silk formation via opposite effects on the terminal domains. Petsko GA (ed.). *PLoS Biol* 2014;**12**:e1001921.

Andersson M, Jia Q, Abella A *et al.* Biomimetic spinning of artificial spider silk from a chimeric minispidroin. *Nat Chem Biol* 2017;**13**:262–264.

Andrady AL. Microplastics in the marine environment. *Mar Pollut Bull* 2011;**62**:1596–1605.

Arakawa K, Kono N, Malay AD *et al.* 1000 spider silkomes: Linking sequences to silk physical properties. *Sci Adv* 2022;**8**:eabo6043.

Arakawa K, Mori M, Kono N *et al.* Proteomic evidence for the silk fibroin genes of spider mites (Order Trombidiformes: Family Tetranychidae). *J Proteomics* 2021;**239**:104195.

Arguelles J, Baker RH, Perez-Rigueiro J *et al.* Relating spidroin motif prevalence and periodicity to the mechanical properties of major ampullate spider silks. *J Comp Physiol B* 2023;**193**:25–36.

Asakura T, Matsuda H, Naito A *et al.* Formylation of recombinant spider silk in formic acid and wet spinning studied using nuclear magnetic resonance and infrared spectroscopies. *ACS Biomater Sci Eng* 2022a;**8**:2390–2402.

Asakura T, Matsuda H, Naito A *et al.* Recombinant spider silk fiber with high dimensional stability in water and its NMR characterization. *Molecules* 2022b;**27**:8479.

Askarieh G, Hedhammar M, Nordling K *et al.* Self-assembly of spider silk proteins is controlled by a pH-sensitive relay. *Nature* 2010;**465**:236–238.

Belzagui F, Crespi M, Álvarez A *et al.* Microplastics' emissions: Microfibers' detachment from textile garments. *Environ Pollut* 2019;**248**:1028–1035.

Bernot JP, Owen CL, Wolfe JM *et al.* Major revisions in pancrustacean phylogeny and evidence of sensitivity to taxon sampling. *Mol Biol Evol* 2023;**40**:msad175.

Blackledge TA, Hayashi CY. Silken toolkits: biomechanics of silk fibers spun by the orb web spider *Argiope argentata* (Fabricius 1775). *J Exp Biol* 2006;**209**:2452–2461.

Blackledge TA, Pérez-Rigueiro J, Plaza GR *et al.* Sequential origin in the high performance properties

of orb spider dragline silk. *Sci Rep* 2012;**2**:782.

Blackledge TA, Scharff N, Coddington JA *et al.* Reconstructing web evolution and spider diversification in the molecular era. *Proc Natl Acad Sci U S A* 2009;**106**:5229–5234.

Blamires SJ, Blackledge TA, Tso IM. Physicochemical property variation in spider silk: ecology, evolution, and synthetic production. *Annu Rev Entomol* 2017;**62**:443–460.

Boutry C, Blackledge TA. Evolution of supercontraction in spider silk: structure–function relationship from tarantulas to orb-weavers. *J Exp Biol* 2010;**213**:3505–3514.

Boutry C, Blackledge TA. Wet webs work better: Humidity, supercontraction and the performance of spider orb webs. *J Exp Biol* 2013;**216**:3606–3610.

Bowen CH, Dai B, Sargent CJ *et al.* Recombinant spidroins fully replicate primary mechanical properties of natural spider silk. *Biomacromolecules* 2018;**19**:3853–3860.

Bryksin AV, Matsumura I. Overlap extension PCR cloning: a simple and reliable way to create recombinant plasmids. *BioTechniques* 2010;**48**:463.

Chamas A, Moon H, Zheng J *et al.* Degradation rates of plastics in the environment. *ACS Sustain Chem Eng* 2020;**8**:3494–3511.

Chaw RC, Correa-Garhwal SM, Clarke TH *et al.* Proteomic evidence for components of spider silk synthesis from black widow silk glands and fibers. *J Proteome Res* 2015;**14**:4223–4231.

Chen J, Tsuchida A, Malay AD *et al.* Replicating shear-mediated self-assembly of spider silk through microfluidics. *Nat Commun* 2024;**15**:527.

Cohen N, Levin M, Eisenbach CD. On the Origin of Supercontraction in Spider Silk. *Biomacromolecules* 2021;**22**:993–1000.

Colgin MA, Lewis RV. Spider minor ampullate silk proteins contain new repetitive sequences and highly conserved non-silk-like “spacer regions.” *Protein Sci* 1998;**7**:667–672.

Collin MA, Clarke TH, Ayoub NA *et al.* Genomic perspectives of spider silk genes through target capture sequencing: Conservation of stabilization mechanisms and homology-based structural models of spidroin terminal regions. *Int J Biol Macromol* 2018;**113**:829–840.

Craig C. Evolution of arthropod silks. *Annu Rev Entomol* 1997;**42**:231–267.

Craig HC, Blamires SJ, Sani MA *et al.* DNP NMR spectroscopy reveals new structures, residues and interactions in wild spider silks. *Chem Commun* 2019;**55**:4687–4690.

Craig HC, Piorkowski D, Nakagawa S *et al.* Meta-analysis reveals materiomic relationships in major ampullate silk across the spider phylogeny. *J R Soc Interface* 2020;**17**:20200471.

Denny M. The physical properties of spider's silk and their role in the design of orb-webs. *J Exp Biol* 1976;**65**:483–506.

Du N, Liu XY, Narayanan J *et al.* Design of superior spider silk: from nanostructure to mechanical properties. *Biophys J* 2006;**91**:4528–4535.

Eberhard W. *Spider Webs: Behavior, Function, and Evolution*. Chicago, IL: University of Chicago Press, 2020.

Edgar RC. MUSCLE: a multiple sequence alignment method with reduced time and space complexity. *BMC Bioinformatics* 2004;**5**:113.

European Commission, European Innovation Council and SMEs Executive Agency, Izsak K *et al. Monitoring the Twin Transition of Industrial Ecosystems – Textiles – Analytical Report*. Publications Office of the European Union, 2024.

Fazio V, De Tommasi D, Pugno NM *et al.* Spider silks mechanics: Predicting humidity and temperature effects. *J Mech Phys Solids* 2022;**164**:104857.

Gao Z, Lin Z, Huang W *et al.* Structural characterization of minor ampullate spidroin domains and their distinct roles in fibroin solubility and fiber formation. *PLoS One* 2013;**8**:e56142.

Gatesy J, Hayashi C, Motriuk D *et al.* Extreme diversity, conservation, and convergence of spider silk fibroin sequences. *Science* 2001;**291**:2603–2605.

Giribet G, Edgecombe GD. The phylogeny and evolutionary history of arthropods. *Curr Biol* 2019;**29**:R592–R602.

Gosline JM, DeMont ME, Denny MW. The structure and properties of spider silk. *Endeavour* 1986;**10**:37–43.

Greco G, Arndt T, Schmuck B *et al.* Tyrosine residues mediate supercontraction in biomimetic spider silk. *Commun Mater* 2021;**2**:1–10.

Grubb DT, Jelinski LW. Fiber morphology of spider silk: the effects of tensile deformation. *Macromolecules* 1997;**30**:2860–2867.

Grubb DT, Ji G. Molecular chain orientation in supercontracted and re-extended spider silk. *Int J Biol Macromol* 1999;**24**:203–210.

Guan J, Vollrath F, Porter D. Two mechanisms for supercontraction in *Nephila* spider dragline silk. *Biomacromolecules* 2011;**12**:4030–4035.

Guerette PA, Ginzinger DG, Weber BHF *et al.* Silk properties determined by gland-specific expression of a spider fibroin gene family. *Science* 1996;**272**:112–115.

Guessous G, Blake L, Bui A *et al.* Disentangling the web: an interdisciplinary review on the potential and feasibility of spider silk bioproduction. *ACS Biomater Sci Eng* 2024;**10**:5412–5438.

Guidetti G, d'Amone L, Kim T *et al.* Silk materials at the convergence of science, sustainability, healthcare, and technology. *Appl Phys Rev* 2022;**9**:011302.

Guinea GV, Elices M, Plaza GR *et al.* Minor ampullate silks from *Nephila* and *Argiope* spiders: tensile properties and microstructural characterization. *Biomacromolecules* 2012;**13**:2087–2098.

Guinea GV, Elices M, Real JI *et al.* Reproducibility of the tensile properties of spider (*Argiope trifasciata*) silk obtained by forced silking. *J Exp Zoolog A Comp Exp Biol* 2005;**303**:37–44.

Guo C, Li C, Mu X *et al.* Engineering silk materials: From natural spinning to artificial processing. *Appl Phys Rev* 2020;**7**:011313.

Hagn F, Eisoldt L, Hardy JG *et al.* A conserved spider silk domain acts as a molecular switch that controls fibre assembly. *Nature* 2010;**465**:239–242.

Hagn F, Thamm C, Scheibel T *et al.* pH-dependent dimerization and salt-dependent stabilization of the N-terminal domain of spider dragline silk–implications for fiber formation. *Angew Chem Int Ed Engl* 2011;**50**:310–313.

Hammersley AP, Svensson SO, Hanfland M *et al.* Two-dimensional detector software: From real detector to idealised image or two-theta scan. *High Press Res* 1996;**14**:235–248.

Hanwell MD, Curtis DE, Lonie DC *et al.* Avogadro: an advanced semantic chemical editor, visualization, and analysis platform. *J Cheminformatics* 2012;**4**:17.

Hauptmann V, Weichert N, Menzel M *et al.* Native-sized spider silk proteins synthesized in planta via intein-based multimerization. *Transgenic Res* 2013;**22**:369–377.

Heidebrecht A, Eisoldt L, Diehl J *et al.* Biomimetic Fibers Made of Recombinant Spidroins with the Same Toughness as Natural Spider Silk. *Adv Mater* 2015;**4**:2189–2194.

Hepburn H, Chandler H, Davidoff M. Extensometric properties of insect fibroins: The green lacewing cross-β, honeybee α-helical and greater waxmoth parallel-β conformations. *Insect Biochem* 1979;**9**:69–77.

Herold HM, Scheibel T. Applicability of biotechnologically produced insect silks. *Z Für Naturforschung C* 2017;**72**:365–385.

Hesselberg T, Vollrath F. The mechanical properties of the non-sticky spiral in *Nephila* orb webs (Araneae, Nephilidae). *J Exp Biol* 2012;**215**:3362–3369.

Hinman MB, Lewis RV. Isolation of a clone encoding a second dragline silk fibroin. *Nephila clavipes*

dragline silk is a two-protein fiber. *J Biol Chem* 1992;**267**:19320–19324.

Holland C, Numata K, Rnjak-Kovacina J *et al.* The Biomedical Use of Silk: Past, Present, Future. *Adv Healthc Mater* 2019;**8**:e1800465.

Holland GP, Jenkins JE, Creager MS *et al.* Solid-State NMR Investigation of Major and Minor Ampullate Spider Silk in the Native and Hydrated States. *Biomacromolecules* 2008;**9**:651–657.

Hu CF, Gan CY, Zhu YJ *et al.* Modulating Polyalanine Motifs of Synthetic Spidroin for Controllable Preassembly and Strong Fiber Formation. *ACS Biomater Sci Eng* 2024;**10**:2925–2934.

Hudson SD, Zhurov V, Grbić V *et al.* Measurement of the elastic modulus of spider mite silk fibers using atomic force microscopy. *J Appl Phys* 2013;**113**:154307.

Humenik M, Scheibel T, Smith A. Spider silk: understanding the structure–function relationship of a natural fiber. In: Howorka S (ed.), *Progress in Molecular Biology and Translational Science*. Vol 103. Academic Press, 2011, 131–185.

International Organization for Standardization. Textiles – Manmade filament yarns – ISO 18066:2015 Determination of shrinkage in boiling water. 2015.

Jenkins JE, Creager MS, Butler EB *et al.* Solid-state NMR evidence for elastin-like β-turn structure in spider dragline silk. *Chem Commun* 2010;**46**:6714–6716.

Joel A-C, Kappel P, Adamova H *et al.* Cribellate thread production in spiders: Complex processing of nano-fibres into a functional capture thread. *Arthropod Struct Dev* 2015:3–8.

Johansson J, Rising A. Doing what spiders cannot—a road map to supreme artificial silk fibers. *ACS Nano* 2021;**15**:1952–1959.

Kakui K, Fleming JF, Mori M *et al.* Comprehensive transcriptome sequencing of Tanaidacea with proteomic evidences for their silk. *Genome Biol Evol* 2021;**13**:evab281.

Knight DP, Vollrath F. Biological liquid crystal elastomers. *Philos Trans R Soc Lond B Biol Sci* 2002;**357**:155–163.

Koeppel A, Holland C. Progress and trends in artificial silk spinning: a systematic review. *ACS Biomater Sci Eng* 2017;**3**:226–237.

Kono N, Nakamura H, Mori M *et al.* Multicomponent nature underlies the extraordinary mechanical properties of spider dragline silk. *Proc Natl Acad Sci* 2021a;**118**:e2107065118.

Kono N, Nakamura H, Ohtoshi R *et al.* Orb-weaving spider *Araneus ventricosus* genome elucidates the spidroin gene catalogue. *Sci Rep* 2019;**9**:8380.

Kono N, Ohtoshi R, Malay AD *et al.* Darwin's bark spider shares a spidroin repertoire with *Caerostris*

extrusa but achieves extraordinary silk toughness through gene expression. *Open Biol* 2021b;**11**:210242.

Kovoor J. Comparative Structure and Histochemistry of Silk-Producing Organs in Arachnids. *Ecophysiology of Spiders*. Springer, Berlin, Heidelberg, 1987, 160–186.

Kovoor J, Peters HM. The spinning apparatus of *Polenecia producta* (Araneae, Uloboridae): Structure and histochemistry. *Zoomorphology* 1988;**108**:47–59.

Kronqvist N, Otikovs M, Chmyrov V *et al.* Sequential pH-driven dimerization and stabilization of the N-terminal domain enables rapid spider silk formation. *Nat Commun* 2014;**5**:3254.

La Mattina C, Reza R, Hu X *et al.* Spider minor ampullate silk proteins are constituents of prey wrapping silk in the cob weaver *Latrodectus hesperus*. *Biochemistry* 2008;**47**:4692–4700.

Larkin MA, Blackshields G, Brown NP *et al.* Clustal W and Clustal X version 2.0. *Bioinformatics* 2007;**23**:2947–2948.

Lazaris A, Arcidiacono S, Huang Y *et al.* Spider silk fibers spun from soluble recombinant silk produced in mammalian cells. *Science* 2002;**295**:472–476.

Li J, Zhu Y, Yu H *et al.* Microbially Synthesized Polymeric Amyloid Fiber Promotes β-Nanocrystal Formation and Displays Gigapascal Tensile Strength. *ACS Nano* 2021;**15**:11843–11853.

Li SF, McGhie a J, Tang SL. New internal structure of spider dragline silk revealed by atomic force microscopy. *Biophys J* 1994;**66**:1209–12.

Lim X. Microplastics are everywhere — but are they harmful? *Nature* 2021;**593**:22–25.

Lin T-Y, Masunaga H, Sato R *et al.* Liquid crystalline granules align in a hierarchical structure to produce spider dragline microfibrils. *Biomacromolecules* 2017;**18**:1350–1355.

Lin Z, Deng Q, Liu XY *et al.* Engineered large spider eggcase silk protein for strong artificial fibers. *Adv Mater* 2013;**25**:1216–1220.

Liu D, Tarakanova A, Hsu CC *et al.* Spider dragline silk as torsional actuator driven by humidity. *Sci Adv* 2019;**5**:eaau9183.

Liu Y, Shao Z, Vollrath F. Relationships between supercontraction and mechanical properties of spider silk. *Nat Mater* 2005;**4**:901–905.

Liu Y, Sponner A, Porter D *et al.* Proline and processing of spider silks. *Biomacromolecules* 2008;**9**:116–121.

Lozano-Pérez AA, Pagán A, Zhurov V *et al.* The silk of gorse spider mite *Tetranychus lintearius* represents a novel natural source of nanoparticles and biomaterials. *Sci Rep* 2020;**10**:18471.

Ma B, Zhang K, Hendrie C *et al.* PEAKS: powerful software for peptide de novo sequencing by tandem mass spectrometry. *Rapid Commun Mass Spectrom RCM* 2003;**17**:2337–2342.

Madsen B, Shao ZZ, Vollrath F. Variability in the mechanical properties of spider silks on three levels: interspecific, intraspecific and intraindividual. *Int J Biol Macromol* 1999;**24**:301–306.

Madurga R, Blackledge TA, Perea B *et al.* Persistence and variation in microstructural design during the evolution of spider silk. *Sci Rep* 2015;**5**:14820.

Malay AD, Arakawa K, Numata K. Analysis of repetitive amino acid motifs reveals the essential features of spider dragline silk proteins. Zou Q (ed.). *PLoS One* 2017;**12**:e0183397.

Malay AD, Craig H, Chen J *et al.* Complexity of spider dragline silk. *Biomacromolecules* 2022;**23**:1827–1840.

Malay AD, Sato R, Yazawa K *et al.* Relationships between physical properties and sequence in silkworm silks. *Sci Rep* 2016;**6**:27573.

Malay AD, Suzuki T, Katashima T *et al.* Spider silk self-assembly via modular liquid-liquid phase separation and nanofibrillation. *Sci Adv* 2020;**6**:eabb6030.

McKim SA, Turner TL. The evolution of silk production in Crustacea. *J Crustac Biol* 2024;**44**:ruae056.

Meier F, Brunner AD, Koch S *et al.* Online parallel accumulation–serial fragmentation (PASEF) with a novel trapped ion mobility mass spectrometer. *Mol Cell Proteomics* 2018;**17**:2534–2545.

Miserez A, Yu J, Mohammadi P. Protein-Based Biological Materials: Molecular Design and Artificial Production. *Chem Rev* 2023;**123**:2049–2111.

Misof B, Liu S, Meusemann K *et al.* Phylogenomics resolves the timing and pattern of insect evolution. *Science* 2014;**346**:763–767.

Nagano A, Kikuchi Y, Sato H *et al.* Structural characterization of silk-based water-soluble peptides (Glu)n(Ala-Gly-Ser-Gly-Ala-Gly)$_4$ (n = 4−8) as a mimic of *Bombyx mori* silk fibroin by ^{13}C solid-state NMR. *Macromolecules* 2009;**42**:8950–8958.

Nakamura H, Ito Y, Sato R *et al.* Correlating Mechanical Properties and Sequence Motifs in Artificial Spider Silk by Targeted Motif Substitution. *ACS Biomater Sci Eng* 2024;**10**:7394–7403.

Nakamura H, Kono N, Mori M *et al.* Composition of minor ampullate silk makes its properties different from those of major ampullate silk. *Biomacromolecules* 2023;**24**:2042–2051.

Numata K, Sato R, Yazawa K *et al.* Crystal structure and physical properties of *Antheraea yamamai* silk fibers: Long poly(alanine) sequences are partially in the crystalline region. *Polymer* 2015;**77**:87–94.

Oktaviani NA, Malay AD, Matsugami A *et al.* Unusual pK_a values mediate the self-assembly of spider dragline silk proteins. *Biomacromolecules* 2023;**24**:1604–1616.

Perea GB, Riekel C, Guinea GV *et al.* Identification and dynamics of polyglycine II nanocrystals in *Argiope trifasciata* flagelliform silk. *Sci Rep* 2013;**3**:3061.

Pérez-Rigueiro J, Elices M, Plaza GR *et al.* Basic principles in the design of spider silk fibers. *Molecules* 2021;**26**:1794.

Pérez-Rigueiro J, Madurga R, Gañán-Calvo AM *et al.* Emergence of supercontraction in regenerated silkworm (*Bombyx mori*) silk fibers. *Sci Rep* 2019;**9**:2398.

Peters HM. On the structure and glandular origin of bridging lines used by spiders for moving to distant places. *Acta Zool Fenn* 1990;**190**:309–314.

Peters HM, Kovoor J. The silk-producing system of *Linyphia triangularis* (Araneae, Linyphiidae) and some comparisons with Araneidae: Structure, histochemistry and function. *Zoomorphology* 1991;**111**:1–17.

Porter D, Guan J, Vollrath F. Spider silk: super material or thin fibre? *Adv Mater* 2013;**25**:1275–1279.

Rappsilber J, Ishihama Y, Mann M. Stop and go extraction tips for matrix-assisted laser desorption/ionization, nanoelectrospray, and LC/MS sample pretreatment in proteomics. *Anal Chem* 2003;**75**:663–670.

Riekel C, Bränden C, Craig C *et al.* Aspects of X-ray diffraction on single spider fibers. *Int J Biol Macromol* 1999;**24**:179–186.

Riekel C, Burghammer M, Rosenthal M. Mesoscale structures in amorphous silks from a spider's orb-web. *Sci Rep* 2020;**10**:18205.

Rising A, Johansson J. Toward spinning artificial spider silk. *Nat Chem Biol* 2015;**11**:309–315.

Rising A, Johansson J, Larson G *et al.* Major ampullate spidroins from *Euprosthenops australis*: multiplicity at protein, mRNA and gene levels. *Insect Mol Biol* 2007;**16**:551–561.

Ritchie RO. The conflicts between strength and toughness. *Nat Mater* 2011;**10**:817–822.

Rudall KM, Kenchington W. Arthropod silks: the problem of fibrous proteins in animal tissues. *Annu Rev Entomol* 1971;**16**:73–96.

Sampath S, Isdebski T, Jenkins JE *et al.* X-ray diffraction study of nanocrystalline and amorphous structure within major and minor ampullate dragline spider silks. *Soft Matter* 2012;**8**:6713–6722.

Sampath S, Yarger JL. Structural hysteresis in dragline spider silks induced by supercontraction: an X-ray fiber micro-diffraction study. *RSC Adv* 2015;**5**:1462–1473.

Saric M, Eisoldt L, Döring V *et al.* Interplay of different major ampullate spidroins during assembly and implications for fiber mechanics. *Adv Mater* 2021;**33**:2006499.

Saric M, Scheibel T. Two-in-one spider silk protein with combined mechanical features in all-aqueous spun fibers. *Biomacromolecules* 2023;**24**:1744–1750.

Savage KN, Gosline JM. The effect of proline on the network structure of major ampullate silks as inferred from their mechanical and optical properties. *J Exp Biol* 2008a;**211**:1937–1947.

Savage KN, Gosline JM. The role of proline in the elastic mechanism of hydrated spider silks. *J Exp Biol* 2008b;**211**:1948–1957.

Sen D, Buehler MJ. Structural hierarchies define toughness and defect-tolerance despite simple and mechanically inferior brittle building blocks. *Sci Rep* 2011;**1**:35.

Shao Z, Vollrath F. The effect of solvents on the contraction and mechanical properties of spider silk. *Polymer* 1999;**40**:1799–1806.

Shao Z, Vollrath F, Sirichaisit J *et al.* Analysis of spider silk in native and supercontracted states using Raman spectroscopy. *Polymer* 1999;**40**:2493–2500.

Simmons A, Ray E, Jelinski LW. Solid-state ^{13}C NMR of *Nephila clavipes* dragline silk establishes structure and identity of crystalline regions. *Macromolecules* 1994;**27**:5235–5237.

Simmons AH, Michal CA, Jelinski LW. Molecular orientation and two-component nature of the crystalline fraction of spider dragline silk. *Science* 1996;**271**:84–87.

Simmons JR, Xu L, Rainey JK. Recombinant pyriform silk fiber mechanics are modulated by wet-spinning conditions. *ACS Biomater Sci Eng* 2019;**5**:4985–4993.

Sonavane S, Hassan S, Chatterjee U *et al.* Origin, structure, and composition of the spider major ampullate silk fiber revealed by genomics, proteomics, and single-cell and spatial transcriptomics. *Sci Adv* 2024;**10**:eadn0597.

Sponner A, Vater W, Monajembashi S *et al.* Composition and hierarchical organisation of a spider silk. *PLoS One* 2007;**2**:e998.

Stauffer SL, Coguill SL, Lewis RV. Comparison of physical properties of three silks from *Nephila clavipes* and *Araneus gemmoides*. *J Arachnol* 1994;**22**:5–11.

Sutherland TD, Young JH, Weisman S *et al.* Insect silk: one name, many materials. *Annu Rev Entomol* 2010;**55**:171–188.

Suzuki Y, Higashi T, Yamamoto T *et al.* Presence of β-turn structure in recombinant spider silk dissolved in formic acid revealed with NMR. *Molecules* 2022;**27**:511.

Tachibana Y, Darbe S, Hayashi S *et al.* Environmental biodegradability of recombinant structural protein. *Sci Rep* 2021;**11**:242.

Termonia Y. Molecular modeling of spider silk elasticity. *Macromolecules* 1994;**27**:7378–7381.

Teulé F, Furin WA, Cooper AR *et al.* Modifications of spider silk sequences in an attempt to control the mechanical properties of the synthetic fibers. *J Mater Sci* 2007;**42**:8974–8985.

Tian M, Lewis RV. Molecular characterization and evolutionary study of spider tubuliform (eggcase) silk protein. *Biochemistry* 2005;**44**:8006–8012.

Van Beek JD, Hess S, Vollrath F *et al.* The molecular structure of spider dragline silk: Folding and orientation of the protein backbone. *Proc Natl Acad Sci* 2002;**99**:10266–10271.

Vollrath F, Porter D. Spider silk as archetypal protein elastomer. *Soft Matter* 2006;**2**:377–385.

Warwicker JO. The crystal structure of silk fibroin. *Acta Crystallogr* 1954;**7**:565–573.

Warwicker JO. Comparative studies of fibroins: II. The crystal structures of various fibroins. *J Mol Biol* 1960;**2**:350–362.

Watanabe Y, Arakawa K. Molecular mechanisms of the high performance of spider silks revealed through multi-omics analysis. *Biophys Physicobiology* 2023;**20**:e200014.

Whittall DR, Baker KV, Breitling R *et al.* Host systems for the production of recombinant spider silk. *Trends Biotechnol* 2021;**39**:560–573.

Wiśniewski JR, Hein MY, Cox J *et al.* A "proteomic ruler" for protein copy number and concentration estimation without spike-in standards. *Mol Cell Proteomics* 2014;**13**:3497–3506.

Work RW. Dimensions, birefringences, and force-elongation behavior of major and minor ampullate silk fibers from orb-web-spinning spiders—the effects of wetting on these properties. *Text Res J* 1977;**47**:650–662.

Work RW. A comparative study of the supercontraction of major ampullate silk fibers of orb-web-building spiders (Araneae). *J Arachnol* 1981;**9**:299–308.

Work RW, Young CT. The amino acid compositions of major and minor ampullate silks of certain orb-web-building spiders (Araneae, Araneidae). *J Arachnol* 1987;**15**:65–80.

Xia XX, Qian ZG, Ki CS *et al.* Native-sized recombinant spider silk protein produced in metabolically engineered *Escherichia coli* results in a strong fiber. *Proc Natl Acad Sci U S A* 2010;**107**:14059–63.

Xu M, Lewis RV. Structure of a protein superfiber: spider dragline silk. *Proc Natl Acad Sci U S A* 1990;**87**:7120–7124.

Yang Z, Liivak O, Seidel A *et al.* Supercontraction and backbone dynamics in spider silk: ^{13}C and ^{2}H NMR studies. *J Am Chem Soc* 2000;**122**:9019–9025.

Yazawa K, Malay AD, Masunaga H *et al.* Role of Skin Layers on Mechanical Properties and Supercontraction of Spider Dragline Silk Fiber. *Macromol Biosci* 2019;**19**:1800220.

Yazawa K, Malay AD, Masunaga H *et al.* Simultaneous effect of strain rate and humidity on the structure and mechanical behavior of spider silk. *Commun Mater* 2020;**1**:1–10.

Yoshioka T, Kameda T, Tashiro K *et al.* Transformation of coiled α-helices into cross-β-sheets superstructure. *Biomacromolecules* 2017;**18**:3892–3903.

Zschokke S. The influence of the auxiliary spiral on the capture spiral in *Araneus diadematus* Clerck (Araneidae). *Bull Br Arachnol Soc* 1993;**9**:169–173.

Zschokke S, Vollrath F. Unfreezing the behaviour of two orb spiders. *Physiol Behav* 1995;**58**:1167–1173.